Friedrich–Schiller-Universität Jena
Physikalisch–Astronomische Fakultät

Cosmological Weak Lensing of the Cosmic Microwave Background by Large Scale Structures

Diploma Thesis

submitted by

Christoph Pfrommer

born on October 22, 1975 in Ulm

Supervisors of the Diploma Thesis:

Prof. Dr. Simon D. M. White
Prof. Dr. Reinhard Meinel
PD Dr. Matthias Bartelmann

Day of granting the Diploma: July, 1

Contents

1 Introduction and Motivation

As the cosmic microwave background (CMB) photons propagate from the surface of last scattering through intervening large–scales structures, they experience gravitational light deflection due to inhomogeneous gravitational fields along their geodesics. After a historical introduction into both gravitational lensing and the cosmic microwave background, the individual chapters of this work will be outlined.

More than two centuries ago, several researchers, among others Newton and Laplace, speculated about the possibility of gravitational light deflection. Assuming a material particle concept of light, Soldner (1804) calculated the magnitude of the gravitational light deflection by the Sun using Newtonian Gravity. Much later, Einstein (1915) formulated General Relativity describing space–time as a four–dimensional manifold whose metric tensor is determined through second order partial differential equations by the energy–momentum tensor of the relevant cosmological fluid components. Applying these equations in the weak field limit, he recalculated the deflection angle due to the Sun to be $1.7''$, twice the result previously obtained using Newtonian Gravity. This value was confirmed by Dyson, Eddington & Davidson (1920) during their expedition on the occasion of a total solar eclipse, when they measured the apparent angular shift of stars close to the Sun. In addition to the explanation of the discrepancy in the perihelion shift of Mercury, this was a further important step towards accepting General Relativity as the correct theory of gravity. After the first discovery of a multiply–imaged quasar by Walsh, Carswell & Weymann (1979), the area of gravitational lensing developed into an active field of research. Among many others, maybe the most prominent examples of gravitational lensing systems are the first Einstein–ring observed in the radio waveband by Hewitt et al. (1987) as well as the giant luminous arcs in galaxy clusters (Soucail et al. (1987) and Lynds & Petrosian (1986)), which can only appear in very precise alignments of source and lens. All those examples are manifestations of *strong lensing*, which is comparatively easy to detect and provides a valuable tool for detailed analyses of the surface mass density of the deflecting object. However, in most of the cases, light rays are merely slightly deflected by gravity, such that astronomical sources are only weakly distorted. This has the consequence that distortions are generally very difficult to detect in individual objects and can only be verified by averaging the net distortion over an ensemble of images. In order to develop a theoretical understanding of realistic implications of weak lensing, numerous simulations have been performed, studying weak lensing in realistic N–body simulations. The first calculations were performed by Blandford et al. (1991),

Miralda-Escude (1991) and Kaiser (1992). Recently, Wambsganss, Cen & Ostriker (1998) and Jain, Seljak & White (2000) conducted more detailed numerical studies of lensing by large–scale structures. This technique is even more important if we study the lensing effect on the CMB radiation, which is itself a realization of a Gaussian random field.

The idea that the cosmic microwave background originated from a hot phase after the Big Bang was developed by Gamow (1948), when he studied the synthesis of the light elements in the early Universe. During the hot era of the Universe, the photons were created in thermal equilibrium with electromagnetically interacting particles until the temperature was sufficiently lowered by the expansion of the Universe for electrons to combine with the newly formed nuclei of hydrogen. This made the Universe transparent for the released photons, now propagating freely through the expanding cosmos, causing the temperature of their black–body distribution to decrease as the photon momenta got redshifted. In 1950, Alpher & Herman (1950) estimated the current value of the temperature of such a primordial radiation to $T_0 \approx 5\,\mathrm{K}$ corresponding to the microwave range of the electromagnetic spectrum. The CMB radiation was serendipitously discovered by Penzias & Wilson (1965) as an "excess antenna temperature". Fixsen et al. (1996) used the FIRAS instrument onboard the COBE satellite to prove its perfect black–body spectrum with a temperature today of $T_0 = 2.725 \pm 0.002$ K (95% confidence limit, Mather et al. (1999)), which moreover can be measured in all directions.

The decoupling of the CMB photons from the photon–baryon plasma provides an imprint of the Universe at the state of recombination with any existing small density perturbations on an otherwise isotropic and homogeneous matter distribution. These small fluctuations act as seeds for the growth of structure in our Universe like the present observable galaxies, clusters of galaxies and filamentary large–scale structures. Thus, soon after the detection of the CMB, the search of fluctuations within the smooth background began. With increasing accuracy of the observations, first a dipole anisotropy on the level of $(T - T_0)/T_0 \equiv \delta T/T_0 \sim 10^{-3}$ was revealed, which is caused by the peculiar velocity of the Earth with respect to the rest frame of the CMB (Smoot et al. 1977), whereas the first higher order fluctuations of primordial cosmological origin were detected by COBE. This was followed by a number of balloon experiments like BOOMERANG (de Bernardis et al. 2002) and MAXIMA (Lee et al. 2001), increasing the angular resolution, but mapping only small parts of the sky and thus lacking completeness. In order to map the full sky CMB temperature fluctuations with high angular resolution, two satellites have been designed, named MAP and PLANCK, where the latter has an angular resolution down to $5'$. In order to fully extract the information of the original CMB fluctuations at these relatively small scales, and to pinpoint the parameters of the Universe, one has to consider some important foreground effects like weak gravitational lensing which cause distortions of the initial CMB distribution. Early work in this already well–studied field considered lensing effects on the temperature correlation function (e.g. Blanchard & Schneider (1987), Linder (1988), Cole & Efstathiou (1989), Watanabe & Tomita (1991), and Fukugita et al. (1992)),

whereas the focus shifted in the further development towards harmonic space power spectrum analyses (e.g. Seljak (1996), Zaldarriaga & Seljak (1998), Hu (2000), and Hu & White (2001)).

These studies were merely concerned with analytic solutions or simple numerical toy models in order to approach the problem of weak lensing of the CMB anisotropies. In contrast, this work is using the high resolution of structure formation simulations done by the Virgo Consortium (for details see chapter 5), in order to perform ray tracing simulations through realistic universes studying weak lensing effects. These simulations are then applied to numerically generated CMB fluctuation maps for studying the lensing influence on them. This work is structured into two main parts, the first of which is intended to provide a detailed theoretical framework for the involved cosmological and mathematical topics, while the second deals with cosmological weak lensing simulations of the CMB.

The first part starts with an introduction into the cosmological topics relevant for the purpose of this work. We restrict ourselves only to those ideas which are thoroughly used later on and refer to the literature for further mathematical detail. After introducing the Friedmann–Lemaître cosmological models and important definitions, both the physical processes leading to the CMB temperature fluctuations and their statistical description are presented. Then the theory of structure formation is described, according to theory originating from seed fluctuations at the epoch of recombination. Eventually, the observational evidence is summarized for the most favored cosmological model used in our simulations.

The following chapter 3 is concerned with the statistical background of correlation functions and power spectra, their projections onto flat sky and their correspondence in the harmonic and flat–sky approximation.

The first part ends with an introduction into gravitational lensing in chapter 4. After presenting the main ideas of gravitational lensing theory, the more general weak cosmological lensing approach is discussed, which is finally used to describe lensing of the CMB anisotropies.

The second part first deals with statistical lensing quantities using very large simulations (Jenkins et al. (1998) and Jenkins et al. (2001)) and applying Limber's equation relating the power spectrum of three–dimensional homogeneous and isotropic random fields to the power spectrum of two–dimensional projections of such fields. In the succeeding chapter 6, ray-tracing simulations through large cosmological N–body simulations are performed, and power spectra of certain lensing quantities of consideration are compared to theoretical expectations. Finally, chapter 7 represents the essential part of the thesis in which weak cosmological lensing of the CMB temperature fluctuations is studied based on their power spectra and local statistical methods.

Part I

Theoretical Background

2 Cosmological Background

In this chapter the fundamental cosmological concepts will be presented which are necessary for the scope of this work. After introducing the family of Friedmann–Lemaître cosmological models together with some basic definitions, the theories of the cosmic microwave background radiation (CMB) and structure formation are presented.

2.1 Friedmann–Lemaître Cosmological Models

2.1.1 Geometry of Space–Time – Robertson–Walker Metric

The standard cosmological model is based upon two fundamental postulates: After averaging over sufficiently large scales, there is an isotropic matter and radiation distribution around us and second, the position of the Earth in space–time is not preferred over others, the so called cosmological or Copernican principle. The first postulate is supported by observations of galaxy populations in the observed Universe today, which is perceived to be isotropic on the largest scales ($\gg 10\,h^{-1}$Mpc $\sim$ scale of a galaxy cluster). Another strong argument in favor of isotropy is the perfect rotational invariance of the CMB temperature in the comoving frame. The smoothness of the CMB, $\delta T/T_0 \sim 10^{-5}$ on all angular scales measured, is an indication of an isotropic and homogeneous distribution of matter and radiation at early times. Accepting the isotropy on the spatial hyper–surface around an observer on Earth and applying the cosmological principle in space leads to isotropy around any point on a spatial hyper–surface. Assuming further that the metric is an analytic function of the coordinates immediately implies homogeneity.

Taking the symmetry assumptions of isotropy and homogeneity motivated by observations, the metric can be written in the form (for derivation see Misner, Thorne & Wheeler (1973) or d'Inverno (1992))

$$\mathrm{d}s^2 = c^2\mathrm{d}t^2 - a(t)^2\left[\mathrm{d}w^2 + f_K^2(w)\left(\mathrm{d}\theta^2 + \sin^2\theta\mathrm{d}\phi^2\right)\right], \tag{2.1}$$

which is called the *Robertson–Walker metric*. If one considers space–time as being filled with a fluid, then the coordinates (w, θ, ϕ) are the coordinates of a comoving fluid element where w is the radial distance from the origin and (θ, ϕ) are the two angles characterizing a point on the unit sphere around the origin. The coordinate t is the proper time of a comoving clock in such an element with constant w, θ, ϕ.

Observers at rest in a comoving frame are called *fundamental observers*. Specifically,

$$f_K(w) = \begin{cases} \frac{1}{\sqrt{K}} \sin(\sqrt{K} w) & (K > 0) \\ w & (K = 0) \\ \frac{1}{\sqrt{-K}} \sinh[\sqrt{-K} w] & (K < 0) \end{cases} . \tag{2.2}$$

Due to its high symmetry, the Robertson–Walker metric allows only two free parameters: K, which is related to the curvature of three–dimensional spatial hyper–surfaces, $R^{(3)} = \frac{6\,K}{a^2(t)}$. One distinguishes between three different geometries of an open ($K < 0$), a flat ($K = 0$) and a closed ($K > 0$) Universe according to the sign of the curvature. It is important to notice that $f_K(w)$ and therefore $|K|^{-1/2}$ both have the dimension of length. The other parameter $a(t)$ describes the conformal mapping between hyper–surfaces separated by time–like vectors and is a function of cosmic time t only. In the dynamical context, this parameter describes the evolution of the Universe and is therefore called the *cosmic scale factor* $a(t)$. Conventionally, it is normalized such that its value is unity at the present epoch t_0.

If the radius r of the two–spheres is defined by $r \equiv f_K(w)$, then the metric takes the following form:

$$\mathrm{d}s^2 = c^2 \mathrm{d}t^2 - a(t)^2 \left[\frac{\mathrm{d}r^2}{1 - Kr^2} + r^2 \left(\mathrm{d}\theta^2 + \sin^2\theta \mathrm{d}\phi^2 \right) \right] . \tag{2.3}$$

This metric shows that hyper–surfaces of constant cosmic time t form a maximally symmetric space, i.e. a space with constant curvature. However the curvature of the overall space–time can change with time. The time dependence of the cosmic scale factor and the dependence of K on the matter content of the Universe uniquely determine space–time.

2.1.2 Dynamics of Space–Time – Friedmann Equation

According to General Relativity, space–time is a four–dimensional manifold, whose metric tensor is a dynamical field. The dynamics of this field is governed by Einstein's field equations (1915)

$$G_{\mu\nu} \equiv R_{\mu\nu} - \frac{R}{2} g_{\mu\nu} = \frac{8\pi G}{c^4} T_{\mu\nu} + \Lambda g_{\mu\nu} \,, \tag{2.4}$$

where both the energy–momentum tensor $T_{\mu\nu}$ of matter and radiation and the cosmological constant Λ act as sources of gravity which itself couples back to the right–hand side of the equation. These considerations show the inherent non–linearity of the field equations.

Friedmann's solution of an expanding Universe solves Einstein's equations (2.4) assuming the energy–momentum tensor of a perfect fluid, which is completely determined by the energy density ρ, the pressure p and the four–velocity u_μ of the fluid,

$$T_{\mu\nu} = \left(\rho + \frac{p}{c^2} \right) u_\mu u_\nu - p g_{\mu\nu} . \tag{2.5}$$

With this energy–momentum tensor (2.5) and the metric (2.1), the general set of Einstein's field equations (2.4) is reduced to two independent ordinary differential equations for three unknown functions of time, $a(t)$, $\rho(t)$ and $p(t)$:

$$H^2 \equiv \left(\frac{\dot{a}}{a}\right)^2 = \frac{8\pi G}{3}\rho - \frac{Kc^2}{a^2} + \frac{\Lambda c^2}{3} \tag{2.6}$$

and

$$\frac{\ddot{a}}{a} = -\frac{4}{3}\pi G\left(\rho + \frac{3p}{c^2}\right) + \frac{\Lambda c^2}{3}, \tag{2.7}$$

where the dot denotes the derivative with respect to the coordinate time t. Equation (2.6) defines the *Hubble parameter* H, which is a measure for the expansion rate of the Universe. Its value at the present epoch is the *Hubble constant* $H(t_0) \equiv H_0$, whose uncertainty is commonly expressed as $H_0 = 100\,h\,\mathrm{km\,s^{-1}\,Mpc^{-1}}$ with the best current value of $h = 0.72 \pm 0.08$ (Freedman et al. 2001).

The two equations (2.6) and (2.7) can be combined to give the *adiabatic equation*,

$$\frac{\mathrm{d}}{\mathrm{d}t}\left[a^3(t)\rho(t)c^2\right] + p(t)\frac{\mathrm{d}}{\mathrm{d}t}\left[a^3(t)\right] = 0. \tag{2.8}$$

This can also be independently obtained by virtue of the conservation equations of Einstein's field equations, $T^{\mu\nu}{}_{;\nu} = 0$, which itself is a necessary requirement for the contracted Bianchi identities $G^{\mu\nu}{}_{;\nu} = 0$ to hold identically. The first term of the adiabatic equation is proportional to the change of energy contained in a fixed comoving volume, which has the meaning of an "internal" energy, whereas the second term is proportional to the change of the proper volume. So equation (2.8) states the first law of thermodynamics in a cosmological context and conserves the entropy per comoving volume in thermal equilibrium, $S = \frac{(\rho c^2 + p)V}{T} = \mathrm{const}$.

2.1.3 Different Epochs of the Universe

The underdetermined set of Friedmann's equations (2.6) and (2.7) is completed by the equation of state, $p = p(\rho, S)$. The equation of state of all cosmologically relevant fluids f can be parametrized by $p = \omega_f \rho c^2$, where ω_f is assumed to be independent of time in the simplest cases. Inserting this expression into equation (2.8) yields the following solution

$$\rho_f(t) = \rho_{f,0}\, a^{-3(1+\omega_f)}. \tag{2.9}$$

In the course of its evolution, the Universe traversed three epochs, in which its dynamics was mainly determined by one of the components, radiation, matter and vacuum energy, respectively.

- The *radiation dominated* era is characterized by $\omega_r = \frac{1}{3}$, which is valid for a non–degenerate ultra–relativistic gas in thermal equilibrium and leads to $\rho_r \propto a^{-4}$. In addition to a volume factor of a^3 for the dilution effect as the Universe expands, there is an additional factor of a for the redshift of photon momentum.

- The *matter dominated* era is described by a pressureless fluid, $\omega_m = 0$, which is a good approximation for a non–relativistic gas or fluid with the property $p \ll \rho c^2$. Thus, the density evolution reads $\rho_m \propto a^{-3}$. The matter density gets diluted at the same rate as the proper volume increases, which is the conservation law of the total amount of energy in the comoving frame. Since the slope of the radiation energy density ρ_r as a function of the scale factor is steeper than that of the matter density ρ_m, it follows that the early Universe was radiation dominated. After a transition period, the so–called *matter–radiation equality* at $a_{\rm eq}$ with equal densities of the two fluids, the matter dominated regime took over. The energy density of ordinary and relativistic matter were equal when the scale factor $a(t)$ was

$$a_{\rm eq} = \left(\frac{\rho_r}{\rho_m}\right)_{\rm today} . \tag{2.10}$$

- Finally, the possible era of the *domination of a cosmological constant* is described by a fluid with negative pressure, $\omega_\Lambda = -1$. This can be obtained from the definition of the energy–momentum tensor of the cosmological constant Λ, which is treated in this context as a perfect fluid component of the Universe $\frac{8\pi G}{c^4} T^{\mu\nu}_\Lambda \equiv \Lambda g^{\mu\nu}$. After taking the trace of this equation and using the definitions (2.13) and (2.14), the desired equation of state follows. This gives rise to a constant energy density $\rho_\Lambda \propto$ const. The transition from the matter dominated epoch into the Λ–dominated epoch occurred at

$$a_{\rm eq,\Lambda} = \sqrt[3]{\frac{\rho_m}{\rho_\Lambda}} , \tag{2.11}$$

  using density values for ρ_m and ρ_Λ at the present epoch.

A much more intuitive form of Friedmann's equation (2.6) can be obtained by defining the *critical density* of the Universe

$$\rho_{\rm cr} \equiv \frac{3H_0^2}{8\pi G} \approx 1.9 \cdot 10^{-29}\, h^2\, {\rm g\,cm^{-3}}, \tag{2.12}$$

which is the energy density that corresponds to a spatially flat Universe without a cosmological constant, i.e. $K = 0$ and $\Lambda = 0$. With this definition in mind, one can introduce the dimensionless *density parameters*

$$\Omega_f \equiv \left(\frac{\rho_f}{\rho_{\rm cr}}\right)_{\rm today} \tag{2.13}$$

$$\text{and} \qquad \Omega_\Lambda \equiv \frac{\Lambda c^2}{3H_0^2}. \tag{2.14}$$

Here the index f accounts for a cosmological matter component which was either relativistic during the decoupling from the other fluid components (r) or non–relativistic

(m). Taking equation (2.6) at the present time where the scale factor is normalized to unity and recalling the previous definitions leads to an expression for the curvature

$$K\left(\frac{c}{H_0}\right)^2 = \Omega_m + \Omega_r + \Omega_\Lambda - 1 \equiv \Omega_{\rm tot} - 1\,, \tag{2.15}$$

which defines the total density $\Omega_{\rm tot}$. Now, the first Friedmann equation (2.6) can be written in the following nice form

$$H^2(t) = H_0^2\left[\frac{\Omega_r}{a^4(t)} + \frac{\Omega_m}{a^3(t)} + \frac{1-\Omega_m-\Omega_r-\Omega_\Lambda}{a^2(t)} + \Omega_\Lambda\right]. \tag{2.16}$$

The time evolution of the Hubble parameter $H(t)$ can be used to determine the dependence of the density parameters Ω_m and Ω_Λ on the scale factor assuming a matter–dominated Universe, i.e. neglecting Ω_r,

$$\Omega_m(a) = \frac{8\pi G}{3H^2(a)}\frac{\rho_m(t_0)}{a^3} = \frac{\Omega_m}{a+\Omega_m(1-a)+\Omega_\Lambda(a^3-a)}\,, \tag{2.17}$$

$$\Omega_\Lambda(a) = \frac{\Lambda c^2}{3H^2(a)} = \frac{\Omega_\Lambda a^3}{a+\Omega_m(1-a)+\Omega_\Lambda(a^3-a)}\,. \tag{2.18}$$

Another fundamental parameter closely related to the future evolution of the Universe is the deceleration parameter, q_0, which measures the rate of change of the expansion today

$$q_0 \equiv -\frac{1}{H_0^2}\left(\frac{\ddot{a}}{a}\right)_0 = \frac{1}{2}\Omega_m + \frac{3}{2}\sum_f \Omega_f\omega_f\,, \tag{2.19}$$

where equation (2.7) was used in the last step and the summation is extended over radiation and a cosmological constant, $f \in \{r, \Lambda\}$. Due to the definition with the negative sign, the deceleration parameter q_0 measures acceleration in the case $q_0 < 0$ and deceleration for $q_0 > 0$.

2.1.4 Redshift

The concept of cosmic redshift z is an important quantity in cosmology, which uses purely geometric arguments and does not involve dynamical arguments other than the predicted expansion of the Universe by Friedmann's equation. Consider a comoving source emitting light with a wavelength λ_e at t_e which reaches the observer with wavelength λ_o at t_o. The redshift is defined as the relative change in wavelength

$$z \equiv \frac{\lambda_o - \lambda_e}{\lambda_e}. \tag{2.20}$$

The reason for this redshift is the expansion of the Universe while the photons propagate from the source to the observer. Photons travel on radial null geodesics of zero proper time

$$\mathrm{d}s^2 = c^2\mathrm{d}\tau^2 = c^2\mathrm{d}t^2 - a(t)^2\mathrm{d}w^2 = 0. \tag{2.21}$$

Because the comoving coordinate distance w from the source to the observer is constant and time independent by definition, it follows

$$w = \int_o^e \mathrm{d}w = \int_{t_e}^{t_o} \frac{c\,\mathrm{d}t}{a(t)} = \text{const.} \tag{2.22}$$

$$\text{and} \qquad w = \int_{t_e+\delta t_e}^{t_o+\delta t_o} \frac{c\,\mathrm{d}t}{a(t)} = w + c\frac{\delta t_o}{a(t_o)} - c\frac{\delta t_e}{a(t_e)}. \tag{2.23}$$

Hence,

$$\frac{\delta t_o}{\delta t_e} = \frac{a(t_o)}{a(t_e)}. \tag{2.24}$$

Relating the inverse of the emitted and observed time intervals to the frequencies of the light, $\delta t_e = \nu_e^{-1}$ and $\delta t_o = \nu_o^{-1}$ yields the important relation

$$1 + z = \frac{a(t_o)}{a(t_e)} = \frac{1}{a(t_e)} \qquad \text{for} \qquad a(t_o) = 1. \tag{2.25}$$

2.1.5 Distance Definitions

In an arbitrary curved space–time, such as that underlying General Relativity, the term "distance" has no longer a unique meaning. Due to the high symmetry of Euclidean space, "distance" combines different properties which are no longer equivalent in General Relativity, so that each desired property needs its own distance definition in curved space–time. For the purpose of this thesis, three different distance scales are important, the proper distance, the comoving distance and the angular diameter distance. Distance measures between different time–like geodesic lines are done by light signals, which are emitted at time t_e from the source and observed at time t_o. Assuming the scale factor $a(t)$ to be a monotonic function, which is at least true piecewise, the coordinate time t can be related in a unique way to the cosmic scale factor a, which occurs in the Friedmann equation.

Proper Distance The *proper distance* $D_{\mathrm{prop}}(a_e, a_o)$ is the elapsed coordinate time a light signal needs to propagate from the source at $a_e = a(t_e)$ to the observer at $a_o = a(t_o)$ and is defined by $\mathrm{d}D_{\mathrm{prop}} \equiv -c\,\mathrm{d}t = -c\,\mathrm{d}a\,\dot{a}^{-1} = -c\,\mathrm{d}a\,(aH)^{-1}$. The last step uses the definition of the Hubble parameter in (2.6) and the minus sign arises because of the choice of the coordinate origin at the observer and the requirement of an increasing distance the further back one goes in time. This yields

$$D_{\mathrm{prop}}(a_e, a_o) = \frac{c}{H_0} \int_{a_e}^{a_o} \frac{\mathrm{d}a}{\sqrt{\Omega_r a^{-2} + \Omega_m a^{-1} + (1 - \Omega_m - \Omega_r - \Omega_\Lambda) + \Omega_\Lambda a^2}}\,. \tag{2.26}$$

Comoving Distance The *comoving distance* $D_{\mathrm{com}}(a_e, a_o)$ is the distance on the spatial hyper–surface $t = t_0$ between the world–lines of a source and an observer locked into the Hubble flow. In other words it is the radial distance on this hyper–surface with the scale factor, i.e. the cosmic expansion, divided out. Its definition $\mathrm{d}D_{\mathrm{com}} \equiv \mathrm{d}w$ can

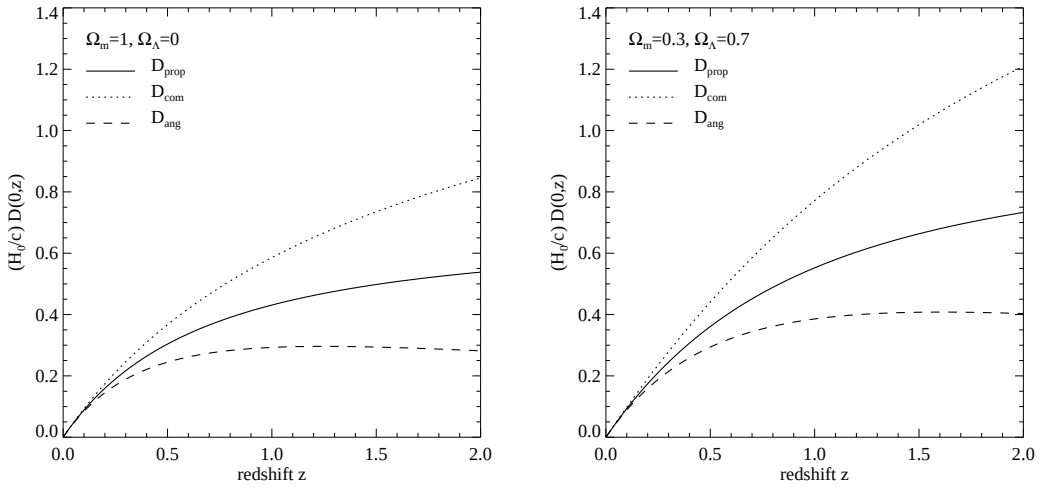

Figure 2.1: Three distance definitions are plotted as a function of source redshift z with the observer being at redshift zero. These are the proper distance $D_{\rm prop}$ (solid line), the comoving distance $D_{\rm com}$ (dotted line), and the angular diameter distance $D_{\rm ang}$ (dashed line). On the left–hand side an Einstein–de Sitter cosmology is shown in comparison with the currently preferred ΛCDM cosmology on the right–hand side.

---

be rewritten using (2.21) yielding $\mathrm{d}D_{\rm com} = -c\,a^{-1}\,\mathrm{d}t = -c\,\mathrm{d}a(a\dot{a})^{-1} = -c\,\mathrm{d}a(a^2H)^{-1}$. Hence,

$$D_{\rm com}(a_e, a_o) = \frac{c}{H_0}\int_{a_e}^{a_o} \frac{\mathrm{d}a}{\sqrt{\Omega_r + \Omega_m a + (1-\Omega_m-\Omega_r-\Omega_\Lambda)a^2 + \Omega_\Lambda a^4}} = w(a_e, a_o)\,. \tag{2.27}$$

Angular Diameter Distance Finally, the *angular diameter distance* $D_{\rm ang}(a_e, a_o)$ is defined such that the relation in Euclidean space between the physical size of the cross–section δA of an object and the solid angle $\delta\Omega$ that it subtends also holds in curved space, $\delta\Omega\, D_{\rm ang}^2 = \delta A$. Using the expression for the physical surface area of a 2–sphere centered at the observer

$$A_2 = \int_\Omega \mathrm{d}\Omega\sqrt{-g^{(3)}} = 4\pi a_e^2\, f_K^2[w(a_e, a_o)] \tag{2.28}$$

$$\text{and} \qquad \frac{\delta\Omega}{4\pi} = \frac{\delta A}{4\pi a_e^2\, f_K^2[w(a_e, a_o)]}, \tag{2.29}$$

one obtains the formula for the angular diameter distance

$$D_{\rm ang}(a_e, a_o) \equiv \left(\frac{\delta A}{\delta\Omega}\right)^{1/2} = a_e f_K[w(a_e, a_o)] = a_e f_K[D_{\rm com}(a_e, a_o)]. \tag{2.30}$$

The integral representation of both the proper and comoving distances leads to the nice property of their being additive functions, i.e. two adjacent distances can be

computed using the starting point of the first one and the ending point of the second one, $D_{\rm com}(a_1, a_2) + D_{\rm com}(a_2, a_3) = D_{\rm com}(a_1, a_3)$. Unfortunately, the angular diameter distance does not have the additive property in general.

In addition, a commonly used distance definition derived from the prior two definitions is the *comoving angular diameter distance* $D_{\rm com,ang}(a_e, a_o)$ which can be defined as follows,

$$D_{\rm com,ang}(a_e, a_o) \equiv \frac{1}{a_e}\left(\frac{\delta A}{\delta\Omega}\right)^{1/2} = f_K[w(a_e, a_o)]. \tag{2.31}$$

2.2 Cosmic Microwave Background

Before presenting the statistical formalism of temperature fluctuations in the cosmic microwave background radiation (CMB), the physical processes during the recombination as well as the relevant scaling laws are explained. The presentation in the following relies mainly on the textbooks by Peacock (1999) and Peebles (1993).

2.2.1 Physical Processes during Recombination

The period of *recombination* represents the epoch when the Universe became transparent for photons. At early times before the time of recombination, the Universe was completely ionized. In this state of hot primeval plasma the photons where tightly coupled to the baryons by interactions like Compton scattering between photons and electrons and electromagnetic interactions between these electrons and protons. Because the mean free path of the photons was much shorter than the horizon scale[1] $cH(a)^{-1}$, the photons were in thermal equilibrium at this time. During the evolution of the Universe, its temperature decreased due to cosmic expansion up to some point where thermal energy was no longer high enough to keep the proton–electron plasma ionized. At this time, protons and electrons combined to form neutral hydrogen atoms and the Universe became transparent for electromagnetic radiation, i.e. the photons decoupled from matter. These photons reaching fundamental observers appear to originate from a spherical surface called the *surface of last scattering* with its radius being the distance a photon has traveled since the time of decoupling.

Equilibrium Approach In order to quantify the preceding statements, the question how the ionization rate changes with temperature needs to be addressed. The assumption of thermal equilibrium is valid if the interaction time scale in the primeval plasma is short compared to the expansion time scale of the Universe, $H(a)^{-1}$, which is a good approximation of the initial phase of the departure from complete ionization. The photoionization reaction is

$$e + p \rightleftharpoons H + \gamma, \tag{2.32}$$

[1] Here the size of the horizon is the distance ct a photon can travel in the time t since the Big Bang, where the appropriate time scale t is given by the inverse Hubble parameter, H^{-1}.

which gives rise to the relation between the chemical potentials $\mu_p + \mu_e = \mu_H$. Requiring local charge conservation ($n_e = n_p$) and using the expression for a non–relativistic and non–degenerate particle number density yields the *Saha equation*

$$\frac{x^2}{1-x} = \frac{(2\pi m_e kT)^{3/2}}{n(2\pi\hbar)^3} e^{-\frac{\Delta_{\rm ion}}{kT}}, \tag{2.33}$$

where Δ_{ion} is the ionization energy and $n = n_p + n_H$ the total proton density. This equation describes the dependence of the ionization rate $x = \frac{n_p}{n_p+n_H}$ as a function of temperature T and the proton density n.

Non–Equilibrium Approach Unfortunately, in reality the equilibrium assumption breaks down shortly after the onset of recombination. In order to solve this problem, one needs to consider rate equations describing this state of non–equilibrium.

However, there are complications arising en route. Consider a recombination directly into the ground state of a hydrogen atom, which produced a photon with $\hbar\omega > \Delta_{\rm ion}$. This photon immediately reionized another just formed neutral atom, so that the reionization needed to proceed via smaller cascade transitions. Yet even with these processes, in the last step there will be Lyman–α photons produced via the $2P \rightarrow 1S + \gamma_{{\rm Ly}\alpha}$ transition which in turn led to highly excited other hydrogen atoms by multiple absorption series of small transitions. Since the interaction rates of the electromagnetic ionization processes at these times were much higher than the expansion of the Universe, the Universe can be regarded as quasi–static and almost no redshift appeared between an emission and recombination process by the next hydrogen atom. Taking into account only these processes it appears that the decoupling of photons would have never occurred after all.

The only way out leading to recombination was the second order process $2S \rightarrow 1S + 2\gamma$, where a pair of photons was emitted in order to conserve energy and angular momentum. One individual photon of these two with wavelength $\lambda > \lambda_{{\rm Ly}\alpha}$ was not able to reionize another hydrogen atom by first order processes once relaxed to its ground state. Since this mechanism is proceeding very slowly, this broadens significantly the scattering cross section near the Lyman α–resonance. Thus, the bottom line of these considerations is, that recombinations are a two–body process being able to create excited states which decay to the $2S$–level, from where they compete with the stimulated transition rate upwards from the $2S$–state in order to decay to the ground state.

Finally, the large photon–to–baryon ratio $\eta^{-1} = \frac{n_\gamma}{n_b} \sim 10^9$, being responsible for the high occupation number of phase space volume, delays the time of decoupling furthermore until the plasma has reached a temperature of $T_{\rm dec} \approx 3300$K, which is referred to as the temperature of decoupling.

Temperature–redshift relation As long as the photons were in thermal equilibrium with electromagnetically interacting particles, their distribution was Planckian. Although the functional shape of the distribution is retained, its characteristic temperature decreased while the Universe was adiabatically expanding. This is known as

the temperature–redshift relation, for which we consider now the equation describing the adiabatically expanding Universe (2.8)

$$\mathrm{d}(\rho a^3) + p\mathrm{d}(a^3) = 0. \tag{2.34}$$

The energy density of the freely streaming photon gas can be related to the temperature using the Stefan–Boltzmann law $\rho_r = \sigma c^{-2} T^4$. Applying in addition the ultra relativistic equation of state for photons $p = \frac{1}{3}\rho$ to the Friedmann equation (2.34), it can be rewritten yielding

$$\mathrm{d}(T^4 a^3) = -\frac{1}{3} T^4 \mathrm{d}(a^3) = 0. \tag{2.35}$$

After integration, this equation reduces to the desired relation between temperature and redshift for the CMB,

$$T = t_0 \frac{a_0}{a} = T_0(1+z). \tag{2.36}$$

Inserting a value of $T_{\mathrm{dec}} \approx 3300\mathrm{K}$ for the decoupling temperature and $T_0 \approx 2.73\mathrm{K}$ for the present observed temperature, the redshift of the last scattering surface $z_{\mathrm{dec}} \approx 1100$ is obtained.

2.2.2 CMB Temperature Fluctuations

Assuming an ideally isotropic and homogeneous Universe and neglecting secondary anisotropies, the CMB temperature of $T_0 \approx 2.73\mathrm{K}$ could be measured in all directions of the sky without any fluctuations. The term *primary anisotropies* refers to temperature fluctuations being produced through density perturbations at the period of decoupling, whereas *secondary anisotropies* are generated afterwards either by gravitational effects from metric distortions or rescattering processes from reionization integrated along the photon paths. For the purpose of this work the three most important primary effects giving rise to temperature fluctuations in the CMB shall be presented qualitatively, before the mathematical framework of an analytic decomposition of the anisotropies is shown.

Sachs–Wolfe Effect If structure formation in our Universe took place via gravitational instability[2], the photon–baryon fluid, as described in the introduction to (2.2), moves in a gravitational potential before decoupling. Any potential perturbation at the time of last scattering was reflected in temperature fluctuations about its average once the photons were released, in the following way: Photons in potential troughs suffer gravitational redshift as they climb out which gives rise to a cooler region in the temperature map than the average. Conversely, photons on potential hills got gravitationally blueshifted as they decoupled, which is reflected in a warmer region in the CMB temperature map. This effect of photons being gravitationally redshifted due to metric perturbations was first studied by Sachs & Wolfe (1967).

[2] Amplification of small density perturbations due to gravitational interactions.

Acoustic Oscillations Gravitational instabilities caused matter overdensities to collapse on scales comparable to the sound horizon $c_s H(a)^{-1}$ if there was no radiation pressure acting as a restoring force in the opposite direction. The interplay between these two forces induced *acoustic oscillations* in the primeval plasma. As the Universe evolved, the sound horizon grew larger and perturbation modes of successively larger wavelengths entered the horizon. To summarize, acoustic waves with a certain wavelength were generated at precisely the time when a perturbation of the same physical size entered the sound horizon. The acoustic oscillations all ended at the same time t_{dec}, the time of decoupling, since the gravitational counterpart, the radiation pressure, was not sustained any more after decoupling of the photons. Their peculiar line of sight velocity relative to the fundamental observer caused a *Doppler shift*, which was imprinted in the CMB fluctuations. Decomposing the temperature fluctuations into spherical harmonics in order to measure the power spectrum, a distinct peak should appear at the angular scale which corresponds to the sound horizon size at the time of decoupling, followed by a harmonic series of peaks associated with acoustic oscillations at smaller scales.

Silk Damping At the smallest scales, the description of the tight coupling of the photon–baryon fluid does not quite meet reality, because there exists a non–zero mean free path of the photons to Compton scattering. So photons can diffuse out of a perturbation and drag the plasma with them either by "particle" diffusion or by a thermal process. The random walk of the photons mixes warm and cold patches of the CMB. This leads to exponential damping at the small–scale end of the power spectrum, called *Silk damping* (Silk 1977).

Angular Power Spectrum The relative temperature fluctuations of the CMB are abbreviated by

$$\frac{T(\vec{\theta}) - \langle T \rangle}{\langle T \rangle} \equiv \tau(\vec{\theta}). \tag{2.37}$$

The theory of inflation predicts that $\tau(\vec{\theta})$ is a Gaussian random field. Originating from initial vacuum fluctuations in a very early phase, they were blown up in a slightly later phase of accelerated expansion, called *inflation*, resulting in density perturbations. These perturbations gave rise to the anisotropies in the CMB as seen before. A Gaussian random field has the property of being fully determined by its first and second moments. Since the first moment of $\tau(\vec{\theta})$ is zero by definition, the important quantity to study is the *angular autocorrelation function* (or second moment)

$$\xi_T(\phi) = \left\langle \tau(\vec{\theta})\tau(\vec{\theta} + \vec{\phi}) \right\rangle, \tag{2.38}$$

where $\langle \cdots \rangle$ represents the ensemble averaging operator. It is commonly assumed, that the quantity τ has the ergodic property, i.e. taking its true ensemble average is an equivalent operation to averaging over a sufficiently large volume. This hypothesis is supported by looking at widely separated parts of the sky, which should be causally

unconnected and represent in some sense different ensembles. So in practice the average is taken over all positions on the sky $\vec{\theta}$. Assuming further a statistically isotropic process, $\xi_T(\phi)$ neither depends on the position $\vec{\theta}$ nor on the direction $\vec{\phi}$, but only on the absolute value of the separation ϕ of the correlated points.

Since the fluctuations are observed on the sky, one takes an angular decomposition of them in multipole space using

$$\phi \equiv \frac{2\pi}{2\ell + 1} \tag{2.39}$$

in contrast to the underlying three–dimensional potential fluctuations which are appropriately decomposed in Fourier space. After expanding the temperature fluctuations $\tau(\theta, \phi)$ into spherical harmonics

$$\tau(\theta, \phi) = \sum_{\ell=0}^{\infty} \sum_{m=-\ell}^{\ell} a_{\ell m} Y_\ell^m(\theta, \phi)\,, \tag{2.40}$$

the angular power spectrum of the CMB fluctuations C_ℓ is defined as the average of squared moduli of the expansion coefficients,

$$C_\ell\, \delta_{\ell,\ell'} \delta_{m,m'} \equiv \langle\, a_{\ell m} a^*_{\ell' m'} \rangle\ . \tag{2.41}$$

It can be shown that the angular correlation function $\xi_T(\phi)$ is related to the power spectrum C_ℓ through

$$C_\ell = \int_0^\pi \mathrm{d}\phi \sin(\phi) P_\ell(\cos\phi) \xi_T(\phi), \tag{2.42}$$

with the Legendre polynomials $P_\ell(\cos\phi)$.

2.3 Structure Formation

In the standard model of cosmology, the Universe was very homogeneous and isotropic at early times, whereas today we observe structures in the Universe like galaxies, clusters of galaxies and even filament–like structures on larger scales. The theory how these structures formed includes the following three main aspects: (i) The properties of the initial conditions of the density fluctuations generated by some physical mechanism which is not contained in the standard model of structure formation. Among many theories, an inflationary period would be the most promising idea relating quantum fluctuations to density perturbations (Guth (1981); Albrecht & Steinhardt (1982)). Unfortunately, the description of this mechanism is beyond the scope of this work. (ii) The nature of gravitationally interacting particle species in the Universe and their interactions leading to the growth of structures, and (iii) the time evolution of the amplitudes of the density perturbations in an expanding Universe by gravitational instability are the other two pillars. As long as the density contrast is smaller than

unity, the evolution of the perturbations can be described by linear perturbation theory assuming a homogeneous Robertson–Walker background. After quoting the main ideas of this approach, the density power spectrum will be introduced as an important ingredient for studying structure formation in both the linear and the non–linear regime.

2.3.1 Gravitationally Interacting Particle Species

The dominant interaction governing the evolution and dynamics of galaxies, clusters and large scale structure is gravitation due to the long range of its interaction and the fact that gravity is always attractive. The importance of gravitation for cosmology is supported by the growing evidence for *dark matter* constituting the major fraction of matter in our Universe today. Since dark matter is optically invisible, this implies that it has to be detected by means of its gravitational, weak or mechanical interactions. Although the astrophysical observational facts for dark matter will be presented in the next section (2.4), the main arguments in favor of it shall be mentioned here. The indirect evidence of dark matter can be seen by the gravitational effect on visible matter or radiation like the orbital motions of galaxies within clusters compared to their luminosity density, leading to a high mass–to–light ratio; in the gravitational lensing effect of background galaxies by gravitationally interacting foreground objects, the flat rotation curves in galaxies or in the analysis of peculiar velocity fields of galaxies averaged over very large scales.

Dark Baryonic Matter The baryonic matter in bright stars only accounts for 10% of the total baryonic mass today. The nature of the missing bulk of dark baryons is not known with the exception of clusters, where they exist in form of hot, x-ray emitting intracluster gas. This is just a small constraint, since clusters only account for 10% of the total matter in the Universe at the present time. By theoretical and observational reasons, the two most promising possibilities for the non-luminous baryons are diffuse hot gas and small astrophysical objects like white dwarfs, neutron stars, black holes or objects of mass below the hydrogen–burning limit (see Turner (1999) for a review). Big–Bang nucleosynthesis limits the total baryonic contribution to the critical matter density to $\Omega_b \approx 0.05$, which is approximately one order of magnitude less than the total matter density $\Omega_m \approx 0.3$ (for details and quotes please see section 2.4). In addition to this accounting argument there is much stronger evidence in favor of non–baryonic dark matter from structure formation. Except for the isocurvature baryon model by Peebles (1987), which was ruled out by its wrong prediction of the CMB power spectrum on small scales, there has been no model for structure formation without dark matter for the following reason: In models only consisting of baryons, density perturbations were only able to grow after decoupling, $z_{\rm dec} \sim 1100$, until the Universe became curvature dominated at $z \sim \Omega_b^{-1} \sim 20$. This period did not last long enough to produce all the structure observed today with the size of density perturbations inferred from the CMB anisotropies. Conversely, non–baryonic dark matter perturbations are able to begin growing much earlier and grow until the transition to a vacuum–energy dominated

age at $z_{\mathrm{eq},\Lambda} = \sqrt[3]{\Omega_\Lambda/\Omega_m} - 1 \approx 0.33$, using equation (2.11) and $\{\Omega_\Lambda, \Omega_m\} = \{0.7, 0.3\}$ (these values will be motivated in section 2.4).

Non–Baryonic Dark Matter Particle physics theories that attempt to unify the forces and particles of nature provide an interesting solution to the composition of non–baryonic dark matter: relic elementary particles left over from the big bang. In order to account for a significant fraction of the critical density ρ_{cr}, they must have the property of being stable particles with very weak interactions such that the annihilation ceased before their number density had decreased too much. The three most probable candidates are massive neutrinos (30 GeV), axions of mass $10^{-5\pm1}$ eV and neutralinos of mass of the order of 100 GeV. At the moment, the neutrino as a representative of *warm dark matter* (WDM) seems to be ruled out of accounting for the bulk of dark matter, since it predicts structure formation from the top down, starting with superclusters and subsequently separating into clusters and galaxies (White, Frenk & Davis 1983). This would contradict observational evidence that structure formed bottom up leading to the *hierarchical model* of structure formation. This scenario is corroborated by *cold dark matter models*, with its most promising candidate the lightest super symmetric particle, presumably the neutralino (see Jungman, Kamionkowski & Greist (1995) for a review). Another popular candidate would be an axion, a particle originating from a condensate of the very early Universe (Turner 1990).

2.3.2 Linear Growth of Density Perturbations

At relatively late times $a > a_{\mathrm{eq}}$, which are relevant for gravitational lensing studies, the Universe is already dominated by cold dark matter. The dark matter perturbations are denoted by the *density contrast* $\delta(\vec{x}, a)$ at the comoving position $\vec{x}$,

$$\delta(\vec{x}, a) = \frac{\rho(\vec{x}, a) - \langle\rho(a)\rangle}{\langle\rho(a)\rangle}, \tag{2.43}$$

where $\langle\rho(a)\rangle = \rho_0 a^{-3}$ is averaged over the volume of the Universe. Provided the density contrast $\delta(\vec{x}, a)$ is smaller than unity, the solution for how matter behaves under the influence of its own self–gravity can be found expanding the linearized equations of motions in the Newtonian framework, because small perturbations imply weak gravitational fields and space is locally flat. However, if the wavelength of the perturbations are of the order of the horizon scale, in general relativistic effects need to be considered due to the fact that the horizon is comparable to the curvature radius of space–time. Nevertheless, both the Newtonian and the relativistic approach yield for an adiabatic change of volume elements in the linear regime $\delta \ll 1$ the solution

$$\delta(a) \propto a^{3\omega_f+1} = \begin{cases} a^2 & \text{before } a_{\mathrm{eq}}, \quad \text{radiation dominated era:} \quad \omega_r = \frac{1}{3} \\ a & \text{after } a_{\mathrm{eq}}, \quad \text{matter dominated era:} \quad \omega_m = 0 \end{cases}, \tag{2.44}$$

as long as the Einstein–de Sitter limit holds. In the following, we will restrict our attention to the *dark matter dominated regime*, which is the only relevant one for

gravitational lensing studies. For the general case of a non–zero cosmological constant ($\Omega_m \neq 1$, $\Omega_\Lambda \neq 0$), the solution to the spherical collapse model for the amplitude of the growing perturbation mode is given by

$$\delta(a) \propto \frac{\dot{a}}{a} \int_0^a \frac{\mathrm{d}a}{(\dot{a})^3}\,, \qquad \text{if } \delta \ll 1\,, \tag{2.45}$$

according to Heath (1977), where $\dot{a}$ is given by the Friedmann equation (2.16). A very good approximation formula for the required numerical integration of equation (2.45) is given by Carroll, Press & Turner (1992)

$$\delta(a) = \delta_0 a \frac{\tilde{g}(a)}{\tilde{g}(1)} \equiv \delta_0 a g(a)\,, \tag{2.46}$$

where δ_0 is the density contrast linearly extrapolated to the present, and the density dependent growth function $\tilde{g}(a, \Omega_m, \Omega_\Lambda)$ is approximated by

$$\tilde{g}(a, \Omega_m, \Omega_\Lambda) = \frac{5}{2}\Omega_m(a) \left[\Omega_m^{4/7}(a) - \Omega_\Lambda(a) + \left(1 + \frac{\Omega_m(a)}{2}\right)\left(1 + \frac{\Omega_\Lambda(a)}{70}\right)\right]^{-1}. \tag{2.47}$$

The dependences of the density parameters Ω_m and Ω_Λ on a are given by the evolution equations (2.17) and (2.18).

2.3.3 Density Power Spectrum

In the following, only the qualitative ideas of the power spectrum approach to structure formation can be sketched, while more detailed representations and calculations can be found in Peacock (1999) and Padmanabhan (1993).

Fourier Decomposition In linear perturbation theory, the density perturbations are conveniently decomposed into Fourier modes, because these evolve independently of each other. However, this approach is strictly only valid in flat space. Fortunately, because observations seem to agree on space being flat at the present epoch (Jaffe et al. 2001), the dynamics of Friedmann's equations guarantees that space is even flatter at earlier times. This can be seen by considering the abundance of the most important fluid component in the early Universe, the radiation density

$$\Omega_r(a) = \frac{8\pi G}{3H^2(a)} \frac{\rho_r(t_0)}{a^4} = \frac{\Omega_r}{\Omega_r(1-a^2) + a^2 + \Omega_m(a-a^2) + \Omega_\Lambda(a^4-a^2)}\,, \tag{2.48}$$

which reaches unity, $\Omega_r(a) \to 1$, as $a \to 0$, which is in turn predicted by the most common variants of inflationary models. Moreover, at late times the interesting scales λ are much smaller than the curvature radius of the Universe, $cH^{-1}(a)$. Thus, a Fourier mode can be written as

$$\hat{\delta}(\vec{k}, a) \equiv |\hat{\delta}(\vec{k}, a)| e^{i\phi_{\vec{k}}} = \int \mathrm{d}^3x\, \delta(\vec{x}, a) e^{i\vec{k}\vec{x}}\,, \tag{2.49}$$

where $|\hat{\delta}(\vec{k}, a)|$ is the amplitude of the mode, $\phi_{\vec{k}}$ is the phase which is independent of time, and $\vec{x}$ is the comoving coordinate.

Qualitative Description of Processes related to the Growth of Structure A perturbation mode of a certain comoving wavelength λ enters the comoving horizon $d_H = \frac{c}{aH(a)}$ if their scales become comparable to each other and therefore causally connected. If $\lambda < d(a_{\rm eq})$, the density perturbation enters the horizon during the radiation dominated epoch at $a_{\rm enter} < a_{\rm eq}$, in which the expansion time-scale $t_{\rm exp} = H^{-1}$ is given by the radiation density ρ_r, which is shorter than the collapse time–scale of dark matter, $t_{\rm col}$:

$$t_{\rm exp} \sim \frac{1}{\sqrt{G\rho_r}} < \frac{1}{\sqrt{G\rho_{dm}}} \sim t_{\rm col} \tag{2.50}$$

This comparison shows that the radiation driven expansion prevents the collapse of dark matter perturbations within the horizon, while perturbations on larger scales are not affected by this suppression and continue to grow according to (2.44). It follows that the suppression factor for perturbations with $\lambda < d_H(a_{\rm eq})$ can be written as

$$f_{\rm sup} = \left(\frac{a_{\rm enter}}{a_{\rm eq}}\right)^2 . \tag{2.51}$$

The condition for the comoving wavelength λ entering the horizon is given by

$$\lambda = d_H(a_{\rm enter}) = \frac{c}{a_{\rm enter} H(a_{\rm enter})} . \tag{2.52}$$

Recalling the definition of $a_{\rm eq}$ in equation (2.10), $a_{\rm eq} = \Omega_r/\Omega_m$, the Hubble function in the Einstein–de Sitter regime can be approximated by

$$H(a) = H_0\sqrt{\Omega_r a^{-4} + \Omega_m a^{-3}} = H_0\,\Omega_m^{1/2} a^{-3/2}\sqrt{1 + \frac{a_{\rm eq}}{a}} . \tag{2.53}$$

Hence, inserting this expression into (2.52) yields the scaling of a perturbation mode of wavelength λ,

$$\lambda \propto \begin{cases} a_{\rm enter} & \text{for} \quad a_{\rm enter} \ll a_{\rm eq} \\ a_{\rm enter}^{1/2} & \text{for} \quad a_{\rm eq} \ll a_{\rm enter} \ll 1 \end{cases} . \tag{2.54}$$

Thus, the suppression factor (2.51) can be written using the expression for the wave number of the perturbation $k = \lambda^{-1}$ and the horizon size at the time of matter–radiation equality, $k_0 = d_H^{-1}(a_{\rm eq})$,

$$f_{\rm sup} = \left(\frac{k_0}{k}\right)^2 . \tag{2.55}$$

There is another process modifying the growth of structure if there are relativistic dark matter particles, so–called hot dark matter (HDM). The free streaming of these particles exponentially damps density perturbations, which are smaller than a certain minimum size necessary to keep them gravitationally bound.

Linear Transfer Function and Power Spectrum For convenience, the concept of the *linear transfer function* has been introduced in order to relate the linear perturbations of the mode $\vec{k}$ at a given scale factor a after matter–radiation equality $a_{\rm eq}$ to the initial perturbation mode $\vec{k_i}$. The linear transfer function for adiabatic perturbations is defined as

$$T(\vec{k},a) = \frac{1}{g(a)} \frac{|\hat{\delta}(\vec{k},a)|}{|\hat{\delta}_i(\vec{k_i},a_i)|}, \tag{2.56}$$

where $g(a)$ is the linear growth factor between scale factor a and the present (2.46) and the normalization scale factor is arbitrary, as long as it refers to a time before any scale of interest has entered the horizon. $T(\vec{k},a)$ depends only on the matter content of the Universe, e.g. HDM particles and their free streaming and on the specific cosmology, because the growth factor depends on the density parameters Ω_m and Ω_Λ. However, it does not depend on the initial amplitudes of the perturbations.

Assuming isotropic Gaussian density fluctuations $\delta(\vec{x})$, the power spectrum completely describes them. It is defined by (see also chapter 3)

$$\left\langle \hat{\delta}(\vec{k},a)\hat{\delta}^*(\vec{k},a) \right\rangle = (2\pi)^3 \delta_D(\vec{k}-\vec{k}') P_\delta(k,a) \tag{2.57}$$

and

$$P_\delta(k,a) = A(a) T^2(k,a) P_i(k,a_i)\,, \tag{2.58}$$

where $\hat{\delta}(\vec{k},a)$ is the Fourier transform of δ, the asterisk denotes complex conjugation, $A(a)$ is the normalization of the power spectrum (2.3.3) and $P_i(k,a_i) = \langle |\delta_i(k)|^2 \rangle$ is the primordial power spectrum at some very early time before any scale of interest has entered the horizon. The growth of the density contrast, $\delta \propto a^{3\omega_f+1}$ (equation (2.44)), reads in terms of the spectrum as $P_\delta \propto a^{2(3\omega_f+1)}$. At $a_{\rm enter} \ll a_{\rm eq}$, the power spectrum has therefore changed to

$$P_{\rm enter}(k) \propto a_{\rm enter}^{2(3\omega_f+1)} \propto k^{-4} P_i(k)\,, \tag{2.59}$$

using equation (2.54) for perturbation modes with wave numbers k much larger as well as much smaller than the horizon size k_0. The most common variants of inflationary models predict the total power of density perturbations at $a_{\rm enter}$ to be almost scale invariant. This implies $k^3 P_{\rm enter} = $ const., or $P_{\rm enter}(k) \propto k^{-3}$. Consequently, the primordial spectrum has to scale with k as $P_i(k) \propto k$. This *scale invariant* spectrum is called the *Harrison–Zel'dovich* power spectrum. The initial power spectrum is commonly parametrized as

$$P_i(k) \propto k^{n_s}\,, \tag{2.60}$$

which defines the spectral tilt n_s of (scalar) density perturbations. Summarizing the presented arguments, the linear power spectrum has the following asymptotic behavior at $a \gg a_{\rm eq}$,

$$P_\delta(k) \propto \begin{cases} k & \text{for} \quad k \ll k_0 \\ k^{-3} & \text{for} \quad k \gg k_0 \end{cases}\,. \tag{2.61}$$

Normalization Having discussed the shape of the power spectrum, its normalization will be considered in the following. There are primarily three different methods, normalizing the power spectrum at different scales and unfortunately also leading different answers. This representation follows the review by Bartelmann & Schneider (2001).

1. At the largest scales, normalization is done by the cosmic microwave background anisotropies which have been measured over the full sky by the DMR experiment onboard the COBE (COsmic Background Explorer) satellite at an angular scale of $\phi \sim 7^\circ$ (Banday et al. 1997). CMB temperature fluctuations can be related to density perturbations and after adopting a specific cosmology yielding a characteristic shape of the density power spectrum, it can be normalized at the comoving wave number k related to the measured angular multipole scale $\ell = f_K(w)k$ using (2.39). Since both scalar and tensor perturbations give rise to CMB temperature fluctuations, while density perturbations are *only* determined by scalar perturbations, this could lead to a possible overestimate of the normalization constant of the density power spectrum.

2. At intermediate scales of about $10h^{-1}$ Mpc, the power spectrum is normalized by the local abundance of galaxy clusters (White et al. 1993a). Since galaxy clusters formed by gravitational instability from dark matter density perturbations in the hierarchical model, the spatial number density of clusters is a measure for the amplitude of dark matter fluctuations. Requiring the power spectrum to reproduce the observed local spatial number density of clusters determines its normalization.

3. Finally, the power spectrum can be normalized by the local variance of galaxy counts, as suggested by Davis & Peebles (1983), assuming galaxies to be biased tracers of the underlying dark matter perturbations. Measuring the variance of galaxy numbers within spheres of radius $8h^{-1}$ Mpc leads to the result $\sigma_{8,\mathrm{galaxies}} \approx 1$. Assuming an expression for the bias, one can relate the variation in the galaxy counts to the dark matter fluctuations and obtains the amplitude $A(t_0)$ of the power spectrum, using (2.58) and

$$\sigma_8 \equiv \sigma(R = 8h^{-1}\ \mathrm{Mpc}, t_0) = 4\pi \int \frac{k^2 \mathrm{d}k}{(2\pi)^3} P_\delta(k) W_8^2(k) \stackrel{!}{=} 1\,. \tag{2.62}$$

   The window function $W_R(k)$ denotes the three–dimensional Fourier transform of the Heaviside function $H(R - |\vec{r}|)$,

$$W_R(k) = \frac{3[\sin(kR) - kR\cos(kR)]}{(kR)^3} = \frac{3j_1(kR)}{kR}\,, \tag{2.63}$$

   where $j_1(x)$ is the spherical Bessel function of the first kind.

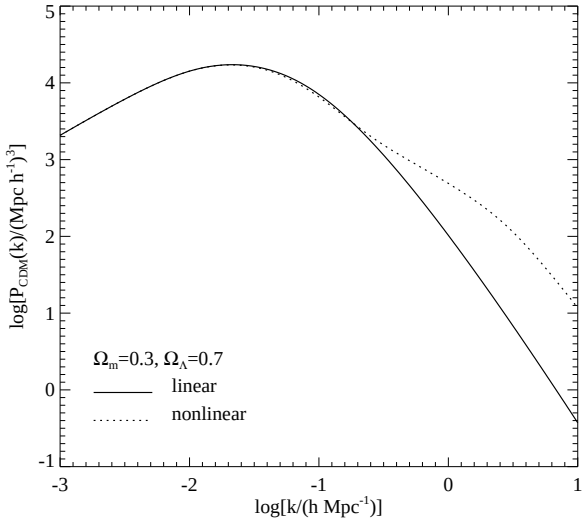

Figure 2.2: ΛCDM power spectrum of the density contrast, normalized to the local abundance of galaxy clusters using $h = 0.7$. The solid curve shows the linear, the dashed curve the non–linear power spectrum using the formula of Peacock & Dodds (1996).

2.3.4 Non–Linear Evolution

The final goal of theoretical cosmology (as it is for any other theory) is to find self–consistent physical concepts which are powerful enough to predict the evolution of the Universe and the structure formation leading to gravitationally bound objects consistent with astronomical observations. One challenge is that the objects we are able to observe in the Universe are the result of non–linear evolution, because clusters typically have a density contrast $\delta \sim 10^3$ and galaxies even have overdensities of $\delta \sim 10^6$. One way of studying the non–linear evolution is numerical integration of the equations of motion of a very large number of particles using *N–body simulations* with given initial conditions arising from linear theory, which is a reasonable approximation at high redshifts. In doing so, the gravitational forces in the Newtonian limit on one particle due to all others are computed in order to calculate the change of the particle position and velocity over a small time interval leading to a acceleration of the particle and therefore to a slightly modified gravitational potential — and the iteration is started again. In order to obtain physical intuition for the non–linear behavior seen in the simulations, semi–analytic models play an important role for a better theoretical understanding. Analytic formulae describing the non–linear behavior of $P_\delta(k)$ have been derived by Jain, Mo & White (1995) and Peacock & Dodds (1996). While the linear power spectrum declines on small scales $\propto k^{-3}$, the amplitude of the non–linear power spectrum is substantially increased on these small scales at the expense of larger–scale structure (see figure 2.2). For the largest scales the non–linear power spectrum remains unaffected. By the process of non–linear evolution non–Gaussian features

are also introduced into the density perturbations. Thus higher order moments are needed for the complete description of the statistical properties of the fields under consideration. Finally, it should be mentioned that non–linear behavior of density perturbations is important for studying weak lensing effects by large–scale structures.

2.4 Observational Constraints on Cosmological Parameters

During the previous presentation of theoretical cosmological ideas behind this work, one was clearly bound to use arguments invoking the knowledge either of the order of magnitude or the exact value of several cosmological parameters. Moreover, in order to carry out numerical simulations, cosmological parameters have to be assumed. Luckily, cosmology changed within the last decade starting from a more qualitative approach leading to quantitative science, where we for the first time have a complete accounting of matter and energy in the Universe. The following section seeks to give an overview of the latest discoveries and experiments yielding a *concordance model* of the Universe with respect to its governing parameters.

Hubble Constant and Age of the Universe The Hubble constant H_0 with its dimension of inverse time sets the scale of the size and the age of the Universe. Recent efforts to measure it have nearly solved the long–standing uncertainty concerning the extragalactic distance scales. Traditionally, the measurement of cosmological distances employs distance ladders, whose most prominent representative is the Cepheid period–luminosity relation. Applying several secondary distance methods, like the relationship between the luminosity of a spiral galaxy and its rotation velocity (*Tully–Fisher relation*) or Type Ia supernovae (SNeIa) as calibrated standard candles, the *Hubble Space Telescope* Key Project found good agreement and consistency with $H_0 = 72 \pm 8\,\mathrm{km\,s^{-1}\,Mpc^{-1}}$ (Freedman et al. 2001). Using this value, the age of the Universe can be inferred, ($\Omega_r \ll 1$),

$$t_0 = \frac{1}{H_0}\int_0^1 \frac{\mathrm{d}a}{\sqrt{a^{-1}\Omega_m + (1-\Omega_m-\Omega_\Lambda) + a^2\Omega_\Lambda}} = 13 \pm 1\mathrm{Gyr}\,, \tag{2.64}$$

using $\Omega_m = 0.3$ and $\Omega_\Lambda = 0.7$.

Curvature of the Universe The CMB temperature anisotropies offer the best means for determining the curvature of the Universe. As already discussed in section (2.2), Fourier modes of density perturbations on different scales were captured at different phases of their oscillation while their pattern was imprinted onto the CMB radiation by the Doppler effect through the process of decoupling. Using causality arguments, the largest scales are therefore unaffected by these oscillations. However, there should be a "first" Doppler peak at a location determined by the sound horizon scale at the time of decoupling. In order to infer the geometry of the Universe, one

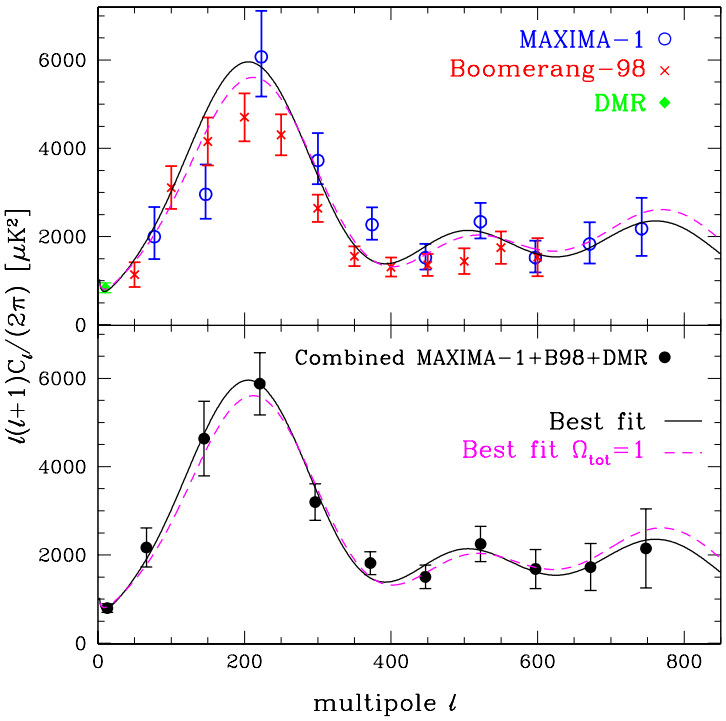

Figure 2.3: CMB power spectra, $\mathcal{C}_\ell = \ell(\ell+1)C_\ell/2\pi$. *Top panel*: MAXIMA–1, BOOMERANG-98 and COBE–DMR. *Bottom panel*: Maximum-likelihood fit to the power in multipole bands for the three spectra, marginalized over beam and calibration uncertainty. In both panels the curves show the best fit model in the joint parameter estimation with weak priors and the best fit with $\Omega_{\rm tot} = 1$. These models have $\{\Omega_{\rm tot}, \Omega_\Lambda, \Omega_b h^2, \Omega_m h^2, n_s\}$= {1.2, 0.5, 0.03, 0.15, 0.95}, {1, 0.7, 0.03, 0.20, 0.975}. From Jaffe et al. (2001)

needs to determine the comoving size of the sound horizon at the time of decoupling $d_s(a_{\rm dec})$ from considerations of physical processes before recombination and measure the multipole of the first Doppler–peak which corresponds to an angular size $\delta\phi$. Using the purely geometrical argument $d_s(a_{\rm dec}) = f_K(w)\delta\phi$ leads to the geometry of spatial hyper–surfaces. A careful analysis shows the scaling of the position of the first peak to be $\ell \simeq 200/\sqrt{\Omega_m + \Omega_\Lambda}$. Combined measurements of the angular power spectrum of the CMB by the MAXIMA and BOOMERANG balloon experiments yields $\Omega_{\rm tot} \simeq 1.11^{+0.13}_{-0.12}$ (confidence limit of 95%, Jaffe et al. (2001)), which is consistent with a flat Universe. In contrast to the model parameters in figure (2.3), the cited parameters are constrained individually by marginalising the posterior distribution over all other parameters.

Baryon Density Parameter Ω_b Following the evolution of the Universe, at temperatures of about 10^9 K nuclear reactions froze out and light elements like H, He and Li formed through *primordial big-bang nucleosynthesis* (BBN). The precise de-

termination of these light element abundances is a powerful tool for constraining the baryon density, among which deuterium gives the strongest limits, because its primeval abundance depends most strongly on the baryon–to–photon ratio $\eta = n_b/n_\gamma$. Recent results of Burles et al. (2001), using deuterium abundance measurements in four high–redshift hydrogen clouds seen in absorption against distant quasars, suggest a value of the baryon density $\Omega_b h^2 = 0.020 \pm 0.002$ at a confidence limit of 95%.

Another completely independent method to infer Ω_b involves CMB physics. Since baryons increase the effective mass and the effective pressure of the plasma, the balance between pressure and gravity is changed. This has the same effect as adding a mass to an oscillating spring which shifts the zero point of the oscillation. Thus, increasing the baryon density results in enhancing the odd numbered acoustic peaks in amplitude while simultaneously lowering the even numbered and measuring the relative height of the peaks in the power spectrum provides a way of deducing the baryon content of the Universe. Combined measurements of the angular power spectrum of the CMB by MAXIMA, BOOMERANG and COBE lead to a value of the baryon density $\Omega_b h^2 = 0.032^{+0.009}_{-0.008}$ (confidence limit of 95%, Jaffe et al. (2001)).

Density Parameter Ω_m Galaxy clusters formed by gravitational instability of density perturbations of around $10h^{-1}$ Mpc radius. Clusters are virtually closed systems which do not lose their intracluster material and gravity does not separate individual matter components during the formation of clusters. Considering their entirety, they gather a very large sample of matter, thus providing a representative sample of the whole Universe. Together with precise BBN baryon density estimates, this can be used to infer the total matter density $\Omega_m = \Omega_{\text{dark matter}} + \Omega_b$ (White et al. 1993b). According to ROSAT results (Briel et al. 1992), most of the baryons in clusters reside in the hot, x–ray emitting intracluster gas and are not bound in stars. Thus, the task of determining the baryon fraction f_b reduces to the gas–to–total mass ratio f_{ICM}. The key argument involves the following relation, which is strictly only valid for closed systems,

$$\langle f_{\text{ICM}} \rangle \equiv \frac{M_b}{M_{\text{tot}}} = \frac{\Omega_b}{\Omega_m} \,. \tag{2.65}$$

Assuming hydrostatic equilibrium of the gas, the gas mass M_b is determined using x–ray flux measurements from intracluster gas.

The total cluster mass M_{tot} can be obtained by using three independent methods, which agree within their uncertainties: (i) Using the dynamics of galaxies employing the virial theorem, (ii) using x–ray observations while assuming that the gas is in hydrostatic equilibrium and applying the virial theorem for the gas; and (iii) mapping the cluster mass by gravitational lensing. Mohr, Mathiesen & Evrard (1999) have compiled the gas–to–total mass ratio determined from x–ray flux limited measurements for a sample of 45 clusters, yielding the result $\langle f_{\text{ICM}} \rangle = (0.075 \pm 0.002) h^{-3/2}$. Inserting the baryon density parameter $\Omega_b = (0.020 \pm 0.002) h^{-2}$ of Burles et al. (2001) into (2.65)

constrains the clustered mass density parameter to

$$\Omega_m \leq \frac{\Omega_b}{\langle f_{\rm ICM}\rangle} = (0.31 \pm 0.02)\left(\frac{0.72}{h}\right)^{1/2}. \tag{2.66}$$

A more traditional approach to estimating the matter density involves the average mass–to–light ratio of clusters and the measured luminosity density $\mathcal{L}$ of the Universe. Using the following equation

$$\langle \rho_m \rangle = \left\langle \frac{M}{L} \right\rangle \mathcal{L}\,, \tag{2.67}$$

and dividing it by the critical density $\rho_{\rm cr}$ yields Ω_m. The CNOC group (Carlberg et al. 1997) determined the mean cluster mass–to–light ratio $(\langle M/L\rangle)_{\rm cluster} = (240\pm50)M_\odot/L_\odot$. Assuming clusters are a "fair sample" of the Universe, they find a mean matter density $\Omega_{\rm cluster} = 0.20 \pm 0.04$, which differs substantially from the other result. However, this approach contains large systematic uncertainties such that this result should not be taken too seriously: (i) Why should M/L in clusters be representative of M/L of the Universe, since only the fraction of galaxies in clusters are taken into consideration and field galaxies are neglected. (ii) Moreover, since we are at the tail end of star formation at the present time, the luminosity density $\mathcal{L}$ evolves strongly with redshift such that large corrections for this effect have to be assumed leading to larger uncertainties. (iii) Finally, mass–to–light ratios are usually measured at blue wavelengths such that the integrated history of star formation is downweighted and the present star formation rate is emphasized.

Relativistic Matter Components Today, we can observe two relativistic matter components in the Universe, photons and neutrinos. The major part of the energy density contained in the photons is determined by the temperature of the cosmic microwave background, $T_{\rm CMB} = 2.725\,{\rm K}$ (Mather et al. 1999). Since the CMB has a black–body spectrum, its energy density is given by the Stefan–Boltzmann law,

$$\rho_{\rm CMB} = \frac{1}{c^2}\frac{\pi^2}{15}\frac{(kT_{\rm CMB})^4}{(\hbar c)^3} \approx 4.5\cdot 10^{-34}{\rm g\,cm^{-3}}\,. \tag{2.68}$$

Dividing by the critical energy density ρ_{cr} defined in (2.12) yields the density parameter of photon background at the present epoch,

$$\Omega_{\rm CMB} = 2.4\cdot 10^{-5}h^{-2}\,. \tag{2.69}$$

The neutrinos were also produced in thermal equilibrium in the hot early phase of the Universe. Compared to the photons, they decoupled earlier from the cosmic plasma at a higher temperature of $kT \approx 1$ MeV, when their weak interaction time–scale exceeded the expansion time–scale of the Universe, the local Hubble time. Because their equilibrium could no longer be maintained this leaves behind the abundance of particles at their freeze–out time. Following Peacock (1999) and assuming three

relativistic neutrino species, the total density parameter in relativistic matter today is

$$\Omega_r = \Omega_{\mathrm{CMB}} + 3 \cdot \Omega_\nu = 3.2 \cdot 10^{-5} h^{-2} \,, \tag{2.70}$$

which has a negligible contribution to the energy density of the Universe. However, this assumes a negligible mass of the neutrinos. If this is not the case, the neutrino density will have a larger contribution to the total density parameter Ω_{tot} of the Universe. According to the discussion in section (2.3.1), there has to be an upper bound to the neutrino contribution in form of WDM in order not to violate structure formation models.

Cosmological Constant Ω_Λ The results presented above, $\Omega_{\mathrm{tot}} = 1.1 \pm 0.2$ and $\Omega_m = 0.3 \pm 0.1$ seem to contradict each other unless there exists some dark, exotic form of energy. To avoid conflicts with structure formation starting from anisotropies in the CMB, which were precisely measured, requires the Universe to be matter dominated until $z_{\mathrm{eq},\Lambda} \approx 0.33$ assuming a flat ΛCDM Universe (equation (2.11)). As already discussed in section (2.1.3), one example of a smooth energy component would be the cosmological constant with an equation of state characterized by $\omega_\Lambda = -1$. Such an energy component with negative pressure would cause an accelerated expansion of the Universe, once it dominates over the other fluid components, or more exactly, according to equation (2.19)

$$q_0 = \frac{1}{2}(\Omega_m + \Omega_r) - \frac{3}{2}\Omega_\Lambda < 0 \,. \tag{2.71}$$

Independly of those strong arguments in favor of a cosmological constant, recently two independent groups succeeded in finding evidence for an accelerated expansion of the Universe. Perlmutter et al. (1998) and Riess et al. (1998) measured the magnitude–redshift (Hubble) diagram for about fifty SNeIa out to redshifts of nearly unity. The high redshift SNeIa seem to be systematically dimmer as would be expected in a Universe without a cosmological constant (see figure 2.72). Since the intrinsic scatter in the sample is larger than the deviation, one should be extremely cautious considering the possibility of systematic errors, e.g. possible evolution effects of the chemical composition of the SNeIa progenitor stars or hypothetical grey dust leading to a dimming of the SNeIa. But no such systematic effects have been found so far. The results of these groups can be summarized as

$$\Omega_\Lambda = \frac{4}{3}\Omega_m + \frac{1}{3} \pm \frac{1}{6} \,, \tag{2.72}$$

which implies $\Omega_\Lambda \simeq 0.7 \pm 0.3$ for $\Omega_m \simeq 0.3 \pm 0.1$. They exclude the possibility of a vanishing cosmological constant at a high confidence level (see figure 2.72).

Conclusion In order to summarize this section, the choice of the cosmological parameters for the successive simulations shall be presented. The result is the so–called ΛCDM Universe with the Hubble constant $H_0 = 70\,\mathrm{km\,s^{-1}\,Mpc^{-1}}$. The spatial curvature is assumed to be zero, which is also preferred by the most common variants of

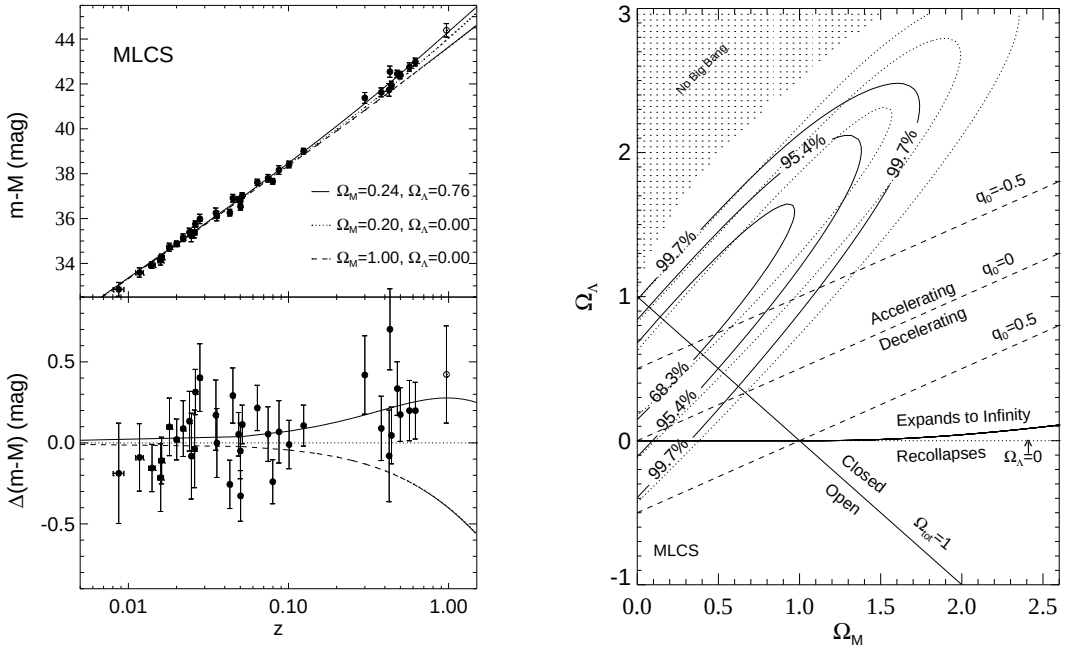

Figure 2.4: Constraints on the matter density Ω_m of the Universe and the cosmological constant parameter Ω_Λ by brightness measurements of high-redshift SNeIa. From Riess et al. (1998)

---

inflationary models. The density parameters are taken to be $\Omega_m = 0.3$ and $\Omega_\Lambda = 0.7$. Finally, for the simulations of the CMB fluctuations, the baryon density is adopted to $\Omega_b h^2 = 0.024$.

3 Correlation Functions and Power Spectra

Before introducing the theory of gravitational lensing, an essential and important tool for studying the lensing properties will be presented in this chapter, namely second order statistics like correlation functions and power spectra of random fields. In the following, a relation between the power spectra of homogeneous and isotropic random fields in three dimensions and their projection onto two dimensions will be derived, the so–called *Limber's equation*. Finally, the correspondence between the power spectrum in Fourier space and its analogue on the sphere in multipole space will be shown. The first two parts follow Bartelmann & Schneider (2001), whereas the last one is based on a paper by Hu (2000).

3.1 Definitions of Correlation Functions and Power Spectra

Without loss of generality, we consider a random field $g(\vec{x})$ in n dimensions with zero expectation value everywhere in space, $\langle g(\vec{x})\rangle = 0$. Otherwise a new random field would be defined from the old one as $g(\vec{x}) - \langle g(\vec{x})\rangle$ with the requested property. Furthermore, it is assumed that $g(\vec{x})$ has the ergodic property, already discussed in (2.2.2), and that it is statistically homogeneous and isotropic. In other words, the field $g(\vec{x})$ is statistically invariant under arbitrary translations and rotations in space. With these restrictions, the *two–point correlation function* (auto–correlation function)

$$\langle g(\vec{x})g^*(\vec{y})\rangle = \xi_{gg}(|\vec{x}-\vec{y}|) \tag{3.1}$$

can only depend on the absolute value of the difference vector between $\vec{x}$ and $\vec{y}$. The assumed ergodicity of $g(\vec{x})$ permits taking spatial averages over sufficiently large volumes in $\mathbb{R}^n$ instead of performing the ensemble average. The Fourier transform is defined by

$$\hat{g}(\vec{k}) = \int\limits_{\mathbb{R}^n} \mathrm{d}^n x\, g(\vec{x}) e^{\mathrm{i}\vec{x}\cdot\vec{k}} \qquad \text{and} \qquad g(\vec{x}) = \int\limits_{\mathbb{R}^n} \frac{\mathrm{d}^n k}{(2\pi)^n} \hat{g}(\vec{k}) e^{-\mathrm{i}\vec{x}\cdot\vec{k}}\,. \tag{3.2}$$

Inserting these Fourier expansions in order to calculate the autocorrelation function in Fourier space leads to

$$\left\langle \hat{g}(\vec{k})\hat{g}^*(\vec{k}')\right\rangle = \int\limits_{\mathbb{R}^n} \mathrm{d}^n x\, e^{\mathrm{i}\vec{x}\cdot\vec{k}} \int\limits_{\mathbb{R}^n} \mathrm{d}^n x'\, e^{-\mathrm{i}\vec{x}'\cdot\vec{k}'} \left\langle g(\vec{x})g^*(\vec{x}')\right\rangle . \tag{3.3}$$

Using the integral representation formula for the Dirac delta distribution,

$$\int\limits_{\mathbb{R}^n} \mathrm{d}^n x\, e^{\mathrm{i}(\vec{k}-\vec{k}')\cdot\vec{x}} = (2\pi)^n \delta_D(\vec{k}-\vec{k}')\,, \tag{3.4}$$

as well as equation (3.1), the correlation function in Fourier space can be written as follows after substituting $\vec{x}' = \vec{x} + \vec{y}$:

$$\begin{aligned}\left\langle \hat{g}(\vec{k})\hat{g}^*(\vec{k}')\right\rangle &= \int\limits_{\mathbb{R}^n} \mathrm{d}^n x\, e^{\mathrm{i}\vec{x}\cdot\vec{k}} \int\limits_{\mathbb{R}^n} \mathrm{d}^n y\, e^{-\mathrm{i}(\vec{x}+\vec{y})\cdot\vec{k}'} \xi_{gg}(|\vec{y}|) \\ &= (2\pi)^n \delta_D(\vec{k}-\vec{k}') \int\limits_{\mathbb{R}^n} \mathrm{d}^n y\, e^{-\mathrm{i}\vec{y}\cdot\vec{k}'} \xi_{gg}(|\vec{y}|) \\ &\equiv (2\pi)^n \delta_D(\vec{k}-\vec{k}') P_g(|\vec{k}|)\,. \end{aligned} \tag{3.5}$$

In the last step, the power spectrum of an isotropic and homogeneous random field was defined as

$$P_g(|\vec{k}|) \equiv \int\limits_{\mathbb{R}^n} \mathrm{d}^n y\, e^{-\mathrm{i}\vec{y}\cdot\vec{k}} \xi_{gg}(|\vec{y}|)\,, \tag{3.6}$$

which is the Fourier transform of the two–point correlation function.

Gaussian random fields $g(\vec{x})$ are defined such that their probability distribution is Gaussian. This is the case if the phases of the individual Fourier modes $\hat{g}(\vec{k})$ are uncorrelated and random, i.e. mutually statistically independent, since the central limit theorem states that the sum of a large number of independent random variables drawn from the same distribution tends to be normally distributed in the limit to infinity provided the variance of the distribution is finite. It follows that the probability densities for the $\hat{g}(\vec{k})$ are Gaussian with dispersion $P_g(|\vec{k}|)$. Therefore, a Gaussian random field with vanishing expectation value is fully determined by its power spectrum.

3.2 Limber's Equation

Density perturbations are defined to "live" in three dimensions whereas lensing quantities like the effective convergence are confined to two dimensions on the sphere. Therefore, a relation needs to be derived between the power spectrum of a homogeneous and isotropic random field in three dimensions, preferably the density contrast $\delta[f_K(w)\vec{\theta}, w]$ and its projection onto two dimensions. Since $\vec{\theta}$ is a two–dimensional vector on the sky, $f_K(w)\vec{\theta}$ and w constitute a local comoving Cartesian coordinate

system. Two different projections of δ are defined along the past light cone of the observer at $w = 0$ to the source at w_s,

$$g_i(\vec{\theta}) = \int_0^{w_s} \mathrm{d}w\, q_i(w)\delta[f_K(w)\vec{\theta}, w] \qquad \text{with} \qquad i = 1, 2\,, \tag{3.7}$$

which differ only by the weight functions $q_i(w)$. The cross correlation function of these two projections reads

$$\begin{aligned} \xi_{12}(|\vec{\theta} - \vec{\theta}'|) &= \left\langle g_1(\vec{\theta}) g_2(\vec{\theta}') \right\rangle \\ &= \int \mathrm{d}w\, q_1(w) \int \mathrm{d}w'\, q_2(w') \left\langle \delta[f_K(w)\vec{\theta}, w]\delta[f_K(w')\vec{\theta}', w'] \right\rangle . \end{aligned} \tag{3.8}$$

Replacing the density contrast δ by its Fourier transform using the expansions in (3.2) yields

$$\begin{aligned} \xi_{12}(|\vec{\theta} - \vec{\theta}'|) &= \int \mathrm{d}w\, q_1(w) \int \mathrm{d}w'\, q_2(w') \int \frac{\mathrm{d}^3k}{(2\pi)^3} \int \frac{\mathrm{d}^3k'}{(2\pi)^3} \\ &\times \left\langle \hat{\delta}(\vec{k}, w)\hat{\delta}^*(\vec{k}', w') \right\rangle e^{-\mathrm{i}f_K(w)\vec{k}_\perp\cdot\vec{\theta}} e^{\mathrm{i}f_K(w')\vec{k}'_\perp\cdot\vec{\theta}'} e^{-\mathrm{i}k_3 w} e^{-\mathrm{i}k'_3 w'} . \end{aligned} \tag{3.9}$$

Here, the three dimensional wave vector $\vec{k}$ is decomposed into a two–dimensional part $\vec{k}_\perp$ perpendicular to the line of sight and one component parallel to it. For proceeding further it is commonly assumed that there is no power in the density perturbations on scales larger than L_{coh} which is justified by the scaling of the power spectrum $P_\delta \propto k$ as $k \to 0$. This implies that the correlator on the right–hand side of equation (3.9) vanishes for $w_H \gg |w - w'| \gtrsim L_{\mathrm{coh}}$. Despite its cosmological evolution, the density contrast is considered constant over the light–crossing time of the comoving distance scale L_{coh}, such that $\hat{\delta}(\vec{k}, w) \approx \hat{\delta}(\vec{k}, w')$. Moreover, one requires that the variation of the weight functions $q_i(w)$ is negligible over the scale $\Delta w = |w - w'| \lesssim L_{\mathrm{coh}}$ where the correlation function ξ_{gg} is non–zero such that $q_2(w') \approx q_2(w)$ and $f_K(w') \approx f_K(w)$. Using these approximations, we can replace the correlator by the power spectrum using (3.5) which introduces a Dirac delta distribution $\delta_D(\vec{k} - \vec{k}')$, which permits performing the $\vec{k}'$–integration and establishes

$$\xi_{12} = \int \mathrm{d}w\, q_1(w) q_2(w) \int \frac{\mathrm{d}^3k}{(2\pi)^3} P_\delta(|\vec{k}|, w) e^{-\mathrm{i}f_K(w)\vec{k}_\perp\cdot(\vec{\theta}-\vec{\theta}')} e^{-\mathrm{i}k_3 w} \int \mathrm{d}w'\, e^{\mathrm{i}k_3 w'} . \tag{3.10}$$

Carrying out the w'–integration leads to $2\pi\delta_D(k_3)$. This indicates that only those modes perpendicular to the line of sight contribute to the projected power spectrum. Using the notations $\Delta\vec{\theta} \equiv \vec{\theta} - \vec{\theta}' \to \vec{\theta}$ and $\mathrm{d}^3k = \mathrm{d}^2k_\perp \mathrm{d}k_3$, the k_3–integration yields

$$\xi_{12}(\Delta\theta) = \int \mathrm{d}w\, q_1(w) q_2(w) \int \frac{\mathrm{d}^2k_\perp}{(2\pi)^2} P_\delta(|\vec{k}_\perp|, w) e^{-\mathrm{i}f_K(w)\vec{k}_\perp\cdot\vec{\theta}} \tag{3.11}$$

$$= \int \mathrm{d}w\, q_1(w) q_2(w) \int \frac{k_\perp \mathrm{d}k_\perp}{2\pi} P_\delta(k_\perp, w) J_0(f_K(w)\theta\, k_\perp) \tag{3.12}$$

In the final step, the integral representation of Bessel functions of the first kind has been used (Abramowitz & Stegun (1984), eq. 9.1.18),

$$J_0(f_K(w)\theta\, k_\perp) = \int_0^{2\pi} \frac{\mathrm{d}\phi}{2\pi} \cos[f_K(w)\theta\, k_\perp \cos(\phi)]\,, \tag{3.13}$$

where ϕ is chosen to be the angle between $\vec{k}_\perp$ and $\vec{\theta}$, and the integral over the imaginary part of the exponential over one period vanishes. In order to obtain the projected power spectrum, relation (3.6) needs to be applied to (3.11), finally establishing the result

$$\begin{aligned} P_{12}(l) &\equiv \int \mathrm{d}^2\theta\, \xi_{12}(\theta) e^{\mathrm{i}\vec{\ell}\cdot\vec{\theta}} \\ &= \int \mathrm{d}w\, q_1(w) q_2(w) \int \frac{\mathrm{d}^2 k_\perp}{(2\pi)^2} P_\delta\left(|\vec{k}_\perp|, w\right) (2\pi)^2 \delta_D\left[\vec{\ell} - f_K(w)\vec{k}_\perp\right] \\ &= \int \mathrm{d}w \frac{q_1(w) q_2(w)}{f_K^2(w)} P_\delta\left(\frac{\ell}{f_K(w)}, w\right)\,. \end{aligned} \tag{3.14}$$

Here the wave vector $\vec{\ell}$ is the conjugate Fourier variable of $\vec{\theta}$. Besides, the following representation of the Dirac delta distribution was used,

$$\delta_D[f(x)] = \sum_{x_s} \frac{\delta_D(x - x_s)}{|f'(x_s)|} \qquad \text{with} \qquad f(x_s) = 0\,, \tag{3.15}$$

which only holds in the case of single valued zeros x_s of $f(x)$.

3.3 Flat and All Sky Correspondence

Usually, the CMB temperature fluctuations are decomposed into spherical harmonics for studying their statistical properties as shown in (2.2.2). Weak gravitational lensing affects the CMB only on small angular scales (see figure 4.2) such that the flat sky approximation for small angular scales is suitably taken by replacing spherical harmonics with Fourier harmonics. In the flat sky approximation, the spherical polar coordinates (θ, ϕ) are replaced by radial coordinates on the tangential plane: $r \equiv 2\sin\frac{\theta}{2} \approx \theta$ and ϕ_r.

Recall the decomposition of the temperature fluctuations $\tau(\theta, \phi)$ into spherical harmonics (2.40),

$$\tau(\theta, \phi) = \sum_{\ell=0}^{\infty} \sum_{m=-\ell}^{\ell} a_{\ell m} Y_\ell^m(\theta, \phi)\,. \tag{3.16}$$

In the following, the weighted sum over the multipole moments $a_{\ell m}$ and its inverse relation is introduced by

$$\begin{aligned} a(\vec{\ell}) &\equiv \sqrt{\frac{4\pi}{2\ell+1}} \sum_{m=-\ell}^{\ell} \mathrm{i}^{-m} a_{\ell m} e^{\mathrm{i}m\phi_\ell} \\ \text{and} \qquad a_{\ell m} &\equiv \sqrt{\frac{2\ell+1}{4\pi}} \mathrm{i}^m \int \frac{\mathrm{d}\phi_\ell}{2\pi} e^{-\mathrm{i}m\phi_\ell} a(\vec{\ell})\,, \end{aligned} \tag{3.17}$$

where the two–dimensional vector $\vec{\ell}$ has the length ℓ and azimuthal angle ϕ_ℓ.

For small angles around the pole and small scales ($\ell \gg 1$), the spherical harmonics are approximated using Gradshteyn & Ryzhik (1980) (eq. 8.722)

$$Y_\ell^m(\theta,\phi) \approx J_m(l\theta)\sqrt{\frac{\ell}{2\pi}}e^{\mathrm{i}m\phi} \qquad \text{for} \qquad \theta \ll 1 \quad \text{and} \quad \ell \gg 1\,, \tag{3.18}$$

where J_m is the Bessel function of the first kind. Using this approximation and the formula of Gradshteyn & Ryzhik (1980) (eq. 8.511), the plane waves can be expanded into

$$e^{\mathrm{i}\vec{\ell}\cdot\vec{\theta}} = \sum_{m=-\ell}^{\ell} \mathrm{i}^m J_m(\ell\theta)e^{\mathrm{i}m(\phi-\phi_\ell)} \approx \sqrt{\frac{2\pi}{\ell}} \sum_{m=-\ell}^{\ell} \mathrm{i}^m Y_\ell^m(\theta,\phi)e^{\mathrm{i}m\phi_\ell}\,. \tag{3.19}$$

The desired correspondence between the flat and the angular power spectra is then derived from the relationship of the multipole moments, using definition (3.17) and (3.5)

$$\langle a_{\ell m} a^*_{\ell' m'}\rangle \approx \mathrm{i}^{m'-m}\frac{\sqrt{\ell\ell'}}{2\pi}P(\ell)\int \mathrm{d}\phi_\ell\, e^{\mathrm{i}m\phi_\ell}\int \mathrm{d}\phi_{\ell'}\, e^{-\mathrm{i}m'\phi_{\ell'}}\delta_D(\vec{\ell}-\vec{\ell}') \tag{3.20}$$

Expanding the delta distribution into plane waves

$$\delta_D(\vec{\ell}-\vec{\ell}') = \int \frac{\mathrm{d}^2\theta}{(2\pi)^2}e^{\mathrm{i}(\vec{\ell}-\vec{\ell}')\cdot\vec{\theta}}\,, \tag{3.21}$$

inserting the approximation (3.19) and integrating over the azimuthal angles $\phi_\ell, \phi_{\ell'}$ collapses the sum to

$$\langle a_{\ell m} a^*_{\ell' m'}\rangle \equiv \delta_{\ell,\ell'}\delta_{m,m'}C_\ell \approx P(\ell)\int \mathrm{d}^2\theta\, Y_\ell^{-m*}Y_{\ell'}^{-m'} = \delta_{\ell,\ell'}\delta_{m,m'}P(\ell)\,. \tag{3.22}$$

In the final step, the orthogonality relation on the sphere has been used. This proves the equality of the two–dimensional flat power spectrum and its angular analogue for small scales ($\ell \gg 1$),

$$C_\ell \approx P(\ell)\,. \tag{3.23}$$

4 Gravitational Lensing

In this chapter the theoretical foundations of gravitational lensing which are necessary for the scope of this work shall be presented. In general, light propagation in arbitrary curved space–time along null geodesics is a difficult problem to solve. However, in most astrophysically relevant situations, there exists an approximate description for light deflection, the *gravitational lens theory*, the important concepts of which will be presented first. This approach holds as long as the dimensions of the lensing objects are not extended over a large fraction of the line of sight between the source and the observer. However, if the mass is distributed on cosmic scales along the line of sight, a more general and thorough description of light propagation is needed. This will be outlined in the following section. Eventually, the basic ideas of cosmological lensing of the CMB photons will be described in the last section. This presentation follows mainly Schneider, Ehlers & Falco (1992), Bartelmann & Schneider (2001) and Narayan & Bartelmann (1995).

4.1 Lensing by Individual Objects

The theory presented in this section is based on two main assumptions: (i) The Newtonian limit of a slowly varying gravitational field is taken from Einstein's field equations, namely $|\Phi| \ll c^2$ and $|v_{\rm lens}| \ll c$, in order to characterize the properties of lenses, and (ii) the lensing objects are considered to be thin, i.e. the deflecting mass is isolated and concentrated within a region L much smaller than the distances between source and deflector and deflector and observer, $L \ll cH_0^{-1}$. This approximation holds remarkably well in the astrophysical cases of galaxies or clusters of galaxies.

4.1.1 Deflection Angle α

Linearizing the gravitational field equations and taking non–relativistic sources results in the "post–Minkowskian" metric to first order, neglecting the gravitational vector potential,

$$\mathrm{d}s^2 = \left(1 + \frac{2\Phi}{c^2}\right) c^2 \mathrm{d}t^2 - \left(1 - \frac{2\Phi}{c^2}\right) \mathrm{d}\vec{r}^{\,2}\,, \tag{4.1}$$

where Φ represents the Newtonian potential and $\mathrm{d}\vec{r}$ characterizes the spatial part of the Minkowski metric. Using the fact that light propagates on null geodesics, namely $\mathrm{d}s^2 = 0$, yields an effective velocity of light c' in the presence of a weak gravitational

field,

$$c' = \frac{|\mathrm{d}\vec{r}|}{\mathrm{d}t} \simeq c\left(1 + \frac{2\Phi}{c^2}\right) \equiv \frac{c}{n}\,, \tag{4.2}$$

$$n = \left(1 - \frac{2\Phi}{c^2}\right) \geq 1\,, \tag{4.3}$$

which defines an *effective index of refraction* n of the gravitational field in analogy to geometrical optics in dense media. Note that the gravitational potential Φ is by definition negative as it represents an attractive gravitational force. Applying Fermat's principle leads to an equation for the spatial light paths by using the Euler–Lagrange equations for carrying out the variation

$$\delta \int_A^B n\,\mathrm{d}l = \delta \int_A^B n(\vec{r})\sqrt{|\dot{\vec{r}}|^2}\,\mathrm{d}\lambda \stackrel{!}{=} 0 \tag{4.4}$$

$$\text{or} \qquad \ddot{\vec{r}} = -\frac{2}{c^2}\vec{\nabla}_\perp \Phi(\vec{r}), \tag{4.5}$$

where the different curves are parametrized by the affine curve parameter λ, the dot denotes a derivative with respect to λ and $\vec{\nabla}_\perp \Phi(\vec{r})$ is the gradient of the potential perpendicular to the perturbed light ray. The total deflection is therefore the integral along the light path of the differential displacements,

$$\vec{\hat{\alpha}}(\vec{r}) = -\int \vec{\nabla}_\perp n(\vec{r})\,\mathrm{d}l = \frac{2}{c^2}\int \vec{\nabla}_\perp \Phi(\vec{r})\,\mathrm{d}l\,. \tag{4.6}$$

Because in nearly all cases of astrophysical interest the deflection angle is small, $\vec{\hat{\alpha}} \ll 1$, one usually applies the "Born approximation" and evaluates the integral along the unperturbed ray, i.e. along a straight line. Since the non–relativistic matter is characterized by its density perturbations only, the gravitational potential which gives rise to light deflections (4.6) neither depends on the actual nature of matter nor its composition or physical state. Therefore gravitational light deflection probes the total matter density of gravitationally interacting particles irrespective of baryonic and dark matter.

4.1.2 The Lens Equation

The lensing equation relates the intrinsic angular source position of an astrophysical object to its observable image position on the sky which was possibly changed in the presence of gravitational light deflection along the line of sight. In order to derive this equation in the thin screen approximation, it is useful first to consider lensing by a point mass. The Newtonian potential as well as its perpendicular gradient can be written as

$$\Phi(\vec{\xi}, r_3) = -\frac{GM}{\sqrt{\xi^2 + r_3^2}} \tag{4.7}$$

$$\text{and} \qquad \vec{\nabla}_\perp \Phi(\vec{\xi}, r_3) = \frac{GM\vec{\xi}}{(\xi^2 + r_3^2)^{3/2}}\,, \tag{4.8}$$

where the tree dimensional vector $\vec{r}$ is decomposed into the r_3–coordinate along the unperturbed ray and the two dimensional impact parameter $\vec{\xi}$ orthogonal to the unperturbed ray pointing towards the point mass. Equation (4.6) leads to the deflection angle

$$\vec{\hat{\alpha}}(\vec{\xi}) = \frac{2}{c^2}\int_{-\infty}^{\infty} \frac{GM\vec{\xi}}{(\xi^2 + r_3^2)^{3/2}}\,\mathrm{d}r_3 = \frac{4GM}{c^2\xi}\frac{\vec{\xi}}{|\vec{\xi}|} = \frac{2R_S}{\xi}\frac{\vec{\xi}}{|\vec{\xi}|}\,, \tag{4.9}$$

with R_S being the Schwarzschild radius of the point mass. The Born approximation in this context makes sure that the integral is evaluated along the straight coordinate line r_3.

If we now consider extended objects acting as lenses, but still located within a small region compared to the total distance between lens and observer, the mass distribution of the lensing object can be projected along the line of sight. The smooth three–dimensional distribution can then be replaced by a mass layer perpendicular to the line of sight, which is called *lens plane*. The surface mass density on the lens plane is given by

$$\Sigma(\vec{\xi}) = \int \rho(\vec{\xi}, r_3)\,\mathrm{d}r_3\,, \tag{4.10}$$

and the deflection angle at position $\vec{\xi}$ is the overall deflection effect due to a superposition of "point–mass" elements in the plane because of linearity of the system:

$$\vec{\hat{\alpha}}(\vec{\xi}) = \frac{4G}{c^2}\int \frac{\Sigma(\vec{\xi}')(\vec{\xi} - \vec{\xi}')}{|\vec{\xi} - \vec{\xi}'|^2}\,\mathrm{d}^2\xi'\,. \tag{4.11}$$

This equation holds in the lens plane with the impact parameter measured in physical units. Assuming the small angle approximation, the *lens equation* relates the position of the source to the observable image position on the sky. The geometry of a typical gravitational lens system is shown in figure (4.1).

The true position of the source with respect to some arbitrarily chosen optical axis is denoted by $\vec{\beta}$ and the angular image position on the sky as viewed by an observer is given by $\vec{\theta}$. All distances along the line of sight are angular diameter distances (2.30), where D_{ls} denotes the distance between lens and source, D_l the distance between lens and observer and D_s the distance between source and observer. Using the relation $\vec{\xi} \simeq D_l\vec{\theta}$ and introducing the reduced deflection angle, $\vec{\alpha}(\vec{\theta}) = \frac{D_{ls}}{D_s}\vec{\hat{\alpha}}(\vec{\theta})$, equation (4.11) can be written as

$$\vec{\alpha}(\vec{\theta}) = \frac{4G}{c^2}\frac{D_l D_{ls}}{D_s}\int \frac{\Sigma(\vec{\theta}')(\vec{\theta} - \vec{\theta}')}{|\vec{\theta} - \vec{\theta}'|^2}\,\mathrm{d}^2\theta'\,. \tag{4.12}$$

The critical surface mass density Σ_{cr} and the convergence κ are defined by

$$\Sigma_{\mathrm{cr}} \equiv \left(\frac{4\pi G}{c^2}\frac{D_l D_{ls}}{D_s}\right)^{-1} \qquad \text{and} \qquad \kappa \equiv \frac{\Sigma}{\Sigma_{\mathrm{cr}}}\,. \tag{4.13}$$

It is important to note that the distance combination appearing in equation (4.12), $\frac{D_l D_{ls}}{D_s}$, acts as a lensing efficiency function. It approaches zero at both the source and

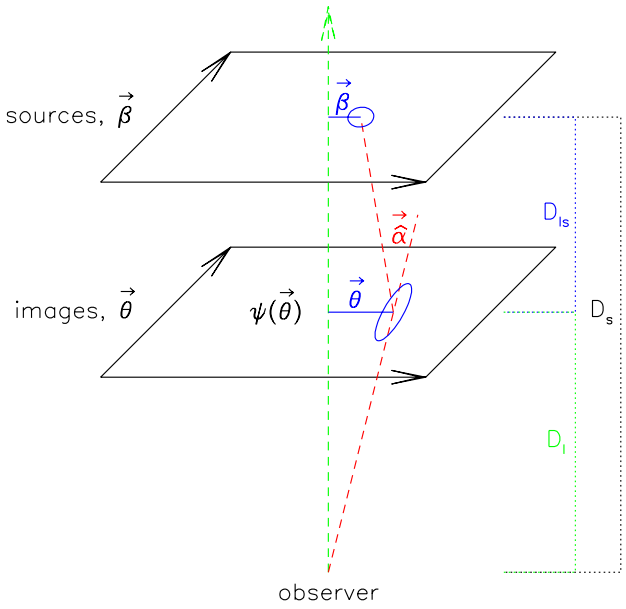

Figure 4.1: Illustration of a typical gravitational lens system. The angles are exaggerated for all your creative comfort.

---

the observer and has a maximum in between. Using definitions (4.13), the deflection angle as a function of the image position $\vec{\theta}$ reduces to

$$\vec{\alpha}(\vec{\theta}) = \frac{1}{\pi} \int \kappa(\vec{\theta'}) \frac{\vec{\theta} - \vec{\theta'}}{|\vec{\theta} - \vec{\theta'}|^2} \, \mathrm{d}^2\theta' \,. \tag{4.14}$$

This equation shows that only the ration of Σ and Σ_{cr} is measurable, or in other words, using gravitational lensing on its own, one is not able to determine both the mass of a lensing object and the involved distances independently. From figure (4.1) we can read off $\vec{\theta} D_s - \vec{\hat{\alpha}} D_{ls} = \vec{\beta} D_s$, assuming the small angle approximation and using the theorem on intersecting lines. Using the expression for the reduced deflection angle, this establishes the *lens equation* in its simplest form

$$\vec{\beta} = \vec{\theta} - \vec{\alpha}(\vec{\theta}) \,. \tag{4.15}$$

In general, this equation is nonlinear and can thus yield multiple images on the sky for a single source position $\vec{\beta}$. Moreover, the shape and the size of the images will differ from the original source because light bundles are deflected differentially.

4.1.3 The Lensing Potential Ψ

It is convenient to define the lensing potential $\Psi(\vec{\theta})$ which is the scaled and projected Newtonian potential of the lens,

$$\Psi(\vec{\theta}) = \frac{D_{ls}}{D_l D_s}\frac{2}{c^2}\int \Phi(D_l\vec{\theta}, r_3)\mathrm{d}r_3\,. \tag{4.16}$$

The lensing potential has the nice property that its gradient with respect to $\vec{\theta}$ is the deflection angle

$$\vec{\nabla}_\theta\Psi(\vec{\theta}) = \frac{D_{ls}}{D_s}\frac{2}{c^2}\int \vec{\nabla}_\perp\Phi(\vec{\xi}, r_3)\mathrm{d}r_3 \;= \vec{\alpha}(\vec{\theta}), \tag{4.17}$$

where the perpendicular gradient is now acting on the physical impact parameter having used the small angle approximation $\vec{\xi} \simeq D_l\vec{\theta}$. Assuming further that the changes of the Newtonian potential along the line of sight average out, which is true for instance, as long as the lensing object is only slowly varying and does not undergo a rapid collapse. More precisely, the time–scale on which light travels across the lensing object, has to be much smaller than the collapse time–scale of the light deflecting object. Then the two–dimensional Laplacian can be replaced by its three–dimensional analogue,

$$\Delta^{(2)}\Phi(\vec{r}) = \sum_{i=1}^{2}\frac{\partial^2\Phi(\vec{r})}{\partial\xi_i^2} \simeq \sum_{i=1}^{3}\frac{\partial^2\Phi(\vec{r})}{\partial r_i^2} = \Delta^{(3)}\Phi(\vec{r})\,. \tag{4.18}$$

Therefore, the Laplacian of the lensing potential acting on its angular coordinate $\vec{\theta}$ equals twice the surface mass density scaled with its critical value, i.e. the convergence κ,

$$\Delta_\theta^{(2)}\Psi(\vec{\theta}) = \frac{2}{c^2}\frac{D_l D_{ls}}{D_s}\int \Delta^{(3)}\Phi(\vec{\xi}, r_3)\mathrm{d}r_3 = 2\frac{4\pi G}{c^2}\frac{D_l D_{ls}}{D_s}\int \rho(\vec{\xi}, r_3)\mathrm{d}r_3 = 2\kappa(\vec{\theta})\,, \tag{4.19}$$

where Poisson's equation has been used in the second step. Since Ψ satisfies the two–dimensional Poisson's equation, its Green's function has to be considered, namely

$$\Delta^{(2)}G(\vec{\theta}, \vec{\theta}') = 2\pi\delta_D(\vec{\theta}, \vec{\theta}') \qquad \Longrightarrow \qquad G(\vec{\theta}, \vec{\theta}') = \ln|\vec{\theta} - \vec{\theta}'|\,. \tag{4.20}$$

Therefore the lensing potential $\Psi(\vec{\theta})$ is given by the convolution integral of the source function $\kappa(\vec{\theta})$ and the Green's function in two dimensions,

$$\Psi(\vec{\theta}) = \frac{1}{\pi}\int \kappa(\vec{\theta}')\ln|\vec{\theta} - \vec{\theta}'|\mathrm{d}^2\theta'\,. \tag{4.21}$$

4.1.4 Local Lens Properties

Liouville's theorem and the conservation of the physical number density of photons during the process of gravitational light bending imply that lensing conserves surface brightness or specific intensity. Assuming that the angular scale on which the lens

properties change is much larger than the extent of the source, the lens equation can locally be linearized yielding

$$\vec{\beta} = \vec{\theta} - \vec{\alpha}(\vec{\theta}) \simeq \vec{\beta}_0 + \frac{\partial \vec{\beta}}{\partial \vec{\theta}} \left(\vec{\theta} - \vec{\theta}_0 \right). \tag{4.22}$$

The local lens properties of the lens mapping are described by its Jacobian matrix $\mathcal{A}$

$$\mathcal{A} \equiv \frac{\partial \vec{\beta}}{\partial \vec{\theta}} = \left(\delta_{ij} - \frac{\partial \alpha_i(\vec{\theta})}{\partial \theta_j} \right) = \left(\delta_{ij} - \frac{\partial^2 \Psi(\vec{\theta})}{\partial \theta_i \partial \theta_j} \right) \equiv \left(\delta_{ij} - \Psi_{,ij}\left(\vec{\theta}\right) \right) = \mathcal{M}^{-1}, \tag{4.23}$$

where an abbreviation for partial derivatives has been introduced and $\mathcal{A}$ is the inverse of the magnification tensor $\mathcal{M}$. This is justified, because a solid–angle element $\delta\beta^2$ of the source is mapped onto the solid–angle element $\delta\theta^2$ on the image, and thus the magnification due to the mapping is given by

$$\frac{\delta\theta^2}{\delta\beta^2} = \det \mathcal{M} = \frac{1}{\det \mathcal{A}}. \tag{4.24}$$

The trace of the Jacobian $\mathcal{A}$ describes the isotropic magnification of the source,

$$\mathrm{tr}(\mathcal{A}) = (1 - \Psi_{,11}) + (1 - \Psi_{,22}) = 2(1 - \kappa). \tag{4.25}$$

This also intuitively explains the meaning of the convergence κ, which is a measure for how much the lens focuses light rays isotropically. Subtracting the trace from $\mathcal{A}$ leads to an expression for anisotropic distortion (astigmatism) of the image,

$$\mathcal{A}_{ij} - \frac{1}{2}\delta_{ij}\,\mathrm{tr}(\mathcal{A}) = \delta_{ij} - \Psi_{,ij} - \delta_{ij}(1 - \kappa) = -\Psi_{,ij} + \kappa\delta_{ij} \equiv \Gamma, \tag{4.26}$$

where the *shear tensor* Γ has been defined in the last step. This distortion is due to the tidal gravitational field. Particularly, it decomposes in

$$\Gamma = \begin{pmatrix} \gamma_1 & \gamma_2 \\ \gamma_2 & -\gamma_1 \end{pmatrix} \tag{4.27}$$

and

$$\gamma_1 = \frac{1}{2}(\Psi_{,11} - \Psi_{,22}) \equiv \gamma(\vec{\theta}) \cos\left(2\phi(\vec{\theta})\right) \tag{4.28}$$

$$\gamma_2 = \Psi_{,12} = \Psi_{,21} \equiv \gamma(\vec{\theta}) \sin\left(2\phi(\vec{\theta})\right). \tag{4.29}$$

Here $\gamma = \sqrt{\gamma_1^2 + \gamma_2^2}$ describes the magnitude of the shear and ϕ its orientation, whereas the factor 2 shows that γ is not a vector, but a 2×2–tensor.

4.2 Weak Cosmological Lensing

In contrast to "strong lensing", which requires the surface mass density $\Sigma(\vec{\theta})$ somewhere within the lens to be larger than the critical density Σ_{cr} and produces for

instance impressive giant luminous arcs, one talks about "weak lensing", if one can only determine statistical properties of the lensing system by averaging over the field of view. Conventionally, this method is applied to faint distant galaxy populations, whose shapes and sizes are distorted by the gravitational tidal field of the deflecting object. Due to intrinsic ellipticities of the individual galaxies, statistical techniques using apertures with angular size of the order $1'$ are needed in order to infer properties of the local gravitational field of the lens.

In contrast, we are interested in the overall weak lensing effect introduced by large scale structure in order to study lensing distortion effects on the CMB temperature fluctuations. Therefore the impact of weak density perturbations in an isotropic and homogeneous Friedmann–Lemaître universe on the propagation of light shall be studied. Throughout this work, it is assumed that the Newtonian potential of these inhomogeneities is only slowly varying compared to the light–crossing time and moreover small, i.e. $|\Phi| \ll c^2$. In realistic cosmological situations, this assumption is well satisfied, because typical velocities in galaxy clusters are of the order of $10^3\,\mathrm{km\,s^{-1}} \ll c$, and typical Newtonian potentials are of the order of $\Phi \lesssim 10^{-5}c^2$.

4.2.1 Light Propagation in a Friedmann–Lemaître Universe

First, the light propagation in an isotropic and homogeneous background universe will be considered. It can be shown (see e.g. Schneider, Ehlers & Falco (1992)) that the transverse comoving separation between neighboring rays in a thin light bundle in a Friedmann–Lemaître universe has the following form

$$\frac{\mathrm{d}^2\vec{x}}{\mathrm{d}w^2} + K\vec{x} = \vec{0}\,, \tag{4.30}$$

using the equation of geodesic deviation. Here the comoving separation vector $\vec{x}$ is related to the physical separation $\vec{\xi}$ by $\vec{x} = a^{-1}\vec{\xi}$, the comoving distance is denoted by w (2.27), and K denotes the curvature parameter introduced in section (2.1.1). The appropriate boundary conditions guarantee that the two past directed light rays start at the observer's position O and their initial directions are separated by $\vec{\theta}$, which reads

$$\vec{x}\big|_{w=0} = \vec{0} \qquad \text{and} \qquad \left.\frac{\mathrm{d}\vec{x}}{\mathrm{d}w}\right|_{w=0} = \vec{\theta}\,. \tag{4.31}$$

The solution of this differential equation obeying these boundary conditions is given by

$$\vec{x}(\vec{\theta}, w) = f_K(w)\vec{\theta}\,, \tag{4.32}$$

depending on the curvature (2.15). The function $f_K(w)$ is given by (2.2). In the case of spatial flatness the comoving separation $\vec{x}$ grows linearly with the comoving distance, whereas it oscillates either trigonometrically or grows hyperbolically, depending on whether K is positive or negative.

4.2.2 Light Deflection in Perturbed Friedmann–Lemaître Space–Time

Light Propagation in Perturbed Minkowski Space In addition to the assumption of weak gravitational fields, the density perturbations are assumed to be localized, i.e. the scales over which the potential Φ changes are much smaller than the curvature scale of the cosmological background model, $cH_0^{-1} \simeq 3000\,h^{-1}\,\mathrm{Mpc}$; thus these perturbations average out over the Hubble scale. As a result, there exists a local neighborhood to each inhomogeneity which is large enough to contain the perturbation completely and still small enough to be considered locally flat. In other words, space–time can be well approximated by the first order post–Minkowskian metric (4.1) which leads to a local equation for the deflection of light rays as shown in (4.5)

$$\frac{\mathrm{d}^2\vec{\xi}}{\mathrm{d}\lambda^2} = -\frac{2}{c^2}\vec{\nabla}_\perp \Phi(\vec{\xi},\lambda)\,. \tag{4.33}$$

In order to rewrite this in comoving distances, a relation between the affine curve parameter λ and the radial coordinate w has to be derived. Consider an observer with four–velocity u_O^μ satisfying $u_O^\mu u_{O\mu} = 1$. Because the physical wave vector k^μ of the photons depends on the light frequency, a past directed, dimensionless wave vector is defined by

$$\tilde{k}^\mu \equiv -\frac{c}{\omega_0}k^\mu\,, \tag{4.34}$$

which is clearly independent of the frequency of the photons ω_0 as measured by an observer. Moreover, the affine parameter λ is chosen to be zero at the observer's position O and obeys $u_O^\mu \tilde{k}_\mu = -1$ at O. Thus, the dimensionless wave vector can be written $\tilde{k}^\mu = \mathrm{d}x^\mu/\mathrm{d}\lambda$. The dispersion relation for the zeroth component in (4.34) reads $k^0 = \omega c^{-1} = \omega_0 a^{-1} c^{-1}$, thus we have $\tilde{k}^0 = -a^{-1}$. Combining these thoughts yields an expression for the proper distance of the photon path $\mathrm{d}\lambda = \mathrm{d}x^0/\tilde{k}^0 = -ac\,\mathrm{d}t$. This can be rewritten using the fact that photons travel on null geodesics which are chosen to be radial, $c\,\mathrm{d}t = -a\,\mathrm{d}w$, yielding

$$\mathrm{d}\lambda = a^2\,\mathrm{d}w\,. \tag{4.35}$$

Introducing the comoving separation of two neighboring photon rays, $\vec{x} = a^{-1}\vec{\xi}$, equation (4.33) reads

$$\frac{\mathrm{d}^2\vec{x}}{\mathrm{d}w^2} = -\frac{2}{c^2}\vec{\nabla}_\perp \Phi(\vec{x},w)\,, \tag{4.36}$$

where the gradient now acts on transverse comoving distances $\vec{x}$. This equation describes the deviation from a straight line due to weak gravitational density perturbations on locally flat Minkowskian space.

Light Propagation through Large Scale Structure Inhomogeneities The description of light propagation shall now be generalized to an expanding non–flat Friedmann–Lemaître universe with large scale mass fluctuations included. Taking a

straight line representing the reference light ray has no longer a unique meaning as in flat space. Therefore, an arbitrary fiducial light ray is chosen as a reference. In this case a modified differential equation describes the evolution of the comoving separation $\vec{x}$ of the perturbed light rays as a function of comoving distance from the observer w of initially closely separated light rays due to the difference in the potential gradients they pass, i.e. $\Delta(\vec{\nabla}_\perp \Phi)$. Let the past directed fiducial light ray start into the direction $\vec{\theta} = \vec{0}$ at the coordinate origin, and its companion into $\vec{\theta} \neq \vec{0}$. Combining the cosmological curvature term of equation (4.30) and the new local source term of the difference of the perpendicular potential gradients along the two light rays yields the propagation equation

$$\frac{\mathrm{d}^2\vec{x}}{\mathrm{d}w^2} + K\vec{x} = -\frac{2}{c^2}\Delta\left\{\vec{\nabla}_\perp \Phi\left[\vec{x}(\vec{\theta}, w), w\right]\right\} . \tag{4.37}$$

Strictly interpreting this notation, the difference on the right–hand side needs to be evaluated between the two light rays at their momentary separation $\vec{x}(\vec{\theta}, w)$ at the comoving distance w, respectively. For simplification, one takes the definitions of global properties of *unperturbed* Friedmann–Lemaître models, like comoving distance w or affine parameter λ in this context, which actually changes in the presence of density fluctuations. Thus, the solution of the boundary value problem (4.31) in this general case is a sum of the homogeneous solution (4.32) and its convolution with the inhomogeneous source term,

$$\vec{x}(\vec{\theta}, w) = f_K(w)\vec{\theta} - \frac{2}{c^2}\int_0^w \mathrm{d}w'\, f_K(w - w')\Delta\left\{\vec{\nabla}_\perp \Phi\left[\vec{x}(\vec{\theta}, w'), w'\right]\right\} , \tag{4.38}$$

where the integral needs to be evaluated along the true photon paths.

Born Approximation In addition to the approximations of slowly varying and weak gravitational fields, $|\Phi| \ll c^2$, and the assumption of well localized density perturbations within a homogeneous and isotropic background solution, a third approximation is used in order to further simplify this complex problem: It is assumed that the comoving separation vector between the two perturbed light rays $\vec{x}(\vec{\theta}, w')$ due to the gravitational field does not strongly deviate from the comoving separation of unperturbed rays, $f_K(w')\vec{\theta}$,

$$\frac{|\vec{x}(\vec{\theta}, w') - f_K(w')\vec{\theta}|}{|f_K(w')\vec{\theta}|} \ll 1 . \tag{4.39}$$

Thus, it is sufficient to evaluate the perpendicular gradient of the potential along unperturbed rays, i.e. we can replace $\vec{x}(\vec{\theta}, w')$ by $f_K(w')\vec{\theta}$ in the integrand. This is the so–called Born approximation of small angle scattering. Furthermore in this limit, one can replace the difference of the orthogonal gradients of the potentials, $\Delta(\vec{\nabla}_\perp \Phi)$, by the perpendicular gradient of the difference of the potentials, $\vec{\nabla}_\perp(\Delta\Phi)$. In the following, for convenience the potential Φ substitutes the difference $\Delta\Phi$, because the replacement procedure effectively results in a redefinition of the potential.

Effective Deflection Angle The deflection angle $\vec{\alpha}$ at comoving distance w is the difference between the separation vector of two light rays propagating through unperturbed space–time, $f_K(w)\vec{\theta}$ (4.32), and the comoving separation vector of the perturbed light rays, $\vec{x}(\vec{\theta}, w)$, divided by the angular diameter distance to w,

$$\vec{\alpha}(\vec{\theta}, w) = \frac{f_K(w)\vec{\theta} - \vec{x}(\vec{\theta}, w)}{f_K(w)} = \frac{2}{c^2}\int_0^w \mathrm{d}w' \, \frac{f_K(w-w')}{f_K(w)} \vec{\nabla}_\perp \Phi\left[f_K(w')\vec{\theta}, w'\right] . \quad (4.40)$$

The choice of the fiducial ray reflects an inherent gauge freedom, because *only* derivatives of the deflection angle produce measurable effects. Nevertheless, the deflection angle depends strongly on the choice of the fiducial ray.

4.2.3 Effective Convergence κ_{eff}

Definition and Derivation In analogy to the definition of the convergence in the thin lens approximation, $\kappa(\vec{\theta}) = \frac{1}{2}\vec{\nabla}_\theta \vec{\alpha}(\vec{\theta})$, an *effective convergence* can be defined for cosmological weak lensing,

$$\kappa_{\mathrm{eff}}(\vec{\theta}, w) \equiv \frac{1}{2}\vec{\nabla}_\theta \vec{\alpha}(\vec{\theta}, w) = \frac{1}{c^2}\int_0^w \mathrm{d}w' \, \frac{f_K(w-w')f_K(w')}{f_K(w)} \Delta_{\vec{x}}^{(2)} \Phi\left[f_K(w')\vec{\theta}, w'\right] . \quad (4.41)$$

This approach of projecting the suitably weighted Laplacian of the potential along the line–of–sight onto the source plane is called the *"effective" theory*. Here the two–dimensional Laplacian $\Delta_{\vec{x}}^{(2)}$ acts on the first argument of the potential. In order to replace this Laplacian, we have to consider Poisson's equation in perturbed Friedmann–Lemaître space–time,

$$\Delta_r(\bar{\Phi} + \Phi) = 4\pi G\rho \, , \quad (4.42)$$

where the Laplacian acts on the physical coordinates of both the potential of the smooth background $\bar{\Phi}$ and the potential of the density perturbations Φ. The total matter density is denoted by $\rho = (1+\delta)\bar{\rho}$. After subtracting the contribution of the smooth background, $\Delta_r\bar{\Phi} = 4\pi G\bar{\rho}$, and rewriting the Laplacian in comoving coordinates, $\Delta_x = a^2\Delta_r$, Poisson's equation describing the density perturbation reads

$$\Delta_x \Phi(\vec{x}) = 4\pi G a^2 \bar{\rho}\delta = \frac{3H_0^2}{2a}\Omega_m \delta \, . \quad (4.43)$$

For the last step, a matter–dominated equation of state was assumed, $\bar{\rho}(a) = \rho_0 a^{-3}$. Using the same arguments like in the thin lens approximation (4.18), the two–dimensional Laplacian can be replaced by a three–dimensional one, such that equation (4.41) can be rewritten as

$$\kappa_{\mathrm{eff}}(\vec{\theta}, w) = \frac{3H_0^2\Omega_m}{2c^2}\int_0^w \mathrm{d}w' \, \frac{f_K(w-w')f_K(w')}{f_K(w)} \frac{\delta[f_K(w')\vec{\theta}, w']}{a(w')} \, . \quad (4.44)$$

This expression is interpreted as the effective convergence for a fixed source redshift $z(w)$ like for instance the last–scattering surface. In this limit, it is given by the

integral along an unperturbed light ray over the appropriately scaled density contrast weighted by its lensing efficiency function. Using the definitions of both the proper distance (2.26), $\mathrm{d}D_{\mathrm{prop}} \equiv -c\,\mathrm{d}t = a\,\mathrm{d}w$, and the angular diameter distance D_{ang} (2.30) and recalling the expression for the critical density (2.12), the preceding equation (4.44) can be written as

$$\kappa_{\mathrm{eff}}(\vec{\theta}, z_s) = \frac{4\pi G}{c^2} \int_0^{z_s} \mathrm{d}z\, \frac{D_l D_{ls}}{D_s} \frac{\mathrm{d}D_{\mathrm{prop}}}{\mathrm{d}z} \left(\rho(\vec{\theta}, z) - \bar{\rho}\right) . \tag{4.45}$$

Here the distances D_l, D_{ls} and D_s are angular diameter distances.

Power Spectrum of the Effective Convergence For this work, we are especially interested in statistical lensing properties, namely the two–dimensional power spectrum of the effective convergence P_κ which is related to the three–dimensional power spectrum of the density contrast P_δ by Limber's equation (3.14). The power spectrum of the effective convergence with a source at redshift $z = z_s(w_s)$ can easily be obtained by identifying the function $g(\vec{\theta})$ defined in (3.7) with κ_{eff} and taking

$$q_1(w) = q_2(w) = \frac{3H_0^2\Omega_m}{2c^2} \frac{f_K(w_s - w) f_K(w)}{f_K(w_s) a(w)} . \tag{4.46}$$

Thus, we have established the power spectrum for the effective convergence

$$P_\kappa(\ell) = \frac{9H_0^4\Omega_m^2}{4c^4} \int_0^{w_s} \mathrm{d}w \left(\frac{f_K(w_s - w)}{f_K(w_s) a(w)}\right)^2 P_\delta\left(\frac{\ell}{f_K(w)}, w\right) . \tag{4.47}$$

The relation between the statistics of the effective convergence κ_{eff} and the *effective shear* γ_{eff} can be shown in Fourier space. In the following, the indices indicating effective lensing quantities are dropped for convenience. In Fourier space, the components of the Jacobian are

$$\hat{\kappa} = -\frac{1}{2}\left(\ell_1^2 + \ell_2^2\right) \hat{\Psi} \tag{4.48}$$

$$\hat{\gamma_1} = -\frac{1}{2}\left(\ell_1^2 - \ell_2^2\right) \hat{\Psi} \tag{4.49}$$

$$\hat{\gamma_2} = -\ell_1 \ell_2 \hat{\Psi} . \tag{4.50}$$

Thus, the square of the shear γ equals the square of the convergence κ, $\hat{\gamma}^2 \equiv \hat{\gamma_1}^2 + \hat{\gamma_2}^2 = \frac{1}{4}(\ell_1^2 + \ell_2^2)^2 \hat{\Psi}^2 = \hat{\kappa}^2$, which yields equality for their power spectra in the limit of weak cosmological lensing

$$\left\langle \hat{\kappa}_{\mathrm{eff}}(\ell) \hat{\kappa}^*_{\mathrm{eff}}(\ell') \right\rangle = \left\langle \hat{\gamma}_{\mathrm{eff}}(\ell) \hat{\gamma}^*_{\mathrm{eff}}(\ell') \right\rangle \quad \Longrightarrow \quad P_\kappa(\ell) = P_\gamma(\ell) . \tag{4.51}$$

Assuming Gaussian density fluctuations, this shows that the overall statistical information is contained in each of the two power spectra.

A similar relation can also be obtained for the power spectra of the deflection angle and the convergence, respectively. The effective convergence was defined to be half the

divergence of the deflection angle. Inverting this equation and rewriting it in Fourier space yields

$$\hat{\vec{\alpha}}(\vec{\ell}) = \frac{2\mathrm{i}\hat{\kappa}_{\mathrm{eff}}(\ell)}{|\vec{\ell}|^2}\vec{\ell}. \tag{4.52}$$

Hence, the deflection angle power spectrum reads

$$P_{\vec{\alpha}}(\ell) = \frac{4}{\ell^2}P_\kappa(\ell)\,. \tag{4.53}$$

4.2.4 Multiple Lens Plane Theory

So far, the presented formalism of weak cosmological lensing relies on continuous integrals of smooth perturbed density distributions. In order to perform gravitational lensing simulations in realistic model universes, this continuous approach needs to be modified using a discretization method. A straightforward way to do so is by introducing multiple lens planes perpendicular to the line–of–sight where the spacing of two successive planes is much larger than a typical distance between two potential wells in the lens planes. The intermediate mass distribution is projected onto these lenses such that light rays can propagate freely through the space in between two lenses, and only get deflected at the lens planes due to the projected Newtonian potentials, respectively. For convenience, one considers past directed light rays starting at the observer's point at a_0 into the direction of the source plane at a_s. Given N lens planes at angular diameter distances $D_i(a_i)$ to the observer, $i = 1, \ldots, N$, ordered such that for $i < j,\ a_i > a_j > a_s$, i.e. the lens planes are numbered with increasing distance from the observer.

The Lens Equation The light ray starting into direction $\vec{\theta}_1$ intersects the first lens plane at $\vec{\xi}_1$, experiences a deflection of $\vec{\hat{\alpha}}_1(\vec{\xi}_1)$ and propagates into the new direction towards the next lens plane etc. Using the theorem of intersecting lines, the position $\vec{\eta}$ of the light ray on the source plane reads

$$\vec{\eta} = \frac{D_s}{D_1}\vec{\xi}_1 - \sum_{i=1}^{N} D_{is}\vec{\hat{\alpha}}_i(\vec{\xi}_i)\,. \tag{4.54}$$

The impact vectors $\vec{\xi}_j$ on the j–th lens plane are obtained recursively from

$$\vec{\xi}_j = \frac{D_j}{D_1}\vec{\xi}_1 - \sum_{i=1}^{j-1} D_{ij}\vec{\hat{\alpha}}_i(\vec{\xi}_i)\,, \tag{4.55}$$

where $D_{ij} = D_{\mathrm{ang}}(a_j, a_i)$ is the angular diameter distance from the i–th to the j–th lens plane. A dimensionless form of this *multiple lens plane equation* can be obtained by introducing the reduced deflection angles $\vec{\alpha}_i = \frac{D_{is}}{D_s}\vec{\hat{\alpha}}_i$ and using the small angle approximation $\vec{\theta}_i = \vec{\xi}_i/D_i$, leading to

$$\vec{\theta}_j = \vec{\theta}_1 - \sum_{i=1}^{j-1} \frac{D_{ij}D_s}{D_j D_{is}}\vec{\alpha}_i(\vec{\theta}_i)\,. \tag{4.56}$$

It is often useful to consider comoving distances because of their additive property. To do so, the reduced deflection angle $\vec{\alpha}_i$ can be rewritten into a perpendicular gradient acting on the comoving orthogonal distances $\vec{x}$ of the lensing potential Ψ,

$$\vec{\alpha}_i = \vec{\nabla}_\theta \Psi_i(\vec{\theta}) = D_i \vec{\nabla}_\xi \Psi_i \left(\frac{\vec{\xi}_i}{D_i} \right) = \frac{D_i}{a_i} \vec{\nabla}_x \Psi_i \left(\frac{a_i \vec{\xi}_i}{D_i} \right) = f_K(w_i) \vec{\nabla}_x \Psi_i \left(\frac{\vec{\xi}_i}{f_K(w_i)} \right) . \tag{4.57}$$

For the final step, the definition of the angular diameter distances, $D_{\text{ang}}(a_i, a_0) = a_i f_K(w_i)$ was used. Recalling the definition for the lensing potential (4.16) yields finally

$$\begin{aligned} \vec{\theta}_j &= \vec{\theta}_1 - \sum_{i=1}^{j-1} \frac{f_K(w_j - w_i)}{f_K(w_j) a_i} \vec{\nabla}_x \left[\frac{2}{c^2} \int_{w_i}^{w_{i+1}} \Phi_i(\vec{x}, w) \, \mathrm{d}w \right] \\ &= \vec{\theta}_1 - \sum_{i=1}^{j-1} \frac{f_K(w_j - w_i)}{f_K(w_j) a_i} \vec{\nabla}_x \tilde{\Psi}_i(\vec{x}) . \end{aligned} \tag{4.58}$$

In the last step, the *unscaled lensing potential* $\tilde{\Psi}_i$ has been defined to be the projection of the Newtonian potential along the line of sight to the next lens plane.

The Jacobian Matrix Next, the Jacobian matrix $\mathcal{A}$ of the lens mapping shall be considered. The Jacobian matrices $\mathcal{A}_i$ on individual lens planes and the tidal matrices $\mathcal{U}_i$ are defined by

$$\mathcal{A}_i \equiv \frac{\partial \vec{\theta}_i}{\partial \vec{\theta}_1} \qquad \text{and} \qquad \mathcal{U}_i \equiv \frac{\partial \vec{\alpha}_i}{\partial \vec{\theta}_i} . \tag{4.59}$$

We find from equation (4.56) a recursion relation for the Jacobian

$$\mathcal{A}_j \equiv \frac{\partial \vec{\theta}_j}{\partial \vec{\theta}_1} = \mathcal{I} - \sum_{i=1}^{j-1} \frac{D_{ij} D_s}{D_j D_{is}} \mathcal{U}_i \mathcal{A}_i \qquad \text{and} \qquad \mathcal{A}_1 = \mathcal{I} . \tag{4.60}$$

Rewritten in comoving angular diameter distances, this equation reads

$$\begin{aligned} \mathcal{A}_j &\equiv \frac{\partial \vec{\theta}_j}{\partial \vec{\theta}_1} = \mathcal{I} - \sum_{i=1}^{j-1} \frac{f_K(w_i) f_K(w_j - w_i)}{f_K(w_j) a_i} \tilde{\mathcal{U}}_i \mathcal{A}_i , \\ \text{where} \qquad \tilde{\mathcal{U}}_i &\equiv \begin{pmatrix} \tilde{\Psi}_{i,11}(\vec{x}) & \tilde{\Psi}_{i,12}(\vec{x}) \\ \tilde{\Psi}_{i,21}(\vec{x}) & \tilde{\Psi}_{i,22}(\vec{x}) \end{pmatrix} . \end{aligned} \tag{4.61}$$

Comparing this equation to the propagation equation for the deflection angle (4.58), we notice a different distance combination within the sum over the lens planes which can possibly affect the numerical propagation of the photons. However, this influence will be studied later on.

4.3 Weak Lensing of the CMB Photons

The presented machinery of weak cosmological lensing shall now be applied to study the influence of lensing effects on the CMB temperature fluctuations at the last–scattering surface, which can be treated as a source plane at $z \approx 1100$. A past directed light ray starting into direction $\vec{\theta}$ with respect to an arbitrarily chosen optical axis experiences a certain number of deflections due to inhomogeneities resulting in a net deflection angle $\kappa_{\rm eff}(\vec{\theta})$ and intercepts the last–scattering surface at the 'true' position

$$\vec{\beta} = \vec{\theta} - \vec{\alpha}(\vec{\theta})\,. \tag{4.62}$$

In other words, the intrinsic temperature of the CMB at the original position $\vec{\beta}$ on the surface of last scattering is mapped to the angular position $\vec{\theta}$ in the sky where we will observe it, or

$$T_{\rm obs}(\vec{\theta}) = T_{\rm int}(\vec{\beta}) = T_{\rm int}[\vec{\theta} - \vec{\alpha}(\vec{\theta})]\,. \tag{4.63}$$

The statistical quantities are also changed by lensing, e.g. the temperature auto–correlation function (2.38) reads in the presence of lensing

$$\xi_T'(\phi) = \left\langle \tau[\vec{\theta} - \vec{\alpha}(\vec{\theta})]\tau[(\vec{\theta}+\vec{\phi}) - \vec{\alpha}(\vec{\theta}+\vec{\phi})] \right\rangle_{\{\vec{\theta}\}}\,. \tag{4.64}$$

Expanding the relative temperature fluctuations $\tau(\vec{\theta})$ into Fourier modes,

$$\tau(\vec{\theta}) = \int \frac{{\rm d}^2\ell}{(2\pi)^2} \hat{\tau}(\vec{\ell}) e^{-{\rm i}\vec{\ell}\cdot\vec{\theta}}\,, \tag{4.65}$$

is justified because weak cosmological lensing *only* influences small angular scales such that a flat–sky approximation is locally valid. Inserting this expression into (4.64) introduces the CMB temperature power spectrum $P_T(\ell)$ which is defined in this limit by

$$\left\langle \hat{\tau}(\vec{\ell})\hat{\tau}^*(\vec{\ell}') \right\rangle \equiv (2\pi)^2 \delta_D^{(2)}(\vec{\ell} - \vec{\ell}') P_T(\ell)\,. \tag{4.66}$$

Assuming further the Gaussian nature of the density fluctuations, it can be shown (Bartelmann & Schneider 2001) that the temperature auto–correlation function modified by gravitational lensing can be written as

$$\xi_T'(\phi) = \int_0^\infty \frac{\ell\,{\rm d}\ell}{2\pi} P_T(\ell) e^{-\frac{1}{2}\ell^2\sigma^2(\phi)} J_0(\ell\phi)\,. \tag{4.67}$$

Here $J_0(x)$ is the zeroth–order Bessel function of the first kind and $\sigma^2(\phi)$ the dispersion of the deflection angle,

$$\sigma^2(\phi) \equiv \frac{1}{2}\left\langle \left[\vec{\alpha}(\vec{\theta}) - \vec{\alpha}(\vec{\theta}+\vec{\phi})\right]^2 \right\rangle\,. \tag{4.68}$$

Thus, gravitational lensing of the CMB temperature fluctuations effectively results in smoothing on an angular scale ϕ by the amount $\sigma(\phi)$. Assuming the following

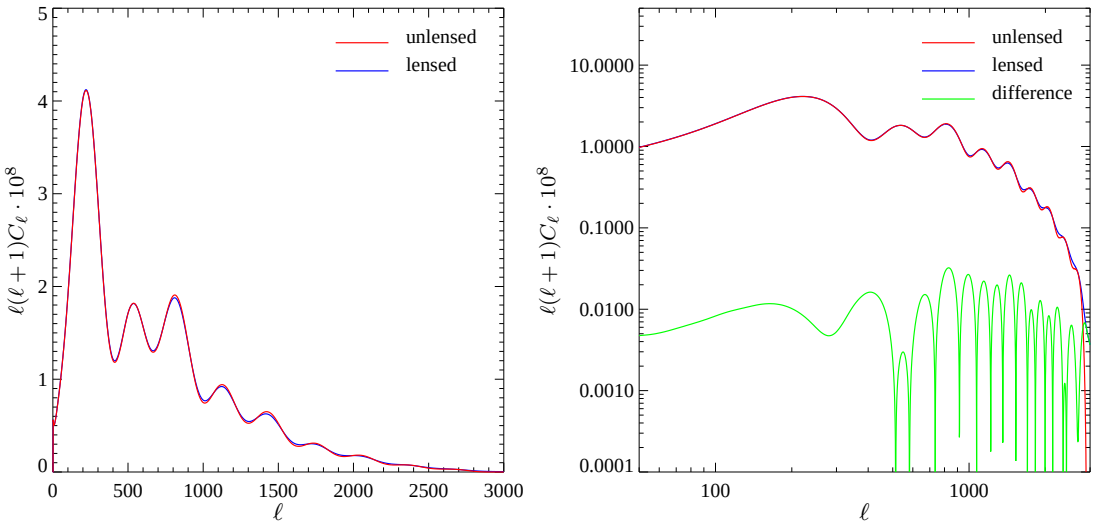

Figure 4.2: The CMB angular power spectrum $\ell(\ell+1)C_\ell$ is shown as a function of ℓ in both linear and double logarithmic representation. The red line depicts the intrinsic, the blue line the lensed power spectrum for the ΛCDM cosmology. The green line on the right–hand side shows the difference of these two power spectra. The graphs are produced with the `CMBfast` code, see Zaldarriaga & Seljak (1998).

---

expression for the dispersion, $\sigma(\phi) = \varepsilon\phi$ with $\varepsilon \ll 1$ being either a constant or a function varying slowly with ϕ, equation (4.67) can be rewritten in terms of the power spectrum, yielding

$$P'_T(\ell) = \int_0^\infty \frac{\mathrm{d}\ell'}{\sqrt{2\pi}\varepsilon\ell'} P_T(\ell') \exp\left[-\frac{(\ell-\ell')^2}{2\varepsilon^2\ell'^2}\right] . \tag{4.69}$$

In Fourier space, the smoothing leads to a convolution with a Gaussian which can be seen in figure (4.2).

Part II

Simulations of Cosmological Weak Lensing of the Cosmic Microwave Background

5 Lensing Statistics using Cosmological Simulations

After the presentation of the theoretical background, different numerical simulations for studying weak cosmological lensing are described. The purpose of this chapter is to give an introduction to large N–body simulations of evolving density distributions, which are used in this work as an underlying matter background acting as a gravitational lens. The first section describes the structure of such N–body simulations and some important details involved, and the following section presents signal–to–noise estimates of the convergence and investigates the lensing efficiency function. Finally, surface density power spectra on different lens planes spanning a large range of redshifts are studied, and Limber's equation yields the power spectrum of the effective convergence. Thus, the whole chapter studies the potentiality of N–body simulations for second–order lensing statistics.

5.1 N–body Simulations

5.1.1 Structure of the Simulations

The N–body simulations with parallel codes were carried out by the Virgo Consortium, which are essentially larger realizations of cosmological models previously simulated by Jenkins et al. (1998). The new simulation was carried out by Yoshida et al. (2001) in order to study non–Gaussian features in the CMB fluctuations introduced by the thermal and kinetic Sunyaev–Zel'dovich effect in the direction of galaxy clusters.

It uses 512^3 particles in a cosmological box of side length $480\,h^{-1}\,\mathrm{Mpc}$. The cosmological model underlying the simulation is flat with matter density $\Omega_m = 0.3$, cosmological constant $\Omega_\Lambda = 0.7$ and present expansion rate $H_0 = 70\,\mathrm{km\,s^{-1}\,Mpc}$. The simulation is normalized to yield the observed abundance of rich clusters at $z = 0$ (White, Efstathiou & Frenk 1993a) and is also consistent with the level of fluctuations measured by COBE setting $\sigma_8 = 0.9$.

The numerical simulation uses the adaptive particle–particle/particle–mesh (AP^3M) technique in large boxes for studying the formation of structure in the Universe by evolving trajectories of a large number of particles forward in time. For simulating the light cone of the photons traversing the evolving matter density, a snapshot of the three–dimensional density distribution in the boxes at progressing redshifts was taken. For numerical reasons the density distribution was discretized into particles with mass $m_{\mathrm{part}} = 6.82 \cdot 10^{10}\,h^{-1} M_\odot$ in the cosmological N–body simulation representing each

a large number of less massive cold dark matter (CDM) particles only. One has to keep in mind that the dissipational baryonic matter component is neglected in these simulations, i.e. effects of high density regions are ignored, where the gas will be heated by shocks and afterwards cool radiatively. This could be one mechanism of star formation if cooling is efficient enough, and would cause an energy input into the surrounding gas by subsequent supernovae and stellar winds. Returning to the CDM simulations, the calculation of the gravitational force uses separate methods on different scales in order to save computational time:

For computing the *long–range gravitational force* on one particle exerted by the others, the discrete mass distribution is smoothed on a three–dimensional mesh which is then fast–Fourier transformed. In Fourier space, the Newtonian potential can easily be obtained because Poisson's equation is algebraic. After an inverse fast–Fourier transform, the forces are interpolated from the lattice back to the particle positions. Using this method, one only needs to evaluate $N \log N$ terms per time step, putting up with the low resolution of the mesh, however. In weakly clustered regions, *short–range forces* are therefore computed using the discrete Newtonian law of gravity between all pairs of particles, which is a process of complexity N^2. Finally, within clustered regions, containing approximately 10^5 particles, higher resolution meshes, so–called *refinements*, are recursively placed on top of the old mesh. Indeed, this speeds up the calculations, although leaving the problem of solving fast–Fourier transforms with non–periodic boundary conditions.

5.1.2 Limitations of the Simulations

Assuming weak interactions only, CDM particles are described by the collisionless Boltzmann equation and Poisson's equation. By taking the discrete limit of interacting particles, the resulting potential is numerically ill behaved at small scales. For these two reasons, the point-like representation of the particles is smoothed with a normalized, spherically symmetric spline kernel of the mass distribution whose broadening is determined by the softening length parameter h,

$$\rho_i(\vec{r}) = m_i \delta_D^3(\vec{r} - \vec{r}_i) \qquad \longrightarrow \qquad \rho_i(\vec{r}) = m_i W(\vec{r} - \vec{r}_i, h)\,. \tag{5.1}$$

This technique corresponds in principle to the Plummer form of *force softening* which explicitly modifies the Newtonian potential of this particle by introducing the softening length ε,

$$\tilde{\vec{\Phi}}_i(\vec{r}) = -G \frac{m_i}{\sqrt{|\vec{r} - \vec{r}_i|^2 + \varepsilon^2}}\,. \tag{5.2}$$

This modification has the consequence of matching the real force law of the weakly interacting particles asymptotically at large scales and of preventing unwanted two–body relaxation in numerical experiments. Unfortunately, one loses resolution on scales of the order and smaller than the softening length, which is typically taken to be

$$\varepsilon \gtrsim f\bar{d} \equiv f \frac{L}{\sqrt[3]{N}} \qquad \text{with} \qquad f \sim 0.03 \ldots 0.1\,, \tag{5.3}$$

where $\bar{d}$ denotes the mean particle separation. The already mentioned finite box size of the simulations limits the statistical reliability on scales large compared to the side length $L_{\rm box}$ of the box by introducing larger statistical fluctuations because of the limited number of long–wavelength modes on these scales.

5.1.3 Initial Conditions

Initial conditions were fixed by perturbing an initially uniform state described by a "glass"–like distribution of particles with the property that the net force of all other particles exerted upon an arbitrarily chosen particle is zero[1]. The Gaussian random field is set up by perturbing the positions of the particles and assigning them velocities according to growing mode solutions in linear theory. The simulations started at $z = 30$ using the approximation to the linear power spectrum given by Bond & Efstathiou (1984), and the transfer function was computed using the code `CMBfast` by Seljak & Zaldarriaga (1996).

5.2 Different Estimates for Lensing Simulations

5.2.1 Signal–to–Noise Estimates of the Convergence

Before taking a particular set of N–body simulations, its potentiality for lensing studies has to be analyzed by estimating signal–to–noise ratios. Thus, one has to compare inherent Poisson noise of the numerical simulations to the expected *rms* of the convergence in circular apertures of the desired resolution.

Convergence in Apertures For being able to distinguish statistically between lensing events due to Poisson noise and deflection due to real gravitational inhomogeneities, the expected *rms* of the convergence should clearly be measured with sufficient significance such that it exceeds the Poisson *rms* on the desired angular resolution scale θ. The averaged effective convergence within a circular aperture of radius θ is given by

$$\kappa_{\rm av}(\theta) = \int_0^\theta \frac{{\rm d}^2\phi}{\pi\theta^2}\bar{\kappa}_{\rm eff}(\vec{\phi})\,, \tag{5.4}$$

and its variance is

$$\langle\kappa_{\rm av}^2\rangle(\theta) = \int_0^\theta \frac{{\rm d}^2\phi}{\pi\theta^2}\int_0^\theta \frac{{\rm d}^2\phi'}{\pi\theta^2}\left\langle\bar{\kappa}_{\rm eff}(\vec{\phi})\bar{\kappa}_{\rm eff}(\vec{\phi'})\right\rangle\,. \tag{5.5}$$

The remaining average is the effective–convergence autocorrelation function $\xi_\kappa(|\vec{\phi}-\vec{\phi}|)$ which can be written terms of the power spectrum using equation (3.6),

$$\xi_\kappa(|\vec{\phi}-\vec{\phi}|) = \left\langle\bar{\kappa}_{\rm eff}(\vec{\phi})\bar{\kappa}_{\rm eff}(\vec{\phi'})\right\rangle = \int\limits_{\mathbb{R}^2}\frac{{\rm d}^2\ell}{(2\pi)^2}P_\kappa(\ell)e^{{\rm i}\vec{\ell}\cdot(\vec{\phi}-\vec{\phi})}\,. \tag{5.6}$$

[1] This method, originally proposed by White, propagates a particle distribution backward in time until such an initial state is reached which shows "glass"–like properties.

Inserting this expression into (5.5) yields

$$\langle\kappa_{\rm av}^2\rangle(\theta) = \int\limits_{\mathbb{R}^2} \frac{{\rm d}^2\ell}{(2\pi)^2} P_\kappa(\ell) \int_0^\theta \frac{{\rm d}^2\phi}{\pi\theta^2} e^{{\rm i}\vec{\ell}\cdot\vec{\phi}} \int_0^\theta \frac{{\rm d}^2\phi'}{\pi\theta^2} e^{-{\rm i}\vec{\ell}\cdot\vec{\phi}'} \,. \tag{5.7}$$

Since the last two integrals separate, they can be performed independently inserting the integral representation of Bessel functions of the first kind (Abramowitz & Stegun (1984), eq. 9.1.18),

$$\begin{aligned} \int_0^\theta \frac{{\rm d}^2\phi}{\pi\theta^2} e^{{\rm i}\vec{\ell}\cdot\vec{\phi}} &= 2\pi \int_0^\theta \frac{\phi\,{\rm d}\phi}{\pi\theta^2} \int_0^{2\pi} \frac{{\rm d}\psi}{2\pi} [\cos(\ell\phi\cos\psi) + {\rm i}\,\sin(\ell\phi\cos\psi)] \\ &= 2\pi \int_0^\theta \frac{\phi\,{\rm d}\phi}{\pi\theta^2} J_0(\ell\phi) = 2\pi \frac{J_1(\ell\theta)}{\pi\ell\theta} \,. \end{aligned} \tag{5.8}$$

In the last step, the substitution $\ell\phi \to \phi$ and the recursion relation for the Bessel functions of the first kind has been used, $\frac{\rm d}{{\rm d}x}[x^m J_m(x)] = x^m J_{m-1}(x)$. Thus, the variance of the effective convergence within a circular aperture of radius θ can be written as

$$\langle\kappa_{\rm av}^2\rangle(\theta) = 2\pi \int_0^\infty \ell{\rm d}\ell\, P_\kappa(\ell) \left[\frac{J_1(\ell\theta)}{\pi\ell\theta}\right]^2 \,. \tag{5.9}$$

In the case of three particular source redshifts, the variance of the effective convergence is plotted as a function of aperture radius θ in figure 5.1.

Signal–to–Noise in Numerical Simulations For estimating the *rms* in numerical simulations, the discretized density distribution needs to be modeled in circular apertures of angular size θ. Thus, the averaged convergence $\kappa_{\rm av}$ within a circular aperture reads in the discrete limit

$$\kappa_{\rm av} = \int {\rm d}a \left|\frac{{\rm d}V_{\rm prop}}{{\rm d}a}\right| \frac{\rho(a)}{m_{\rm part}} D_{\rm eff}(a) \quad \longrightarrow \quad \kappa_{\rm av} \approx \sum_i \Delta V_i \frac{\rho_i}{m_{\rm part}} D_i = \sum_i N_i D_i \,, \tag{5.10}$$

where $V_{\rm prop}$ is the proper volume element, ρ denotes the mass density of particles with mass $m_{\rm part}$ in the simulations, and $D_{\rm eff}$ is a dimensionless function quantifying lensing efficiency. The corresponding quantities in the discrete case of finite size volume elements are labeled with an index i and N_i is the number of discrete particles within such a volume element. The variance of the averaged convergence can be written as

$$\begin{aligned} {\rm var}(\kappa_{\rm av}) &= \left\langle (\kappa_{\rm av} - \langle\kappa_{\rm av}\rangle)^2 \right\rangle = \left\langle \left[\sum_i (N_i D_i - \bar{N} D_i)\right]^2 \right\rangle \\ &= \sum_{ij} D_i D_j \langle (N_i - \bar{N})(N_j - \bar{N}) \rangle \,. \end{aligned} \tag{5.11}$$

Assuming statistical independence between the different slices and a Poisson distribution of the simulation particles, then the average in equation (5.11) can be replaced

by $\delta_{ij} N_i$, yielding

$$\begin{aligned} \mathrm{var}(\kappa_{\mathrm{av}}) &= \sum_{ij} D_i D_j \delta_{ij} N_i = \sum_i D_i^2 N_i \\ &\approx \int \mathrm{d}a \left| \frac{\mathrm{d}V_{\mathrm{prop}}}{\mathrm{d}a} \right| \frac{\rho(a)}{m_{\mathrm{part}}} D_{\mathrm{eff}}^2(a) \,. \end{aligned} \tag{5.12}$$

In the last step, the continuous approximation of the sum was used. The number of particles within an infinitesimal slice of the light cone is given by

$$\delta \bar{N}_{\mathrm{part}} = \frac{\rho}{m_{\mathrm{part}}} \delta V = \frac{\rho_{\mathrm{cr}}}{m_{\mathrm{part}}} \frac{\Omega_m}{a^3} \underbrace{(aw)^2 \delta\tilde{\omega} \left| \frac{\mathrm{d}(ct)}{\mathrm{d}a} \right| \mathrm{d}a}_{\delta V} \,, \tag{5.13}$$

assuming a matter dominated equation of state. In this notation, $\delta\tilde{\omega}$ denotes the solid angle element of the aperture and w is the comoving distance from the observer to the considered volume element defined by equation (2.27). The Jacobian in equation (5.13) can be rewritten as

$$\left| \frac{\mathrm{d}(ct)}{\mathrm{d}a} \right| \mathrm{d}a = \frac{c\,\mathrm{d}a}{\dot{a}} = \frac{c\,\mathrm{d}a}{aH(a)} \,. \tag{5.14}$$

Combining the last three equations yields following expression for the variance of the averaged convergence within the aperture,

$$\mathrm{var}(\kappa_{\mathrm{av}}) = \frac{\rho_{\mathrm{cr}} \Omega_m}{m_{\mathrm{part}}} \delta\tilde{\omega} \frac{c}{H_0} \int_0^{a(z_s)} \frac{D_{\mathrm{eff}}^2(a, a_s)\, w^2(a)\, \mathrm{d}a}{\sqrt{\Omega_m a + (1 - \Omega_m - \Omega_\Lambda) a^2 + \Omega_\Lambda a^4}} \tag{5.15}$$

The following values are used for the parameters,

$$\begin{aligned} \Omega_m &\approx 0.3 \,, \\ \Omega_\Lambda &\approx 0.7 \,, \\ \rho_{\mathrm{cr}} &\approx 2.8 \cdot 10^{11}\, h^2 M_\odot\, \mathrm{Mpc}^{-3} \,, \\ m_{\mathrm{part}} &\approx 6.86 \cdot 10^{10}\, h^{-1}\, M_\odot \,, \\ \delta\tilde{\omega} &\approx \frac{\pi}{4} \left(\frac{5' \cdot 2\pi}{60' \cdot 360} \right)^2 \,, \\ cH_0^{-1} &\approx 3 \cdot 10^3\, h^{-1}\, \mathrm{Mpc} \,. \end{aligned}$$

Depending on the source redshift z_s of the lensing efficiency function, the inverse signal–to–noise ratio within a circular aperture of radius θ due to Poisson fluctuations can be defined, using equations (5.15) and (5.10),

$$\frac{N}{S}(\theta, z_s) \equiv \frac{\sqrt{\mathrm{var}(\kappa_{\mathrm{av}})}}{\kappa_{\mathrm{av}}} \propto \frac{1}{\theta} \tag{5.16}$$

These Poisson fluctuations are always present, even in the case of uniform discretized density distributions.

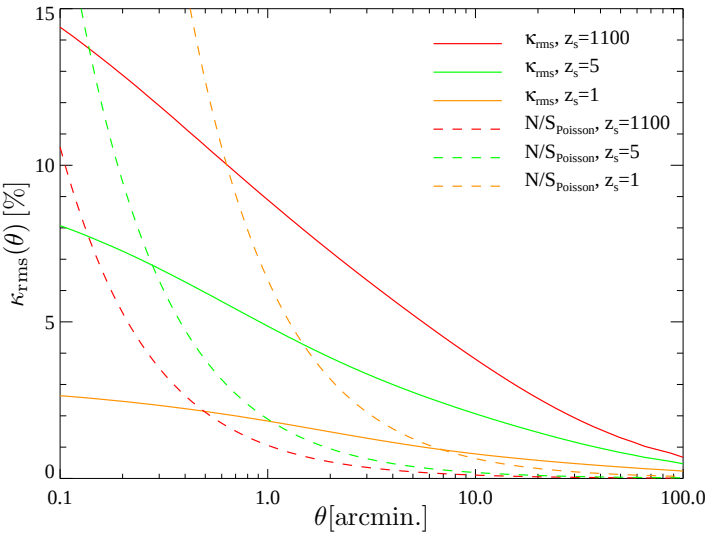

Figure 5.1: Signal–to–noise estimate of the effective convergence within a circular aperture of radius θ. The *rms* convergence $\kappa_{\rm rms}(\theta)$ is plotted as a function of θ at three different source redshifts $z_s = \{1, 5, 1100\}$ assuming a flat ΛCDM cosmological model and a non–linear density evolution (solid lines). They are compared to the inverse signal–to–noise ratios (dashed lines) within a circular aperture of radius θ due to Poisson noise.

Figure 5.1 shows a signal–to–noise estimate of the effective convergence within a circular aperture of radius θ. The *rms* convergence $\kappa_{\rm rms}(\theta) = \langle\kappa^2_{\rm av}\rangle^{1/2}(\theta)$ (defined in equation (5.9)) at three different source redshifts $z_s = \{1, 5, 1100\}$ is compared to the inverse signal–to–noise ratios within a circular aperture of radius θ due to Poisson noise (cf. equation (5.16)). For low source redshift $z_s = 1$, $\kappa_{\rm rms}$ becomes comparable to the Poisson noise at scales of ~ 5 arc minutes. The expected resolution limit due to Poisson noise shifts to smaller angular scales for increasing source redshifts such that we expect a resolution down to ~ 0.1 arc minutes for the source redshift of the surface of last scattering, $z_s = 1100$.

5.2.2 Lensing Efficiency Function

For studying lensing effects on the CMB anisotropies, it is important to produce fields whose angular size is as large as possible in order to improve statistics. This implies that the field of view has to subtend a large solid angle which, however, is limited by the side length of the box in which the simulations were performed. There are two effects allowing us to reduce the number of lens planes in the high redshift universe which need to be considered in order to obtain an acceptable size of the lensing field but nevertheless reproduce all necessary effects of lensing. This can be seen by taking

into account the effective convergence as presented in equation (4.45),

$$\kappa_{\text{eff}} = \frac{4\pi G}{c^2} \int_0^{z_s} \mathrm{d}z \, \frac{D_l D_{ls}}{D_s} \frac{\mathrm{d}D_{\text{prop}}}{\mathrm{d}z} \, (\rho - \bar{\rho}) \; . \tag{5.17}$$

Considering the distance combination $D_l D_{ls}/D_s$, it is clear that it has the same functional behavior as the graph on the right–hand side of figure 5.2, namely it approaches zero towards the observer and the source and peaks in between asymmetrically shifted to lower redshifts due to the definition of the angular diameter distance. This combination acts as a lensing efficiency function D_{eff} suppressing structures at high and low redshifts which are not contributing to lensing.

The other effect is the growth of structure starting from the weakly perturbed but otherwise smooth background and yielding high overdensities in the present Universe through gravitational instability. This effect is mathematically described by the growth function $g(a)$ which was defined in equation (2.46). Its functional form, changing with the scale factor, is shown in the left–hand side of figure (5.2). The growth rate is constant for the Einstein–de Sitter model ($\Omega_m = 1, \Omega_\Lambda = 0$), while it is higher in the earlier Universe ($a \ll 1$) and lower for $a \lesssim 1$ for the preferred ΛCDM model. As a consequence, structure forms earlier in low–Ω_m than in high–Ω_m models.

Combining these two effects yields the function effectively influencing lensing, depicted on the right–hand side of figure (5.2).

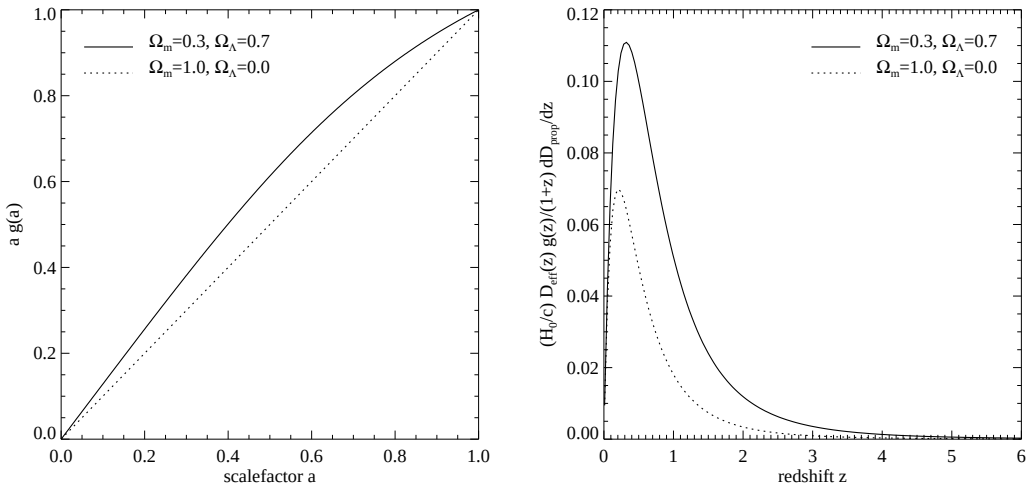

Figure 5.2: *Left panel*: Growth function $g(a)$ in an Einstein–de Sitter cosmology ($\Omega_m = 1$, $\Omega_\Lambda = 0$, dotted curve) and a ΛCDM Universe ($\Omega_m = 0.3$, $\Omega_\Lambda = 0.7$, solid line). *Right panel*: Lensing efficiency function D_{eff} with an observer at $z = 0$ and the CMB acting as source ($z = 1100$), weighted appropriately to produce the integrand of the effective convergence.

In our preferred ΛCDM cosmology ($\Omega_m = 0.3$, $\Omega_\Lambda = 0.7$), there is hardly any lensing contribution seen at redshifts larger than approximately 6.5. This can be estimated

integrating the efficiency, defining

$$e(0, z_s) = \int_0^{z_s} \mathrm{d}z \, \frac{\mathrm{d}D_{\mathrm{prop}}}{\mathrm{d}z} \frac{D_l D_{ls}}{D_s} \frac{g(z)}{1+z} \,. \tag{5.18}$$

Then the relative error introduced by neglecting lensing contributions of redshifts between z_{cut} and $z_{\mathrm{lss}} = 1100$ is

$$1 - \frac{e(0, z_{\mathrm{cut}})}{e(0, z_{\mathrm{lss}})} = 0.3\% \quad \text{for} \quad z_{\mathrm{cut}} = 6.7 \,. \tag{5.19}$$

This particular value for z_{cut} compromises between minimizing the relative error introduced and maximizing the field of view at this particular redshift. Taking this redshift $z_{\mathrm{cut}} = 6.7$, the appropriate comoving distance is $w \approx 6\,h^{-1}\,\mathrm{Gpc}$, using the ΛCDM cosmology and the formula given in (2.27). Thus, the corresponding maximum subtended angle is given by $\alpha_{\mathrm{max}} \approx x/w \approx 4.58°$, where $x = 480\,h^{-1}\,\mathrm{Mpc}$ is the comoving side length of the box.

5.3 Surface Density Power Spectra of the Projected Lens Planes

The three–dimensional density contrast $\delta(\vec{x}, w)$ was projected onto four lens planes per box, which are perpendicular to the line of sight and equally spaced in comoving coordinates, i.e. they are separated by $120\,h^{-1}\,\mathrm{Mpc}$. A particle located between w_i and w_{i+1}, the comoving distances of two adjacent lens planes, is projected onto the i–th lens plane in parallel to the third axis. Thus, the particle's projected comoving vector $\vec{x}$ is not changed. Since the N–body simulations are periodic in all directions, the projected particle distributions are also periodic in the lens planes. The projected surface overdensity field $\delta\Sigma(\vec{x})$ was smoothed onto 2048^2 (4096^2) square lattices from the projected discrete particle distribution using the triangular shaped cloud (TSC) assignment scheme (Hockney & Eastwood 1988). The resolution of the grid and the smoothing method were chosen in order to suppress the shot noise due to discreteness in N–body simulations at late times with the smoothing kernel while simultaneously maintaining a good enough resolution of the simulations for lensing studies.

5.3.1 Theoretical Expectations of the Surface Density Power Spectra

In this section, the theoretical expectation of the surface density power spectrum $P_{\delta\Sigma}(k_\perp)$ shall be derived in terms of the three–dimensional non–linear power spectrum $P_\delta(k)$ which is given by the analytic formulae of Peacock & Dodds (1996).

Here $(\vec{x}, w)$ form a local comoving Cartesian coordinate system, where $\vec{x}$ lies in the plane perpendicular to the comoving coordinate w along the line–of sight. The surface density Σ is given by the projection of the density field along the line–of–sight,

$$\Sigma(\vec{x}) = \int \mathrm{d}w \, \rho(\vec{x}, w) = \int \mathrm{d}w \, \bar{\rho} \, [\delta(\vec{x}, w) + 1] = \bar{\Sigma} + \bar{\rho} \int \mathrm{d}w \, \delta(\vec{x}, w) \,. \tag{5.20}$$

Using this projection, the surface overdensity field of lens plane i, $i = \{1, \ldots, 50\}$, is defined by

$$\delta\Sigma_i(\vec{x}) \equiv \frac{\Sigma_i(\vec{x}) - \bar{\Sigma}}{\bar{\Sigma}} = \frac{1}{\Delta w} \int_{w_i}^{w_i+\Delta w} \mathrm{d}w\, \delta(\vec{x}, w)\,, \tag{5.21}$$

where Δw characterizes the comoving separation between two adjacent lens planes, i.e. $\Delta w = 120\, h^{-1}\,\mathrm{Mpc}$. This choice guarantees the validity of the assumption of the multiple lens plane theory, namely that the spacing of two successive planes is much larger than the typical size of density fluctuations on the lens planes, which is of order $10\, h^{-1}\,\mathrm{Mpc}$.

We can now proceed like in the general case of Limber's equation in section (3.2), if we identify the q–parameter of equation (3.7) with Δw. Here, the only difference to the general case consists in the range of the projection integral which extends only over the finite distance between the lens planes. Nevertheless, the calculation is identical to section (3.2) until equation (3.10) which reads in this context

$$\xi_{\delta\Sigma_i} = \frac{1}{(\Delta w)^2} \int_{w_i}^{w_i+\Delta w} \mathrm{d}w \int \frac{\mathrm{d}^3k}{(2\pi)^3} P_\delta(|\vec{k}|, w) e^{-\mathrm{i}(\vec{k}_\perp \cdot \vec{x} + k_3 w)} e^{\mathrm{i}\vec{k}_\perp \cdot \vec{x}'} \int_{w_i}^{w_i+\Delta w} \mathrm{d}w'\, e^{\mathrm{i}k_3 w'}\,. \tag{5.22}$$

In order to perform the last integral, we shift the limits symmetrically around the origin and obtain the purely real result

$$\int_{-\Delta w/2}^{\Delta w/2} \mathrm{d}w'\, e^{\mathrm{i}k_3 w'} = \frac{2}{k_3} \sin\left(\frac{k_3 \Delta w}{2}\right)\,. \tag{5.23}$$

Now, we know that only the gravitational forces acting perpendicular to the line–of–sight deflect light rays. Consequently, the parallel component in Fourier space has a negligible contribution to the projected correlation function compared to the perpendicular one, $k_3 \ll k_\perp$, following the argument of Blandford et al. (1991). Hence we can approximate the integral with a delta distribution $2\pi\delta_D(k_3)$ such that the k_3–integration can easily be carried out, yielding

$$\xi_{\delta\Sigma_i}(\Delta\vec{x}) = \frac{1}{(\Delta w)^2} \int_{w_i}^{w_i+\Delta w} \mathrm{d}w \int \frac{\mathrm{d}^2k_\perp}{(2\pi)^2} P_\delta(|\vec{k}_\perp|, w) e^{-\mathrm{i}\vec{k}_\perp \cdot \Delta\vec{x}}\,. \tag{5.24}$$

In the following, we use the convenient redefinition $\Delta\vec{x} \to \vec{x}$ in order to calculate the power spectrum,

$$\begin{aligned} P_{\delta\Sigma_i}(k_\perp) &= \int \mathrm{d}^2x\, \xi_{\delta\Sigma_i}(\vec{x}) e^{\mathrm{i}\vec{k}_\perp \cdot \vec{x}} \\ &= \frac{1}{(\Delta w)^2} \int_{w_i}^{w_i+\Delta w} \mathrm{d}w \int \frac{\mathrm{d}^2k'_\perp}{(2\pi)^2} \int \mathrm{d}^2x\, P_\delta(|\vec{k}'_\perp|, w) e^{-\mathrm{i}(\vec{k}'_\perp - \vec{k}_\perp)\cdot\vec{x}} \\ &= \frac{1}{(\Delta w)^2} \int_{w_i}^{w_i+\Delta w} \mathrm{d}w\, P_\delta(|\vec{k}_\perp|, w)\,. \end{aligned} \tag{5.25}$$

So the surface density power spectrum is the appropriately scaled and projected three–dimensional power spectrum, the result one would have guessed intuitively.

5.3.2 Simulated Surface Density Power Spectra

We are now able to compare this theoretical formula with the power spectrum directly measured from the surface density maps. For doing so, we apply equation (3.5),

$$\left\langle \hat{\Sigma}_i(\vec{k}_\perp)\hat{\Sigma}_i^*(\vec{k}'_\perp)\right\rangle = (2\pi)^2\delta_D(\vec{k}_\perp - \vec{k}'_\perp)P_{\delta\Sigma_i}(|\vec{k}_\perp|)\,. \tag{5.26}$$

The procedure separates into two steps:

1. First the surface density fields are fast–Fourier transformed, yielding $\hat{\Sigma}_i(\vec{k}_\perp)$. Since the surface density maps are real, we can impose the additional symmetry in Fourier space,
$$\hat{\Sigma}_i(-\vec{k}_\perp) = \hat{\Sigma}_i^*(\vec{k}_\perp)\,. \tag{5.27}$$
2. From equation (5.26) we can see that the delta distribution $\delta_D(\vec{k}_\perp - \vec{k}'_\perp)$ limits the contributing modes to the power spectrum. Therefore we form the absolute square of the Fourier transforms, $|\hat{\Sigma}_i(\vec{k}_\perp)|^2$, which are subsequently binned logarithmically according to the norm of their wave vectors, $|\vec{k}_\perp|$. After performing the average, we obtain the desired result.

The following figure 5.3 shows the power spectrum of the surface density field which was computed on five different lens planes, all separated by the same comoving distance of approximately $1.5\,h^{-1}\,\mathrm{Gpc}$ (shown with crosses). They are compared to the theoretical prediction (5.25), represented by solid lines, respectively.

First considering the time evolution of the surface density power spectra in the theoretical prediction, we can see increasing power of correlations on all scales, in the progress of evolution as inhomogeneities grow. Moreover, the non–linear property of the power spectrum, which is visible as a substantial enhancement at small scales, affects larger and larger scales when evolving forward in time.

Comparing now the theoretical prediction with the simulated measured power spectra reveals good agreement on large scales irrespective of an increasing scatter below $k_\perp \sim 0.2\,h^{-1}\,\mathrm{Mpc}$, the *cosmic variance*, because of the limited number of long–wavelength modes on these scales. This effect will be addressed in detail in section 7.1.4.

However a prominent feature appears on small scales at large redshift in the simulations. This is due to the initial conditions of the "glass"–like distribution of particles in the simulations and situated at the mean inter–particle separation

$$\bar{d}_{\mathrm{com}} = \bar{d}_{\mathrm{phys}}(1+z) = \sqrt[3]{\frac{m_{\mathrm{part}}}{\rho_{\mathrm{cr}}\,\Omega_m(1+z)^3}}(1+z) = \sqrt[3]{\frac{m_{\mathrm{part}}}{\rho_{\mathrm{cr}}\,\Omega_m}} = 0.937\,h^{-1}\,\mathrm{Mpc}\,, \tag{5.28}$$

which is independent of redshift, as it should be. The corresponding wavelength is $k_\perp = 2\pi/\bar{d}_{\mathrm{com}} = 6.7\,h\,\mathrm{Mpc}^{-1}$. This feature is merely an effect of the initial conditions and does not develop gravitationally. In contrast, it even gets "washed out" as structures grow and develop correlations on these scales.

The lack of power on small scales at low redshift is due to the missing resolution of the grid of the smoothed surface density field. All curves meet at $k_\perp \approx 40\,h\,\mathrm{Mpc}^{-1}$,

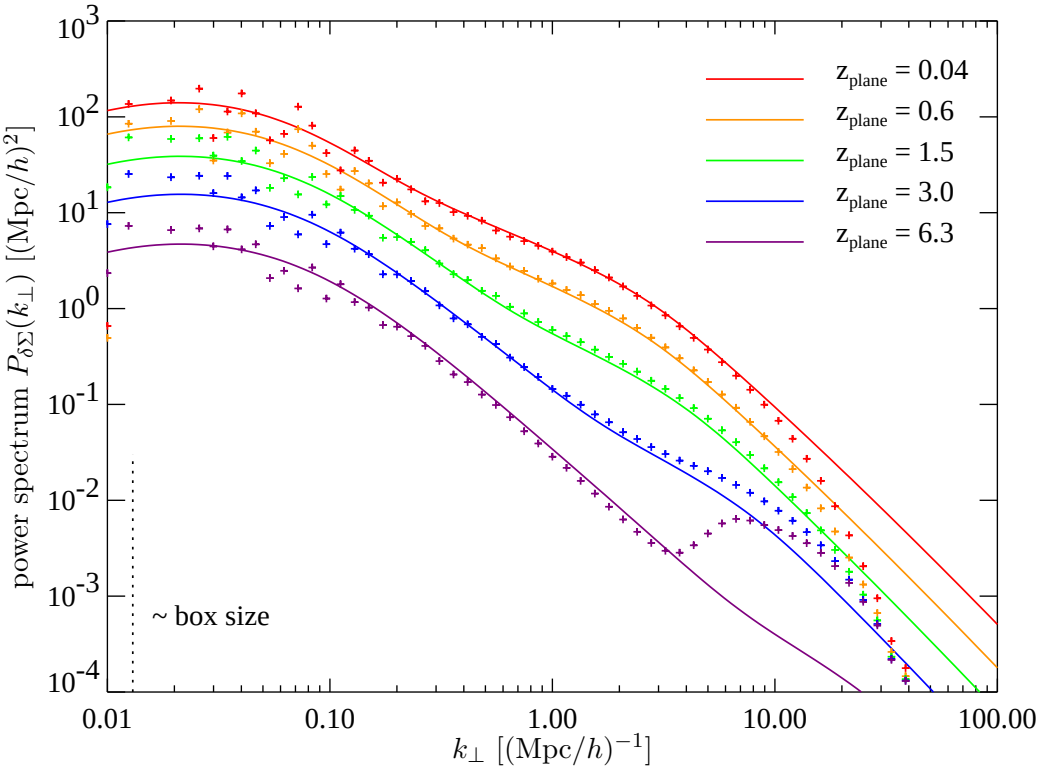

Figure 5.3: Surface density power spectra $P_{\delta\Sigma_i}(|\vec{k}_\perp|)$ of different lens planes at their redshifts z_i, respectively. Comparison of the theoretical prediction (solid lines) to the "measured" power spectra of the simulations (crosses).

---

indicating the smoothing effect due to the TSC kernel in order to suppress the contribution of white noise, which dominates on yet smaller scales.

5.4 Power Spectrum of the Effective Convergence P_κ

To proceed further, the lensing potential of the N–body simulations shall be studied. This can be done by simulating the power spectrum of the effective convergence using the previously obtained surface density power spectra. In principle, this gives a measure of the total statistical lensing information included in the cosmological simulations.

5.4.1 Theoretical Derivations of the Power Spectrum of the Effective Convergence

Theoretical expectation The power spectrum of the effective convergence κ_{eff} in terms of the non–linear density power spectrum P_δ is given by equation (4.47) in the "effective" theory,

$$P_\kappa(\ell) = \frac{9H_0^4\Omega_m^2}{4c^4}\int_0^{w_{\text{cut}}} \mathrm{d}w \left(\frac{f_K(w_s-w)}{f_K(w_s)a(w)}\right)^2 P_\delta\left(\frac{\ell}{f_K(w)}, w\right). \tag{5.29}$$

In principle, the upper integration limit w_{cut} should be identical to the comoving distance to the source, w_s. For statistical reasons of the ray tracing method, we impose an upper limit of the number of lens planes (see section 5.2.2). This can be modeled in the theoretically obtained power spectrum by lowering the upper integration limit w_{cut}.

Derivation of the Formula for the Simulated P_κ Now, the task consists in relating the surface density power spectra of the individual lens planes $P_{\delta\Sigma_i}(k_\perp)$ to the power spectrum of the effective convergence $P_\kappa(\ell)$. The surface density power spectrum $P_{\delta\Sigma_i}$ is given by equation (5.25), which can be further approximated, assuming a slowly varying density power spectrum P_δ over the projection distance of the lens planes, namely

$$P_{\delta\Sigma_i}(k_\perp) = \frac{1}{(\Delta w)^2}\int_{w_i}^{w_i+\Delta w} \mathrm{d}w\, P_\delta(|\vec{k}_\perp|, w) \simeq \frac{1}{\Delta w} P_\delta(|\vec{k}_\perp|, w_i)\,. \tag{5.30}$$

Taking equation (5.29) and breaking up the integral into individual projection distances yields

$$P_\kappa(\ell) = \frac{9}{4}\left(\frac{H_0}{c}\right)^4\left(\frac{\Omega_m}{f_K(w_s)}\right)^2\sum_{i=1}^{N}\int_{w_i}^{w_i+\Delta w} \mathrm{d}w \left(\frac{f_K(w_s-w)}{a(w)}\right)^2 P_\delta\left(\frac{\ell}{f_K(w)}, w\right). \tag{5.31}$$

Assuming furthermore that both the comoving angular diameter distance $f_K(w_s-w)$ and the scale factor $a(w)$ are slowly varying over the integration range Δw, and using equation (5.30) yields the final result for the simulated power spectrum of the effective convergence,

$$P_\kappa(\ell) = \frac{9}{4}\left(\frac{H_0}{c}\right)^4\left(\frac{\Omega_m}{f_K(w_s)}\right)^2(\Delta w)^2\sum_{i=1}^{N}\left(\frac{f_K(w_s-w_i)}{a(w_i)}\right)^2 P_{\delta\Sigma_i}\left(\frac{\ell}{f_K(w_i)}, w_i\right), \tag{5.32}$$

using the relation $k_\perp = \ell/w$. Thus, the power spectrum P_κ of the effective convergence is given by a sum over the surface density power spectra $P_{\delta\Sigma_i}$, suitably normalized by some weighting functions according to Limber's equation. For convenience, the comoving distance w is taken to be the independent variable such that the scale factor a also depends on w. In practice, the Newton–Raphson method is used to solve for

the scale factor, given the comoving distance w (see equation (2.27)). Since $P_{\delta\Sigma_i}$ has the dimension of a squared length, the power spectrum of the effective convergence P_κ is dimensionless.

5.4.2 Simulated Power Spectra of the Effective Convergence

The following figure 5.4 shows the simulated power spectrum of the effective convergence in comparison to its theoretical prediction. The graphs show the power spectra from the bottom to the top with a source redshift $z_s = 1$ (green), $z_s = 5$ (orange) and the redshift of the surface of last scattering, $z_s = 1100$ (red). The red line uses the approximation that there is no density perturbation above a redshift $z_{\text{cut}} = 6.7$, according to equation (5.29), while the blue line corresponds to the correct power spectrum assuming density perturbations up to the surface of last scattering.

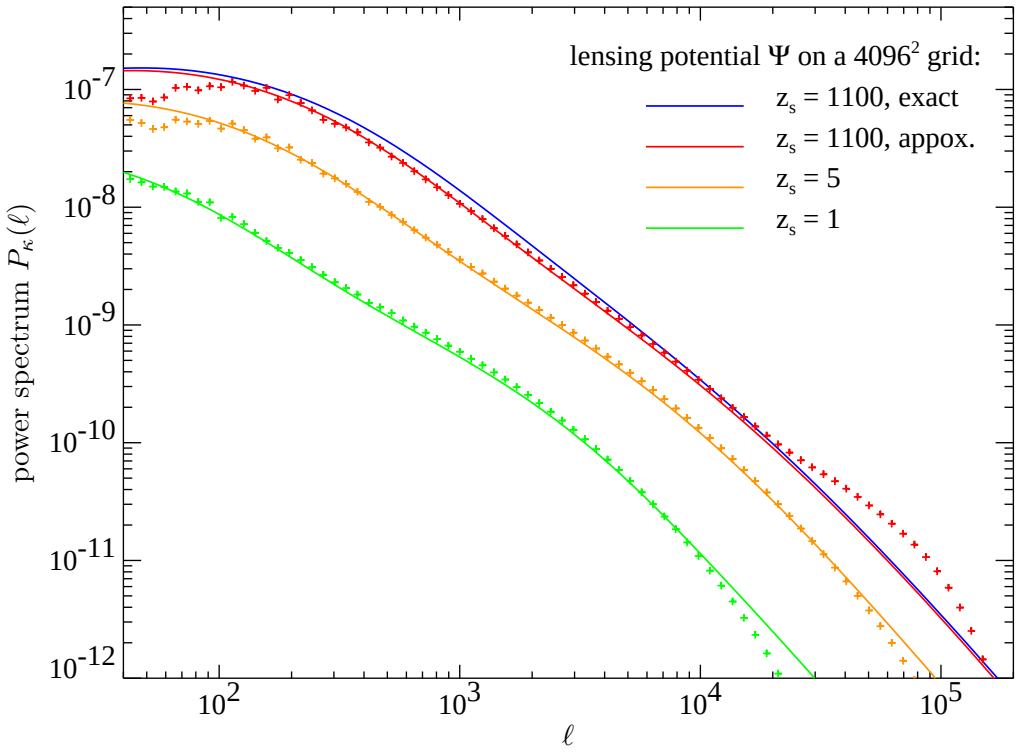

Figure 5.4: Power spectra of the effective convergence $P_\kappa(\ell)$ at different source redshifts z_s, respectively. Comparison of the theoretical prediction (solid lines) to the "measured" power spectra of the simulations (crosses).

At a glance, there is perfect agreement between the theoretical prediction and the measured power spectra of the simulations on scales between $\ell \simeq 100$ and $\ell \simeq 2 \cdot 10^4$,

depending on the source redshift. This means that the theoretical expectation from the "effective" theory and the multiple lens plane approach agree very well on these scales.

On angular scales larger than $\phi \simeq 1.8^\circ$ corresponding to $\ell \lesssim 100$, there is power missing in the simulated curves due to a combination of the following two effects: (i) The lens planes on which the surface density power spectra are measured at high redshifts corresponding to a large comoving distance to the observer subtend a smaller solid angle than the lens planes at low redshift. Thus, in Fourier space a fixed absolute value of the physical wave vector $k_\perp$ corresponds to larger values of ℓ for lens planes further away from the observer, i.e. larger comoving distance, according to $\ell = k_\perp w$. (ii) The side length of the box determines a minimum wave number in Fourier space, $k_\perp = 2\pi/L_{\rm box}$, below which there is no power in the power spectrum. Combining these two effects leads to an underestimate of power due to the non–accounting of scales larger than the side length of the box at the most distant lens planes. In principle, this effect could easily be corrected by inserting the theoretical linear power spectrum. Since we ultimately want to study lensing effects on the CMB which start being important at $\ell \gtrsim 800$, we ignore this angular resolution effect.

In the case of the power spectra at source redshift $z_s = 1$ and $z_s = 5$, the simulated power spectra start to deviate slightly from the theoretical prediction on the smallest scales. This is due to the same angular resolution effect combined with the resolution limit of the mean inter–particle separation of the N–body simulations (see also signal–to–noise estimates in figure 5.1).

In the case of source redshift $z_s = 1100$, there is a prominent enhancement visible on the smallest scales. The reason for this is the effect of the initial conditions of the original N–body simulations. This hypothesis was confirmed by simulations whose results are shown in figure 5.5.

For the orange curve in the left panel we ignored density fluctuations above redshifts $z = 3$, i.e. the lens planes with the remaining "glass"–like effect were neglected. There is almost no excess on small scales which proves the excess in the red graph is due to the effect discussed above.

In the right panel, the resolution of the lensing potential on each of the lens planes was lowered by a factor of 4 in order to get rid of the excess on small scales. But the effect of missing power on these small scales due to the lower resolution is also clearly visible. Nevertheless we decided to adopt this lower resolution of the lensing potential Ψ in order to perform ray tracing simulations in chapter 6. Summarizing this chapter, the N–body simulations are well suited for studying lensing properties by ray tracing simulations.

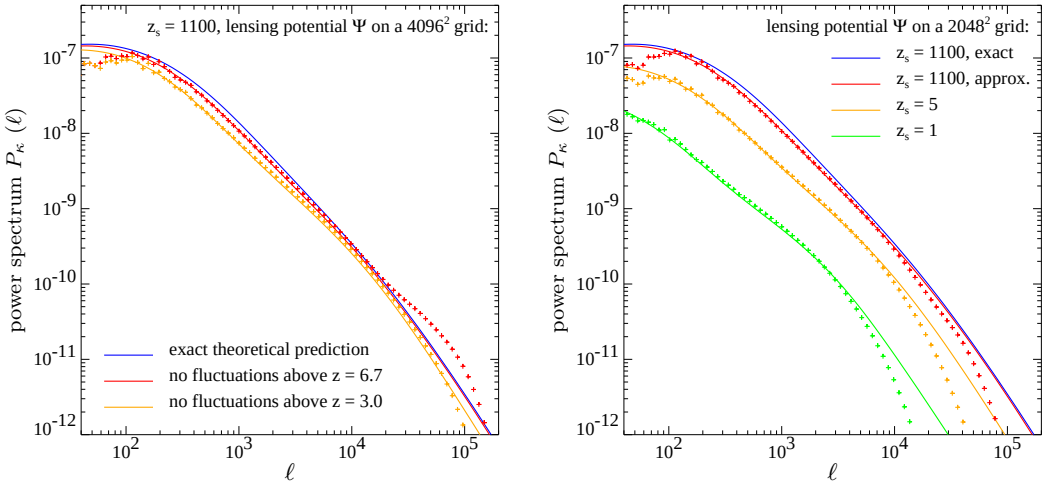

Figure 5.5: *Left panel*: Simulations revealing the origin of the enhancement in the power spectrum P_κ at small scales. The red crossed graph integrates out to redshift $z_s = 6.7$ whereas the orange graph only takes into account lens planes up to $z_s = 3$ with a negligible contribution of the "glass" effect. *Right panel*: Same simulations as in figure 5.4, but, using a lower resolution of the lensing potential grid in order to get rid of the "glass" effect.

6 Ray Tracing Photons through a Simulated ΛCDM Universe

This chapter is devoted to the ray tracing simulations. Photons are traced back on their past light cone through cosmological N–body simulations by means of the multiple lens plane theory. The ray tracing simulations of this chapter are based on earlier work by Hamana & Mellier (2001).

6.1 Structure of the Ray Tracing Simulations

Ray tracing effectively results in applying the multiple lens plane theory to geodesics of individual photons, i.e. evaluating both equation (4.58) for the position of a given photon at the lens plane j, $\vec{\theta}_j$, and equation (4.61) for the Jacobian matrix, $\mathcal{A}_j$, at this position backward in time. This backward propagation ensures that all photons reach the observer. For completeness and convenience, these two equations are repeated here:

$$\vec{\theta}_j = \vec{\theta}_1 - \sum_{i=1}^{j-1} \frac{f_K(w_j - w_i)}{f_K(w_j) a_i} \vec{\nabla}_x \tilde{\Psi}_i(\vec{x}) \,, \tag{6.1}$$

$$\text{and} \qquad \mathcal{A}_j = \mathcal{I} - \sum_{i=1}^{j-1} \frac{f_K(w_i) f_K(w_j - w_i)}{f_K(w_j) a_i} \tilde{\mathcal{U}}_i \mathcal{A}_i \tag{6.2}$$

$$\text{where} \qquad \tilde{\mathcal{U}}_i \equiv \begin{pmatrix} \tilde{\Psi}_{i,11}(\vec{x}) & \tilde{\Psi}_{i,12}(\vec{x}) \\ \tilde{\Psi}_{i,21}(\vec{x}) & \tilde{\Psi}_{i,22}(\vec{x}) \end{pmatrix} .$$

In order to perform ray tracing, the local deflection angles $\vec{\nabla}_x \tilde{\Psi}_i$ as well as the tidal matrices $\tilde{\mathcal{U}}_i = (\partial^2_{kl} \tilde{\Psi})_i$ on the lens planes i, $i = \{1, \ldots, 50\}$, need to be computed in a preparatory step. Here $\{k, l\} \in \{1, 2\}$ as they represent the two comoving coordinates on the lens planes.

The ray tracing algorithm can be split into three distinct parts: Projecting the three–dimensional density fields onto lens planes, computing the local deflection angles and the tidal matrices on each plane, and using them recursively in order to propagate the photon trajectories along the past light cone.

This is summarized in the following illustration:

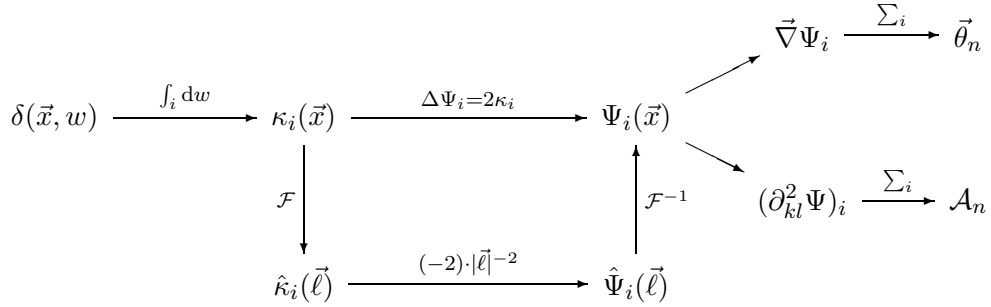

(6.3)

1. The projection and subsequent smoothing procedure of the density distribution has already been addressed in detail in chapter 5.

2. Instead of performing the convolution integral over the Green's function in real space (equation (4.21)), the lensing potential Ψ_i is obtained by means of the fast Fourier transform with periodic boundary conditions. This assumption is valid because of the periodicity of the original structure formation simulations. The gradient and the second derivatives are evaluated on the lattice in real space using the finite difference method (see Premadi, Martel & Matzner (1998)) and yielding the deflection angle field $\vec{\nabla}_x\tilde{\Psi}_i(\vec{x})$ and the tidal matrices $\tilde{\mathcal{U}}_i$ on each lens plane i.

3. The photons are initialized on a regular 1024^2–point grid on the first lens plane close to the observer with an initial grid separation of 0.25 arcmin. Thus, the first lens plane is the image plane with the unperturbed photon positions. For each photon trajectory, its position is computed on all lens planes iteratively using equation (6.1). The first and second derivatives of the unscaled lensing potential $\tilde{\Psi}_i$ are linearly interpolated from the lens plane grid to the perturbed photon position, yielding the photon's angular position on the source plane, $\vec{\theta}_n$. Therefore, large scale perturbations along the line–of–sight effectively result in distortions of the grid. Finally, equation (6.2) is solved for the Jacobian $\mathcal{A}_n$ of the mapping from the last lens plane, being identified with the source plane, to the image plane. In addition to the deflection angle field on the source plane, this procedure yields also effective fields of the convergence κ_{eff} and the two components of the shear γ_{eff} on the source plane, whose statistics are studied in the following.

In total, 50 different realizations of the underlying density field are obtained by randomly choosing the origin of each box during the ray tracing simulations, assuming periodic boundary conditions. For maintaining the clustering in each box and therefore the coherent large scale modes, lens planes from the same box are treated equally. Certainly, these realizations are not statistically independent, yet this provides a compromise between extracting as much statistical information as possible and the limited numerical resources.

6.2 Resolution Studies and Uncertainty Estimates

6.2.1 Effective Resolution of the Evolution Equations

In principle, the angular resolution of the ray tracing simulation is only limited by the spatial resolution of the TSC smoothing grid. In section 5.4.2, we decided to adopt a grid spacing of

$$d_{\rm res} = \frac{L_{\rm box}}{N_{\rm side}} = \frac{480\,h^{-1}\,{\rm Mpc}}{2048}\,, \tag{6.4}$$

which can be converted into angular scale using the angular diameter distance relation in comoving units, $d_{\rm res} = f_K(w)\theta_{\rm res}$. The panel on the right–hand side in figure 6.1 shows such an angular scale computed for the flat ΛCDM cosmology. Therefore it increases strongly as $\theta_{\rm res} \propto w^{-1}$ for redshifts $z \lesssim 0.5$. The impact of this lower resolution at low redshifts depends strongly on the distance weighting functions in the evolution equations (6.1) and (6.2). Including this distance weighting effect into the numerical resolution, one talks about *effective resolution*.

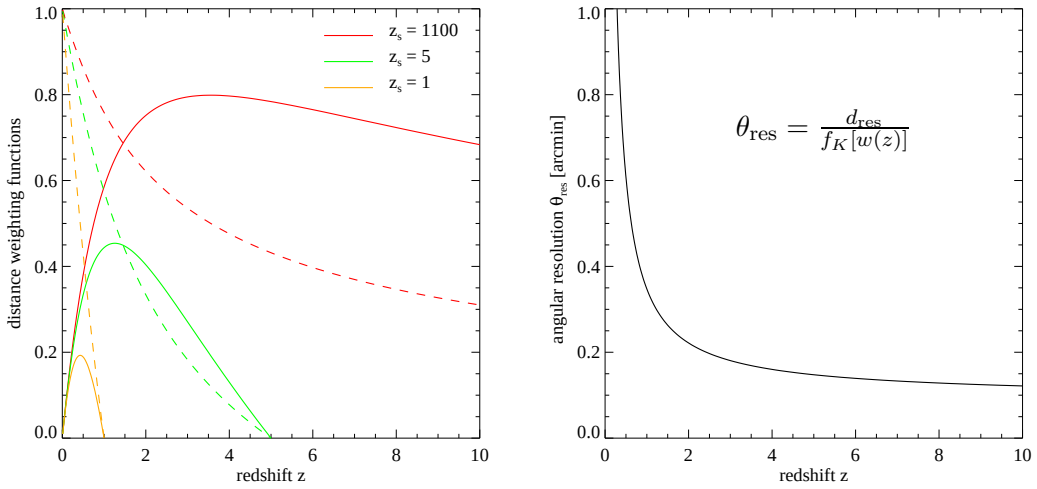

Figure 6.1: *Left panel*: Distance combinations acting as weighting functions in the evolution equations for different source redshifts. The dashed line shows the combination of the comoving angular diameter distances D_{ls}/D_s of equation (6.1) and the solid line represents the combination $D_{ls}D_l/D_s$ in units of c/H_0 of equation (6.2). *Right panel*: Angular resolution $\theta_{\rm res}$ as a function of redshift.

Let us first consider the effective resolution of the convergence and the shear, which are obtained by solving the evolution equation for the Jacobian matrix, equation (6.2) describing the mapping from the source plane n to the image plane. The distance combination, appearing in this equation as a weighting function, is $f_K(w_i)f_K(w_n - w_i)/f_K(w_n)$, where the different distances are comoving angular diameter distances from the observer to lens plane i, from lens plane i to the source and from the observer

to the source, respectively. This distance combination is shown as solid lines for different source redshifts z_s in the left panel in figure 6.1, normalized by the Hubble length, c/H_0. It peaks at intermediate redshifts, depending on the source redshift. Therefore, the lower resolution of the simulations on low redshift lens planes has only a small effect on the effective resolution of the components of the Jacobian, the convergence κ and the shear γ, in all cases of interest for our source redshifts ($z_s > 1$).

In contrast to that, the dimensionless distance combination appearing in the evolution equation of the lensing deflection angle, $f_K(w_n - w_i)/f_K(w_n)$, is shown as dashed curves in the left panel in figure 6.1 at different redshifts. This function has its largest value at redshift zero while declining to higher redshifts indicating that lensing deflections due to inhomogeneities at low redshift are higher weighted than those at high redshift. Thus, the statistics of the deflection angle should pick up the lower resolution at low redshifts giving rise to a much smaller effective resolution in comparison to that of the components of the Jacobian.

As an example, the resolution of the first lens plane at redshift $z_1 = 0.04$ is $\theta_{\rm res} = 6.6$ arcmin, corresponding to a value of $l \approx 1640$ in Fourier space. On these scales, we would expect to see small deviations of the statistics of the lensing deflection angle compared to theoretical predictions (see also section 6.3.3 and Appendix B.1).

6.2.2 Uncertainty Estimate of the Growth Function

As previously outlined in section (5.3), the ray tracing method for lensing studies is strongly based on the underlying projected density distributions. In practice, these density distributions are taken from cosmological boxes of comoving side length $L_{\rm box} = 480\,h^{-1}$Mpc, which represent snapshots of formed structure at a particular mean box redshift. Therefore, the evolution of structure within a given box, while the photons were propagating through, was neglected in the ray tracing simulations. Only the structure evolution from one box to another was considered. Commonly, it is assumed that these effects of structure being passed by photons earlier and later compared to the mean redshift of the box average out. Nevertheless, in the following, we derive an estimate of the maximum uncertainty introduced by the consideration of photons passing structure at the box boundary in the line–of–sight which represents the worst case. The true density contrast of structures at the box boundary at redshift z', denoted by $\delta(\vec{x}, z')$, is compared to the mean density contrast of the box at z, $\delta(\vec{x}, z)$. Defining the effective growth function by $G_+[a(z)] \equiv a(z)g[a(z)]$, which is normalized to unity at the present time, (see equation (2.46)) and using the Taylor expansion yields

$$\begin{aligned}\delta(\vec{x}, z') &= \delta_0(\vec{x}) G_+[a(z)] \left(1 + \frac{1}{G_+[a(z)]} \left|\frac{\mathrm{d}G_+(a)}{\mathrm{d}a}\right|(z) \left|\frac{\mathrm{d}a}{\mathrm{d}w}\right|(z)\, \Delta w\right) \\ &\equiv \delta_0(\vec{x}) G_+[a(z)] \left(1 + \frac{1}{G_+[a(z)]} \Delta G_+[a(z)]\right), \end{aligned} \tag{6.5}$$

where $\Delta w = 240\,h^{-1}$Mpc, which is half the side length of the box. Using the fact the photons travel on null geodesics which are taken to be radial, $|c\,\mathrm{d}t| = a\mathrm{d}w$, the

derivative of the scale factor is obtained by

$$\frac{\mathrm{d}a}{\mathrm{d}w} = \frac{\mathrm{d}a}{\mathrm{d}t}\frac{\mathrm{d}t}{\mathrm{d}w} = \frac{\dot{a}a}{c} = \frac{\dot{a}}{a}\frac{a^2}{c} = \frac{H_0}{c}\sqrt{a\Omega_m + a^2(1-\Omega_m-\Omega_\Lambda) + a^4\Omega_\Lambda}\,, \tag{6.6}$$

Figure 6.2 shows the maximum relative uncertainty of the effective growth function $\Delta G_+(a)/G_+(a)$ as a function of redshift z from neglecting evolution of structure within the cosmological boxes. The plot shows the worst case, i.e. each redshift z corresponds to photons passing structure at the box boundary in the line–of–sight, where we have the largest deviation of the growth function compared to the mean of the box. In both cases of an Einstein–de Sitter model and a flat ΛCDM Universe, $\Delta G_+(a)/G_+(a)$ is rising at larger redshifts, indicating stronger influence of this effect at earlier times. Fortunately, these high redshifts are suppressed by the lensing efficiency function (see section 5.2.2).

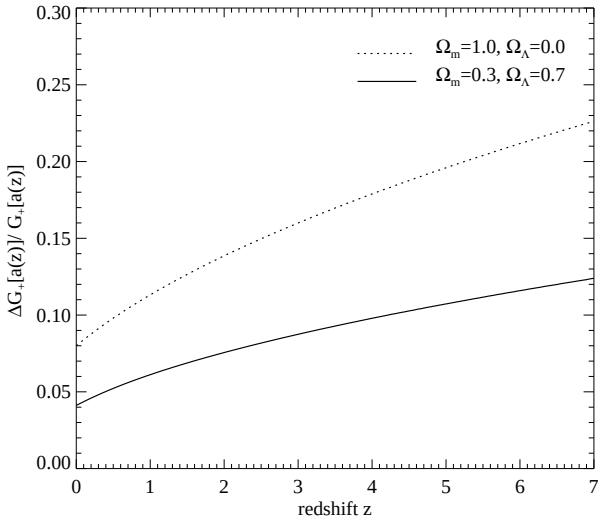

Figure 6.2: Maximum relative uncertainty in the effective growth function $\Delta G_+(a)/G_+(a)$ as a function of redshift z from neglecting evolution of structure within the cosmological boxes. Comparison of a flat ΛCDM Universe (solid line) to an Einstein–de Sitter model (dotted line).

6.3 Results and Discussion of the Ray Tracing Simulations

6.3.1 Images of the Effective Convergence

The following three pictures show a particular realization of the effective convergence field κ_{eff} situated at the source redshift of $z_s = \{1, 5, 1100\}$. Individual prominent features are clearly seen developing with higher source redshifts, corresponding to the increasing amount of surface mass density being passed by the photons and suitably weighted by the lensing efficiency function $D_{ls}D_l/D_s$ responsible for isotropic magnification.

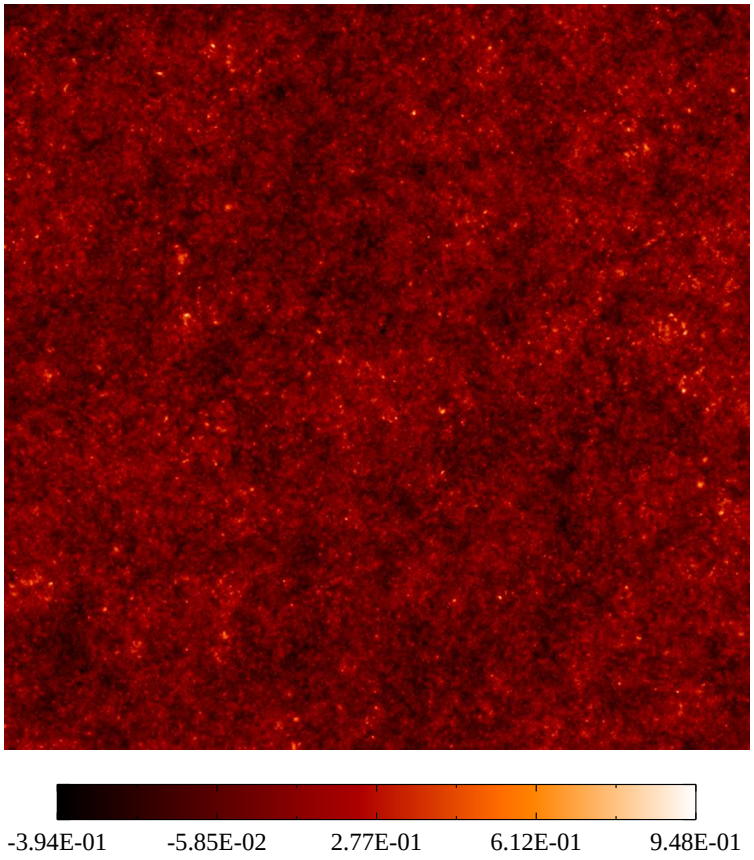

Figure 6.3: Effective convergence field $\kappa_{\text{eff}}(\vec{\theta})$ of angular size $\theta \simeq 4.27°$, assuming sources at the last scattering surface at $z_s = 1100$. For the simulation, only density perturbations up to $z_{\text{cut}} = 6.7$ were considered.

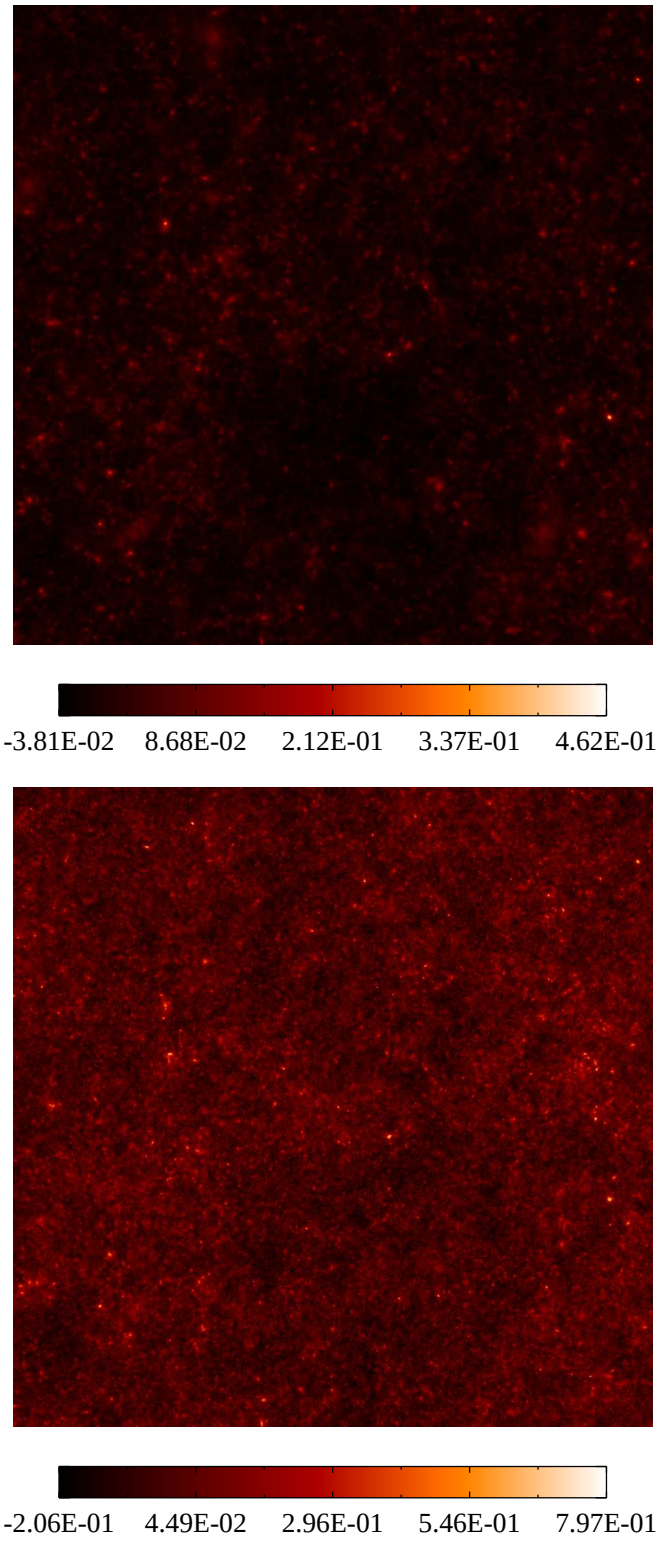

Figure 6.4: Effective convergence fields $\kappa_{\rm eff}(\vec{\theta})$ of angular size $\theta \simeq 4.27°$, assuming source redshifts of $z_s = \{1, 5\}$ for the upper and lower panel, respectively.

6.3.2 Probability Distribution Function

In the following figure, the probability distribution function (PDF) of the effective convergence $\kappa_{\text{eff}}(\vec{\theta})$ of the previously shown realizations assuming source redshifts of $z_s = \{1, 5, 1100\}$ are shown.

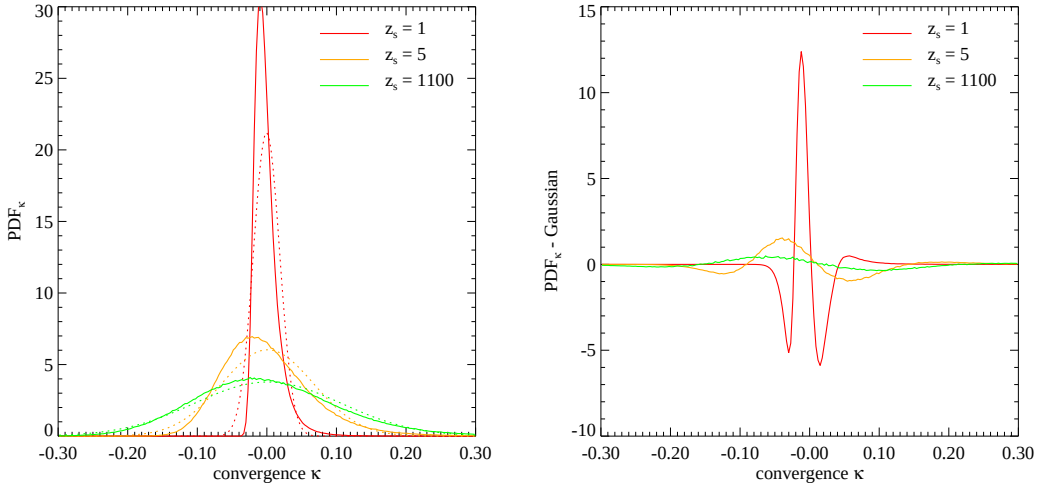

Figure 6.5: Probability distribution functions (PDFs) of the effective convergence $\kappa_{\text{eff}}(\vec{\theta})$ at different source redshifts of $z_s = \{1, 5, 1100\}$ normalized such that the integrals over the PDFs equal unity. *Left panel*: PDFs of κ_{eff} (solid line) are compared to Gaussians with the same mean and variance (dotted line). *Right panel*: Difference of the PDFs and their corresponding Gaussians.

For completeness, the following table shows the mean μ_κ and the standard deviation σ_κ of the PDFs of the effective convergence at their source redshifts z_s, respectively.

z_s	1	5	1100
$\mu_\kappa \cdot 10^{-3}$	0.47	1.12	1.41
$\sigma_\kappa \cdot 10^{-1}$	0.19	0.66	1.06

Theoretically, the effective convergence $\kappa_{\text{eff}}(\vec{\theta})$ of a source at comoving distance w_s is given by equation (4.44),

$$\kappa_{\text{eff}}(\vec{\theta}, w_s) = \frac{3H_0^2\Omega_m}{2c^2} \int_0^{w_s} \mathrm{d}w' \, \frac{f_K(w_s - w') f_K(w')}{f_K(w)} \frac{\delta[f_K(w')\vec{\theta}, w']}{a(w')} \,. \tag{6.7}$$

Since the effective convergence κ_{eff} is proportional to the projected density contrast δ along the line–of–sight, the evolution of δ is crucial for understanding κ_{eff}.

Overdense regions with $\delta > 0$, and therefore also $\kappa > 0$, have collapsed into dense structures leading to a non–Gaussian tail of high κ in the probability distribution

function. This is particularly visible for low source redshifts z_s. In rarefactions corresponding to $\kappa < 0$ along this line–of–sight, non–linear evolution is responsible for taking matter from underdense regions into collapsed halos or filaments connecting them.

In the linear regime, the time evolution of different Fourier modes is statistically independent, allowing information from different scales to be combined. It is commonly assumed, that the amplitudes of the Fourier modes are Gaussian distributed. Non–linear gravitational evolution on small scales develops correlations between Fourier modes that were uncorrelated in the linear regime leading to non–Gaussian distributions.

Returning to the measured probability distribution functions of the effective convergence, the presented descriptions of the evolution of δ allows convincing explanations of the visible effects. The deviations from Gaussianity are larger at low z_s because of the following two reasons: (i) As the source redshift increases, more independent regions are projected due to the larger integration range. By the central limit theorem, this yields a Gaussian distribution, even though the PDF of the three–dimensional density contrast is very non–Gaussian. It follows approximately a log normal distribution (Jain, Seljak & White 2000), which has a lower bound at $\delta = -1$ due to the definition of δ and extends to high values of $\delta \sim 10^6$ in galaxies, for instance. (ii) On the other hand for low z_s, the lensing efficiency function enhances the non–linear regime of the density evolution and causes the PDF of $\kappa_{\rm eff}$ to become highly non–Gaussian.

The variance of the PDF of $\kappa_{\rm eff}$ is increasing with source redshift z_s. This is due to the effect of the integrated light cone covering a larger sample at higher redshift of both voids and gravitationally bound objects like galaxies and clusters of galaxies, which broadens the PDF.

6.3.3 Power Spectra of different Lensing Quantities

Convergence Power Spectrum In the following, the power spectrum of the effective convergence $P_\kappa(\ell)$, which has been measured directly from the ray tracing simulations, is compared to the theoretical prediction (equation (4.47)).

Assuming the flat sky approximation, we can apply equation (3.5),

$$\left\langle \hat{\kappa}_i(\vec{\ell})\hat{\kappa}_i^*(\vec{\ell}')\right\rangle = (2\pi)^2\delta_D(\vec{\ell}-\vec{\ell}')P_\kappa(|\vec{\ell}|)\,. \tag{6.8}$$

Then, the method yielding the power spectrum proceeds in analogy to section 5.3.2: After fast–Fourier transforming the convergence fields, leading to $\hat{\kappa}(\vec{\ell})$, the absolute squares of the Fourier transforms are computed, $|\hat{\kappa}(\vec{\ell})|^2$, which are subsequently binned logarithmically according to the norm of their wave vectors, $|\vec{\ell}|$, and averaged in order to obtain the power spectrum.

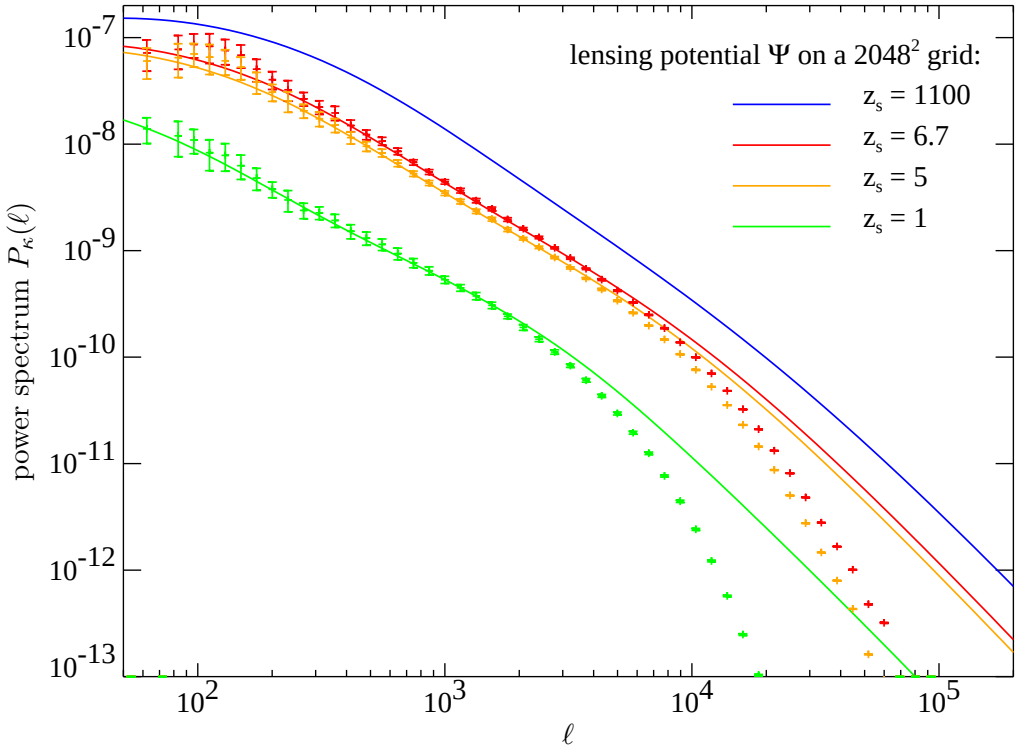

Figure 6.6: Power spectra of the effective convergence $P_\kappa(\ell)$ at different source redshifts z_s. Comparison of the theoretical prediction (solid lines) to the "measured" power spectra of ray tracing simulations (crosses).

The graphs in the figure 6.6 show the power spectra from the bottom to the top with source redshifts $z_s = 1$ (green), $z_s = 5$ (orange) and $z_s = 6.7$ (red). The theoretical

blue curve corresponds to a source redshift of $z_s = 1100$, whereas the average and the standard deviation of the curves obtained by the ray tracing algorithm were taken over 50 realizations.

The power spectra agree quite well on large scales, whereas some power is lacking on small scales due to the finite resolution on the 2048^2–point grid, on which the lensing potential Ψ was computed. The larger error bars at large scales are due to cosmic variance.

Shear Power Spectrum Proceeding further, the power spectrum of the effective shear as measured directly from the ray tracing simulations, shall be compared to the theoretical prediction of the convergence power spectrum $P_\kappa(\ell)$. According to equation (4.51), they should agree identically.

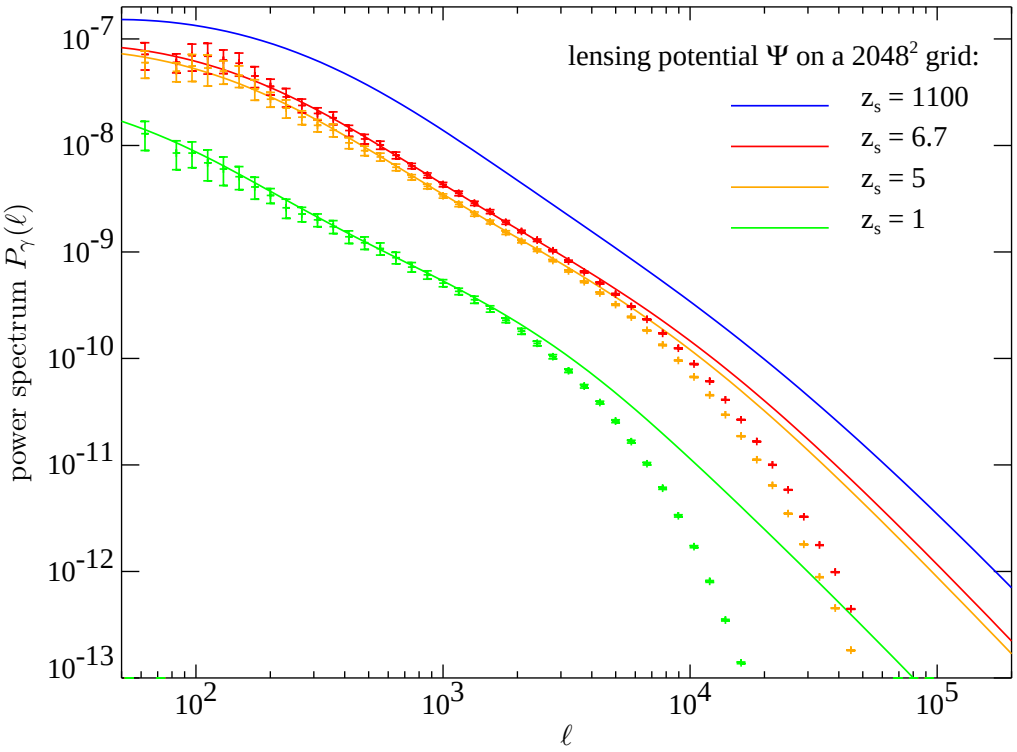

Figure 6.7: Power spectra of the effective shear $P_\gamma(\ell)$ at different source redshifts z_s. Comparison of the "measured" shear power spectra of ray tracing simulations (crosses) to the theoretical prediction of the convergence power spectra $P_\kappa(\ell)$ (solid lines).

The procedure for obtaining the shear power spectrum follows the one presented in the previous paragraph, however, taking now the two components of the shear, γ_1 and γ_2, which are related to the total shear by $\gamma^2 \equiv \gamma_1^2 + \gamma_2^2$. The color coding of

the shear power spectrum $P_\gamma(\ell)$ in figure 6.7 is the same as in the previous figure 6.6 and the average and the standard deviation were also taken over 50 realizations. The agreement with the theoretical convergence power spectrum $P_\kappa(\ell)$ is excellent except for the resolution effect on small scales and the effect of cosmic variance on large angular scales, which are comparable to figure 6.6.

Power Spectrum of the Lensing Deflection Angle Finally, the power spectrum of the lensing deflection angle $P_{\vec{\alpha}} = P_{\alpha_1} + P_{\alpha_2}$ was measured from the ray tracing simulations using the same procedure as in the two previous paragraphs. The lensing deflection angle $\vec{\alpha}$ itself is obtained by means of the lens equation (4.15),

$$\vec{\alpha}(\vec{\theta}) = \vec{\theta} - \vec{\beta}(\vec{\theta})\,, \tag{6.9}$$

where the angular position on the image plane is denoted by $\vec{\theta} \equiv \vec{\theta}_1$ (*regular grid*) and the angular position on the source plane is given by $\vec{\beta} \equiv \vec{\theta}_n$ (*distorted grid*, computed by the ray tracing algorithm). The power spectrum of the lensing deflection angle $P_{\vec{\alpha}}$ is subsequently compared to the modified convergence power spectrum $P_\kappa(\ell)$, according to equation (4.53),

$$P_{\vec{\alpha}}(\ell) = \frac{4}{\ell^2} P_\kappa(\ell)\,. \tag{6.10}$$

The graphs in figure 6.8 show the power spectra from the bottom to the top for source redshifts $z_s = 1$ (green), $z_s = 5$ (orange) and the redshift of the surface of last scattering, $z_s = 1100$ (red). The average and the standard deviation were also taken over 50 realizations.

The power spectrum systematically picks up power on small scales, especially at low source redshifts z_s. This seems to be an effect of the effective resolution (see section 6.2.1), which has a weaker influence at high redshifts due to the stronger distortions of the regular grid by the higher number of passed lens planes. This hypothesis is also supported by a set of simulations checking the linear interpolation routine of the code (see Appendix B.2). In principle, there could also be other sources, which would lead to such an enhancement like shot noise, or a failure of the weak lensing approximation on these scales. However, these are less likely compared to the previously discussed effective resolution effect.

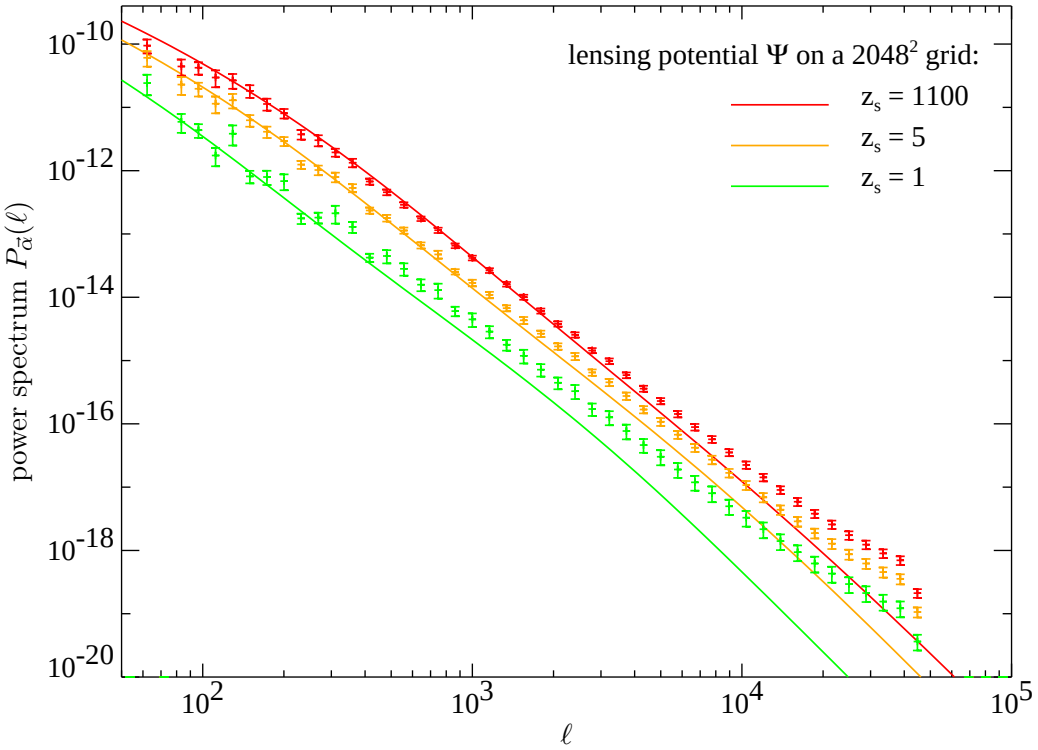

Figure 6.8: Power spectra of the effective deflection angle $P_{\vec{\alpha}}(\ell)$ at different source redshifts z_s. Comparison of the theoretical prediction (solid lines) to the "measured" power spectra of ray tracing simulations (crosses).

7 Lensing the Cosmic Microwave Background

Finally, this chapter studies cosmological weak lensing of the CMB temperature anisotropies. First, temperature anisotropy maps have to be generated with the same statistical properties as the CMB. After a description of the used scheme and a resolution study of these maps, the phenomenon of cosmic variance, having been encountered several times during the previous chapters, shall be described. The last chapter is dedicated to the actual lensing studies of the CMB: After the probability distribution approach, the skewness as an indicator of induced non–Gaussianity in the CMB maps by lensing is presented.

7.1 Generating CMB Temperature Anisotropies

It is commonly assumed that the CMB anisotropies originate from primordial density perturbations. This hypothesis is strongly supported by theories like inflation (Guth (1981) and Albrecht & Steinhardt (1982)), which predict that these perturbations originate from quantum vacuum fluctuations in the early Universe and by direct observations of the CMB (sections 2.2 and 2.4).

Furthermore, one assumes the CMB anisotropies to be a particular realization of a Gaussian random field. This is based on the fact that processes like quantum fluctuations leading to primordial density perturbation took place in causally unconnected regions. Postulating that the involved physical processes in different regions are of the same nature, respectively, and using the central limit theorem predicts the CMB anisotropies to be a Gaussian random field.

7.1.1 Structure of the Generating Mechanism

Realization of Gaussian Random Fields In order to simulate Gaussian random fields, we follow the ideas described in Press et al. (1992). Considering the fundamental transformation law of probabilities,

$$p(y)\,|\mathrm{d}y| = p(x)\,|\mathrm{d}x|\,, \tag{7.1}$$

we can define the function $y(x) = \sqrt{(-2)\log(x)}$, where $x \in (0,1)$ is a uniform deviate, determined by $p(x) = \mathrm{d}x$, $\forall x \in (0,1)$. We conclude that the quantity y is normally

Gaussian distributed according to

$$p(y)\,\mathrm{d}y = \left|\frac{\mathrm{d}x}{\mathrm{d}y}\right|\mathrm{d}y = \frac{1}{\sqrt{2\pi}}e^{-y^2/2}\mathrm{d}y\,. \tag{7.2}$$

Using equation (7.1) it can be seen that the quantity $\hat{\tau} \equiv \sigma y$ is Gaussian distributed with variance σ^2.

Power Spectrum of the CMB As already discussed in section 3.1, a Gaussian random field is fully determined by its mean μ and its variance σ^2. Taking the Fourier transform of the relative temperature fluctuations $\hat{\tau}$ to be the independent random field,

$$\tau(\vec{\theta}\,) \equiv \frac{T(\vec{\theta}\,) - \langle T\rangle}{\langle T\rangle} \tag{7.3}$$

$$\text{and} \qquad \hat{\tau}(\vec{\ell}\,) = \int\limits_{\mathbb{R}^2} \mathrm{d}^2\theta\,\tau(\vec{\theta})e^{\mathrm{i}\vec{\theta}\cdot\vec{\ell}}\,,$$

then the mean of $\hat{\tau}$ vanishes by definition. Defining furthermore the power spectrum of the temperature anisotropies in the flat–sky approximation

$$\left\langle \hat{\tau}(\vec{\ell}\,)\hat{\tau}^*(\vec{\ell}\,')\right\rangle \equiv (2\pi)^2\delta_D(\vec{\ell} - \vec{\ell}\,')P_T(|\vec{\ell}\,|)\,, \tag{7.4}$$

we deduce that the variance of the relative temperature fluctuations in Fourier space is given by the power spectrum,

$$\sigma_T^2(\ell) \equiv \left\langle \left|\hat{\tau}(\vec{\ell}\,)\right|^2\right\rangle = P_T(\ell)\,. \tag{7.5}$$

In particular, the simulation of the CMB temperature fluctuations consists of the following three parts:

1. The angular power spectrum C_ℓ is computed for the flat ΛCDM Universe using the `CMBfast` code of Seljak & Zaldarriaga (1996). In the flat–sky approximation, the angular power spectrum equals the flat one, $C_\ell = P(\ell)$ for $\ell \gg 1$ (see section 3.3).

2. Then Gaussian random variables are generated on a complex two–dimensional grid in Fourier space with variance $\sigma^2(\ell) = P_T(\ell)$ according to the absolute value of their wave vectors $\vec{\ell}$. The exact value of the power spectrum $P_T(\ell)$, is linearly interpolated from the discrete multipole moments ℓ of the angular power spectrum C_ℓ.

3. Finally, the field $\hat{\tau}(\vec{\ell}\,)$ is Fourier transformed onto the tangential plane to the sky yielding the pure real temperature anisotropies $\tau(\vec{\theta})$.

The procedure is illustrated by the following flow chart:

$$C_\ell \xrightarrow{\ell\gg 1} P_T(\ell) \longrightarrow \hat{\tau}(\vec{\ell}\,) \xrightarrow{\mathcal{F}^{-1}} \tau(\vec{\theta}) \tag{7.6}$$

7.1.2 Visualization of the CMB

The following figure shows a particular realization of a CMB temperature anisotropy field $\tau(\vec{\theta})$ of angular size $\theta = 5^\circ$ being taken from a larger realization. The colors are coded such, that the brightest yellow corresponds to the highest present positive value of the temperature fluctuations, and the darkest blue corresponds to the most negative value of τ.

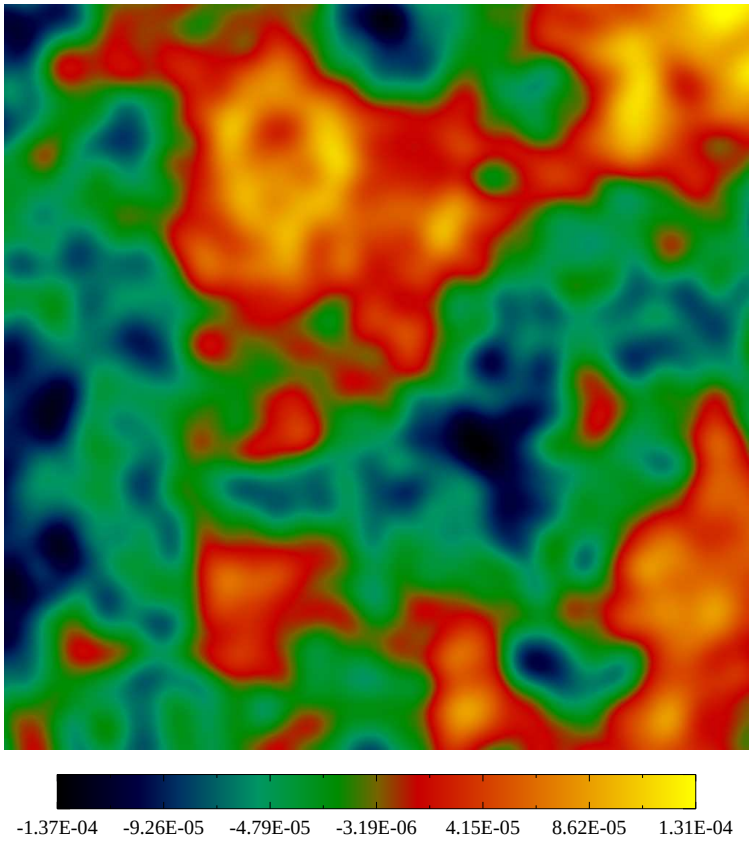

Figure 7.1: Particular realization of an CMB temperature anisotropy field $\tau(\vec{\theta})$ of angular size $\theta = 5^\circ$.

7.1.3 Resolution Studies

The `CMBfast` code provides only values of the angular power spectrum C_ℓ up to $\ell = 3000$, because the CMB is exponentially damped on these scales due to Silk damping (see section 2.2.2). In order to simulate the temperature fluctuations $\hat{\tau}(\vec{\ell})$ on the two–dimensional grid in Fourier space, one has to adjust the maximum physical wave vector, up to which the Gaussian random field needs to be generated. The absolute

value of this maximal wave vector is given by the Nyquist frequency,

$$\ell_N = \frac{2\pi}{\Delta\theta} = \frac{2\pi n}{\theta_{\text{side}}}\,, \tag{7.7}$$

where $\Delta\theta$ denotes the grid separation in angular space, n is the number of grid points on a side and θ_{side} is consequently the side length of the flat tangential plane in angular space. This equation represents the uncertainty relation in Fourier space. Given a fixed number of grid points $N = n^2$, a small Nyquist frequency ℓ_N coming along with a good resolution in Fourier space corresponds to large angular fields combined with bad resolution in angular space and vice versa. Therefore, in order to obtain a good sampling of the given angular power spectrum C_ℓ by `CMBfast`, the Nyquist frequency ℓ_N should not exceed the maximum multipole moment by more than a factor of a few.

Probability Distribution Function Considering first the probability distribution function of the CMB temperature fluctuations PDF_τ, we can check the temperature fields for the required Gaussianity. Figure 7.2 shows such a probability distribution function (solid line) compared to a Gaussian (dashed line) with the same mean and variance yet without considering lensing effects. They are both normalized to unity.

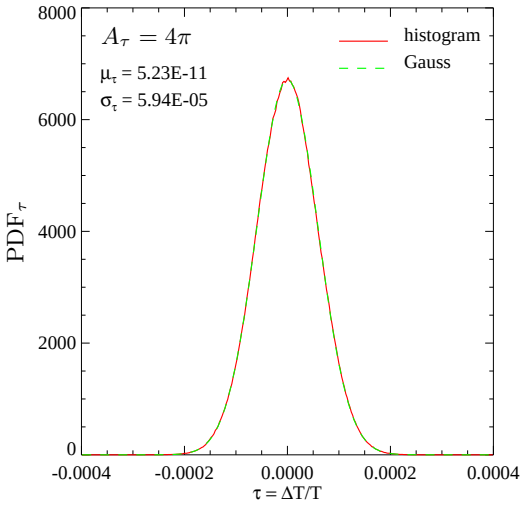

Figure 7.2: Probability distribution function (PDF) of the CMB temperature fluctuations $\tau(\vec{\theta})$ at the last scattering surface without considering lensing effects. PDF_τ (solid line) with size comparable to the area of the sky is compared to a Gaussian with the same mean and variance (dashed line).

Figure 7.2 shows the PDF_τ of an angular field with size comparable to the area of the whole sky. This huge field could be interpreted as a tiling of smaller sub patches each representing tangential planes on the sky. In order to obtain an angular field of this

size, the temperature fluctuations τ have been simulated using the Nyquist frequency $\ell_N = 3630$ on a 2048^2–point grid. This implies perfect sampling in Fourier space and results in an excellent Gaussian distribution of τ.

Power Spectrum Taking into account the power spectrum of $\tau(\vec{\theta})$ is even more instructive for resolution studies. The simulation of the CMB temperature fluctuations on a field of size comparable to the area of the sky, $\tau_{\mathrm{sky}}(\vec{\theta})$, proceeds according to the technique described in section 7.1.1. For obtaining smaller fields because of the finite size of our lensing field, smaller patches are obtained by successively subdividing the field of large angular size into smaller parts, $\tau_{\mathrm{w}}(\vec{\theta})$. However, before transforming them back into Fourier space, they have to be made periodic, because the fast–Fourier transform technique intrinsically assumes periodic boundary conditions. Since the small temperature fluctuation fields do not have periodic boundary conditions, in principle, there are several techniques how to deal with this problem: (i) One could use the method of zero padding the small fields with fields identically zero representing an aperture. Unfortunately, zero padding the temperature fluctuations before fast Fourier transforming them mathematically corresponds to a multiplication with a two–dimensional Heaviside function in angular space, $H(\vec{\theta}_{\mathrm{side}} - \vec{\theta})$, for $\vec{\theta} > 0$, where $\vec{\theta}_{\mathrm{side}}$ denotes the length of the angular field. In Fourier space, this yields a convolution with the Fourier transform of the Heaviside function,

$$\begin{aligned}
\mathcal{F}\left[H\left(\vec{\theta}+\frac{\vec{\theta}_{\mathrm{side}}}{2}\right)\cdot H\left(\frac{\vec{\theta}_{\mathrm{side}}}{2}-\vec{\theta}\right)\cdot\tau(\vec{\theta})\right] = \\
&= 4\int_{\mathbb{R}^2}\mathrm{d}^2l'\,\hat{\tau}(\vec{\ell}-\vec{\ell}')\frac{\sin\left(\ell_1\frac{\theta_{\mathrm{side}}}{2}\right)}{\ell_1}\frac{\sin\left(\ell_2\frac{\theta_{\mathrm{side}}}{2}\right)}{\ell_2} \\
&= \theta_{\mathrm{side}}^2\int_{\mathbb{R}^2}\mathrm{d}^2l'\,\hat{\tau}(\vec{\ell}-\vec{\ell}')j_0\left(\ell_1\frac{\theta_{\mathrm{side}}}{2}\right)j_0\left(\ell_2\frac{\theta_{\mathrm{side}}}{2}\right), \qquad (7.8)
\end{aligned}$$

where $j_0(x)$ is the spherical Bessel function of the first kind. This effect is of minor importance for large angular fields θ_{side}, but has large impact on small fields which are preferred because our lensing field is finite. So we decided to adopt another method, (ii), which consists of making the angular field periodic in both angular directions by reflecting the original field around two adjacent borders as well as reflecting the field at the intercept point. This leads to the temperature fluctuation field $\tau'_{\mathrm{w}}(\vec{\theta})$ with periodic boundary conditions,

$$\tau'_{\mathrm{w}}(\vec{\theta}) = \tau'_{\mathrm{w}}(\vec{\theta}+\vec{\theta}_{\mathrm{side}})\,. \qquad (7.9)$$

Applying the usual procedure using equation 7.4, the power spectrum of the temperature anisotropies $P_T(\ell)$ can be recovered and compared to the original one. The

following commuting diagram illustrates this procedure:

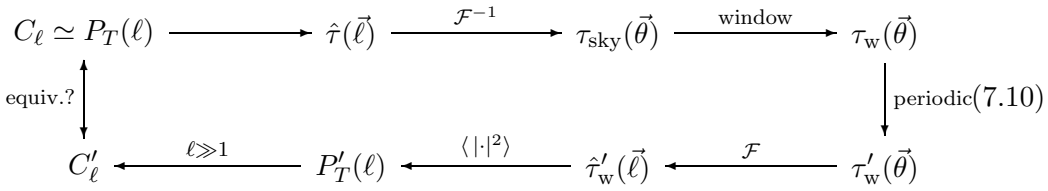

Figure 7.3 shows a resolution study of the recovered angular power spectrum C_ℓ.

The upper left panel in figure 7.3 shows the excellent recovery of the angular power spectrum from a full sky map. Because of the small size of our lensing fields ($\theta_{\rm side} \sim 5^\circ$) we have to aim at small CMB temperature fluctuation fields. This can be achieved by successively subdividing the large CMB fields into smaller parts with worse resolution in angular space, however. We split up the large field of angular size comparable to the whole sky into equally sized smaller parts and measured $C_\ell(\ell)$ on these maps. Due to the smaller number of large scale modes of temperature fluctuations in these smaller fields, this leads to larger statistical scatter in the power spectrum. This effect can also be seen as missing modes in the lower two panels at large angular scales due to the small number of grid points.

The best way out of this problem would clearly be the consideration of all sky maps of CMB anisotropies from where C_ℓ can be perfectly recovered. In return, this would require spherical light cone simulations of structure formation. Concluding, it is very difficult with this method of generating the CMB anisotropies to simulate small $\tau(\vec{\theta})$ fields with sufficiently high statistical information of global properties like the power spectrum.

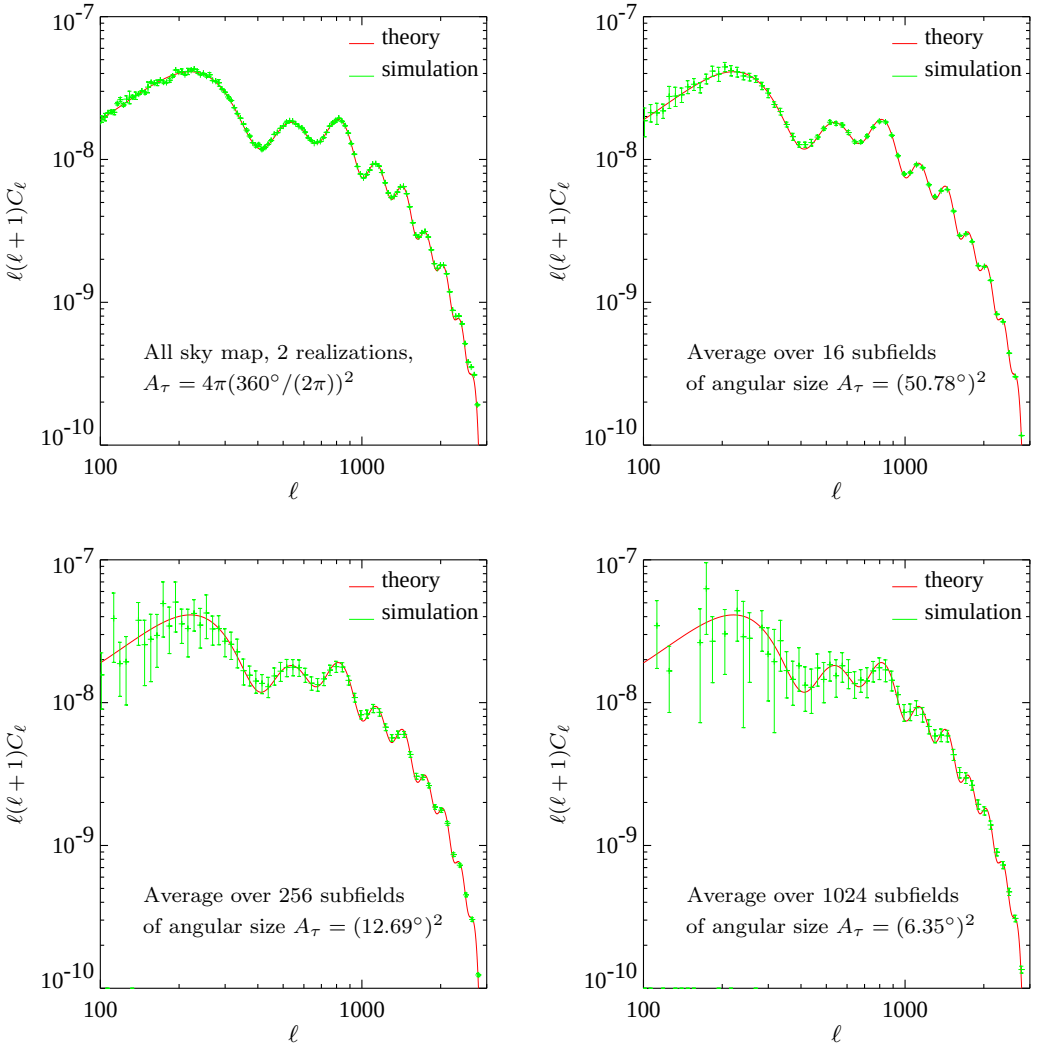

Figure 7.3: Resolution study of the recovered angular power spectrum C_ℓ. The upper left panel shows C_ℓ recovered from an all sky map (1σ–error bars drawn from a second independent realization). Successively subdividing the large field into smaller parts, measuring C_ℓ and subsequently averaging leads to the green graphs in the other panels. The error bars show the standard deviation of the number of subpatches in which the large field was divided.

7.1.4 Cosmic Variance

Looking more closely at the previous graphs, we see larger error bars on larger angular scales which are due to *cosmic variance*. The influence of this effect shall be calculated in this subsection. All averages represent ensemble averages over a large number of different all–sky realizations. The variance of the angular power spectrum is defined by

$$\sigma^2_{C_\ell} = \left\langle (C_\ell - \langle C_\ell \rangle)^2 \right\rangle = \langle C_\ell^2 \rangle - \bar{C}_\ell^2 \,, \tag{7.11}$$

$$\text{where} \qquad \bar{C}_\ell \equiv \langle C_\ell \rangle = \left\langle \sum_{m=-\ell}^{\ell} |a_{\ell m}|^2 \right\rangle .$$

The first term of equation (7.11) can be rewritten as

$$\begin{aligned} \langle C_\ell^2 \rangle &= \left\langle \left(\frac{1}{2\ell+1} \sum_{m=-\ell}^{\ell} |a_{\ell m}|^2 \right)^2 \right\rangle \\ &= \bar{C}_\ell^2 \left\langle \left(\frac{1}{2\ell+1} \sum_{m=-\ell}^{\ell} g_m^2 \right)^2 \right\rangle , \end{aligned} \tag{7.12}$$

where g_m is normal Gaussian distributed, with vanishing mean, $\langle g_m \rangle = 0$ and unit variance, $\langle g_m^2 \rangle = \sigma^2_{g_m} = 1$. This term can be further simplified,

$$\begin{aligned} \langle C_\ell^2 \rangle &= \bar{C}_\ell^2 \left\langle \frac{1}{(2\ell+1)^2} \left(\sum_m g_m^4 + \sum_{\substack{m,m' \\ m' \neq m}} g_m^2 g_{m'}^2 \right) \right\rangle \\ &= \bar{C}_\ell^2 \frac{1}{(2\ell+1)^2} \left[(2\ell+1)\langle g_m^4 \rangle + (2\ell+1)2\ell \langle g_m^2 \rangle^2 \right] \\ &= \bar{C}_\ell^2 \frac{1}{2\ell+1} (3+2\ell) \,, \end{aligned} \tag{7.13}$$

where the relation $\langle g_m^4 \rangle = 3\langle g_m^2 \rangle^2$ for $\langle g_m \rangle = 0$ has been used in the first step. Thus, the cosmic variance can be expressed in terms of the average angular power spectrum $\bar{C}_\ell$ and the multipole moments,

$$\sigma^2_{C_\ell} = \langle C_\ell^2 \rangle - \bar{C}_\ell^2 = \frac{2\bar{C}_\ell^2}{2\ell+1} \,. \tag{7.14}$$

The cosmic variance is a purely statistical effect, which is larger for smaller multipole moments ℓ and larger values of the average angular power spectrum due to the limited number of long–wavelength modes in the sky on these large scales.

As instructive example, the corresponding value for the angular power spectrum at the multipole of the first Doppler peak, $\ell \sim 200$, is of the order $C_\ell \sim 10^{-12}$. Thus, we expect a cosmic variance of $\sigma_{C_\ell} \sim 7 \cdot 10^{-14}$ on these scales which agrees well with the measured standard deviation of $\sigma_{C_\ell,\mathrm{sim}} \sim 8 \cdot 10^{-14}$ from the second realization of the full sky map indicating no systematic uncertainties.

7.2 Lensing the CMB Temperature Anisotropies

7.2.1 Visualization of the Lensing Effect on the CMB

Finally, the lensing displacement, as computed and studied in chapter 6 has been applied to the CMB temperature fluctuations. In other words, the intrinsic temperature of the CMB at the position of the surface of last scattering $\vec{\beta}$ has been related to the lensed angular position $\vec{\theta}$ on the sky, where it is observed,

$$T_{\rm obs}(\theta) = T_{\rm int}(\vec{\beta}) = T_{\rm int}(\vec{\theta} - \vec{\alpha})\,. \tag{7.15}$$

The lensing displacement has been modeled according to section 6.1, by propagating a regular two–dimensional grid of photons along the past light cone to the surface of last scattering. There, the intrinsic CMB fluctuations $\tau_{\rm int}$ have been linearly interpolated onto the distorted photon positions ($\vec{\beta}$) which corresponds to fluctuations of the regular grid on the sky $\tau_{\rm obs}(\theta)$ for the observer, according to equation (7.15). The upper two panels of figure 7.4 show the comparison of a particular realization of a CMB temperature anisotropy field between $\tau_{\rm int}$ and $\tau_{\rm obs}$. The unlensed CMB field $\tau_{\rm int}$ has also been interpolated onto the regular lensing grid on the sky for a better comparison. There can hardly be seen any difference.

7.2.2 Probability Distribution

The lower two panels of figure 7.4 study the pure lensing effect on the CMB temperature anisotropies by means of the difference between lensed observed and the unlensed intrinsic CMB, $\delta\tau = \tau_{\rm obs} - \tau_{\rm int}$. The original structure of the CMB fluctuations has been subtracted such that we are left with the lensing contribution. This is also supported by the probability distribution function $\mathrm{PDF}_{\delta\tau}$, being displayed in the right panel, whose standard deviation is roughly one order of magnitude smaller than that of PDF_{τ}. This is an indication of the small effect of lensing on the CMB anisotropies which will be studied more thoroughly in the following section.

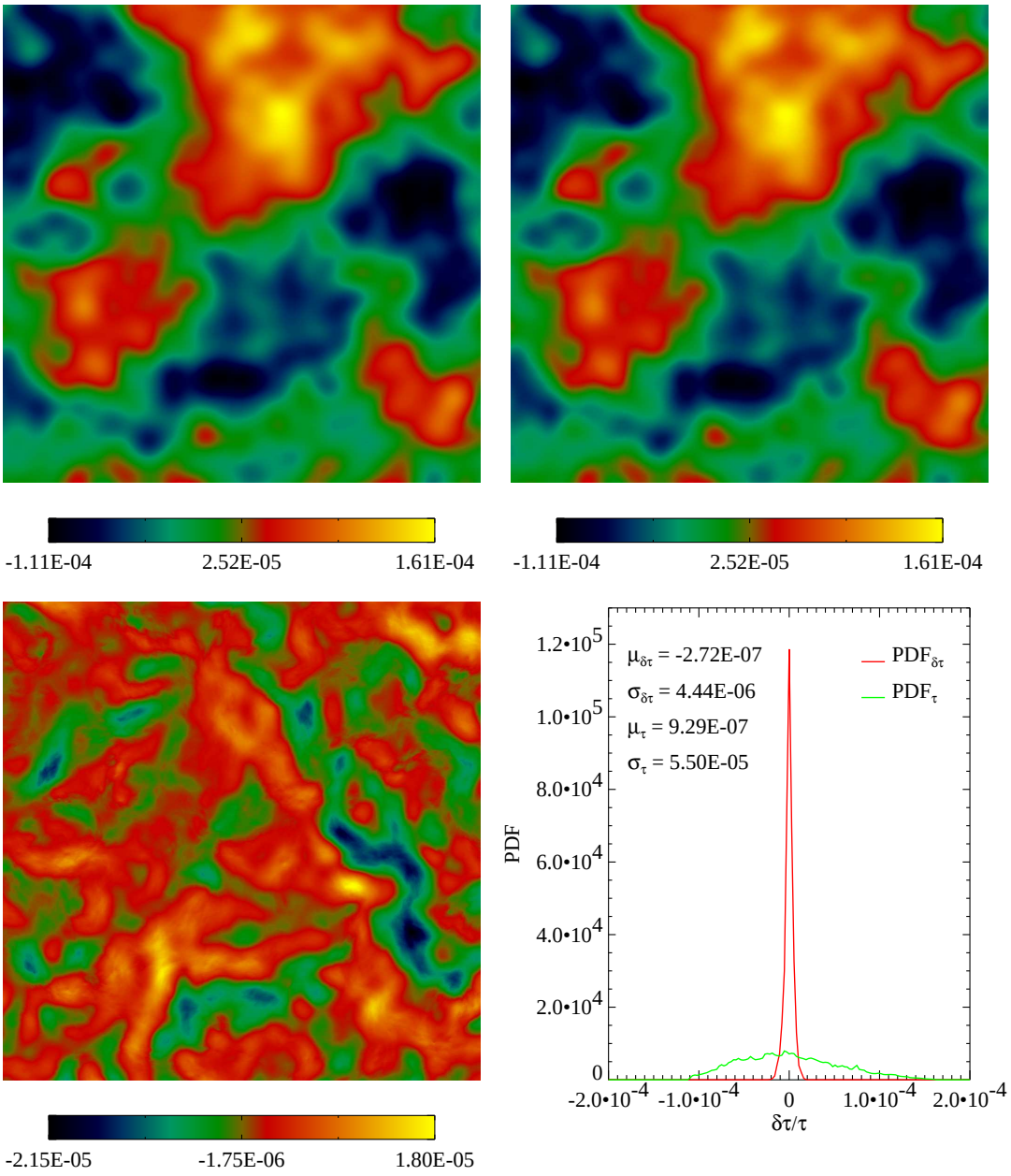

Figure 7.4: Study of the lensing effect on a particular realization of an CMB temperature anisotropy field $\tau(\vec{\theta})$ of angular size $\theta \simeq 4.27°$. *Upper left panel*: Unlensed CMB field $\tau_{\rm int}$ at intrinsic position at the surface of last scattering. *Upper right panel*: Lensed CMB field $\tau_{\rm obs}$ at the image position on the sky. *Lower left panel*: Difference between lensed and unlensed CMB, $\delta\tau = \tau_{\rm obs} - \tau_{\rm int}$ with same angular size. *Lower right panel*: Comparison of the probability distribution functions $\mathrm{PDF}_{\delta\tau}$ (red) and PDF_{τ} (green) of this individual realization.

7.2.3 Skewness as Indicator of Non–Gaussianity

In contrast to the power spectrum, which measures the global statistical properties of random fields because it involves the Fourier transform, there are other local methods for detecting present non–Gaussianity in the lensed CMB maps. The skewness or third moment S_3 in real space is one way to compress the information of non–Gaussianity into a single number on a given scale. The skewness characterizes the degree of asymmetry of a distribution around its mean and is defined to be the appropriately weighted, centered third moment μ_3 of a probability distribution $p(\tau)$,

$$S_3 \equiv \frac{\mu_3}{\mu_2^{3/2}} = \frac{\mu_3}{\sigma^3} = \frac{1}{N}\sum_{i=1}^{N}\left(\frac{\tau_i - \mu}{\sigma}\right)^3 , \tag{7.16}$$

where μ is the mean of the distribution, σ its standard deviation and N is the number of different realizations times the number of pixels within one temperature map. This definition guarantees the skewness to be a dimensionless quantity. It can be shown that all odd moments of a Gaussian distribution vanish. Thus, a non–zero value of the skewness indicates non–Gaussianity in the distribution. A positive value of skewness indicates an asymmetric tail extending out towards positive values τ, and a negative value signifies the opposite.

Figure 7.5 compares the skewness S_3 as measured in lensed and unlensed CMB temperature anisotropy fields of angular size $\theta = 5^\circ$. The skewness as measured in individual CMB maps (displayed in the left panel of figure 7.5) shows large scatter around zero. This is not surprising because that statistical quantity measures the deviation of the functional shape of the distribution from a Gaussian which is large for an individual noisy realization of a Gaussian random field. However, the cumulative skewness of the single realizations levels out with increasing number of realizations (right panel in figure 7.5).

There can hardly be seen any difference between the lensed and unlensed CMB fluctuation fields. For explaining this, one has to return to studies of non–Gaussianity in the effective convergence fields κ_{eff} in section 6.3.2. Already in the statistics of the convergence are weaker non–Gaussian effects visible for increasing source redshifts. Concentrating now on the statistics of the deflection angle $\vec{\alpha}$, which is responsible for the lensing of the CMB temperature anisotropies, shows even weaker effects of non–Gaussianity for the following reason: The power spectra of the effective convergence and the deflection angle are related by equation (4.53), namely

$$P_{\vec{\alpha}}(\ell) = \frac{4}{\ell^2} P_\kappa(\ell) \,. \tag{7.17}$$

This shows that the power spectrum of the deflection angle is weighted by a factor of ℓ^{-2} compared that of the convergence, enhancing the large angular scales which are related to large scale structures. Thus, small scales are suppressed in the statistics of the lensing deflection angle. However, only these scales gave rise to non–linear effects in the course of the density evolution of the Universe being responsible for non–Gaussian statistical features. This shows that non–linear density evolution is

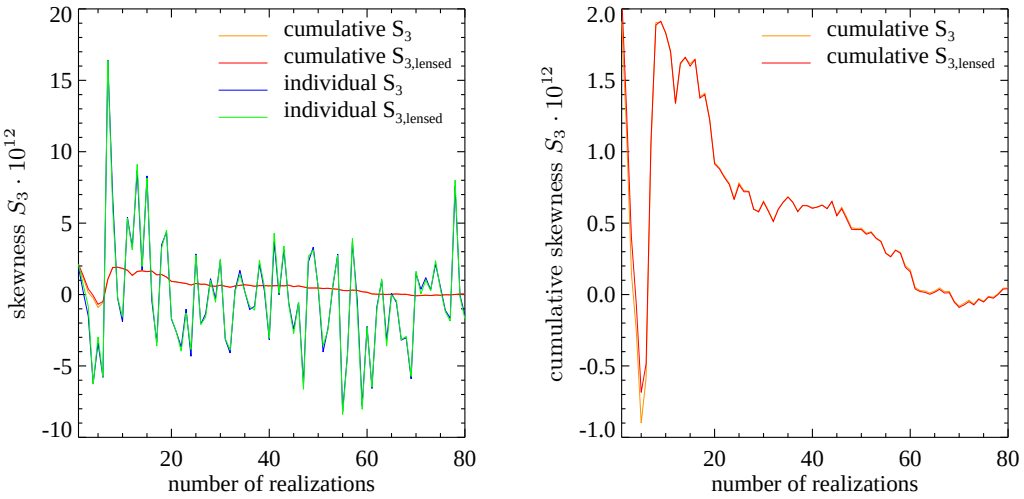

Figure 7.5: Comparison of skewness S_3 in lensed and unlensed CMB temperature anisotropy fields of angular size $\theta = 5°$. *Left panel*: Skewness as measured in individual CMB maps (green for lensed and blue for unlensed) compared to the cumulative skewness in these maps (red for lensed and orange for unlensed) as a function realizations. *Right panel*: Only the cumulative skewness is displayed for a better comparison of the lensed (red) and unlensed (orange) CMB maps.

---

much less important for lensing statistics of the CMB than it is for the convergence or the shear. For further investigations, measuring the skewness within an aperture would be a possibility of detecting any present non–Gaussianity.

7.3 Concluding Remarks

Because the different results were already discussed in the course of this work, only the final main conclusions shall be mentioned here:

1. The N–body simulations as underlying density field were well designed for realistic lensing studies by ray tracing methods. For high source redshifts of $z_s \sim 5$, the studies are reliable on scales of $10^2 \lesssim \ell \lesssim 8 \cdot 10^3$ (cf. section 6.3.3).

2. However, for studying lensing of the CMB temperature anisotropies in form of induced non–Gaussian signals or the like, the kind of simulations carried out in this work faces two severe problems of principle: (i) Taking cosmological N–body simulations in large boxes of $\sim 0.5\,h^{-1}$ Gpc imposes automatically an upper limit to the size of the light cone. Considering the surface of last scattering as source leads to the small–angle approximation with angular size of $\sim 5°$ and generating CMB maps of such an angular size causes a low resolution either in Fourier space

or in angular space. The only way to avoid this problem would be the consideration of all sky maps of CMB anisotropies, however, requiring spherical light cone simulations of structure formation in order to studying lensing properties. Using the chosen method of generating the CMB anisotropies to simulate small $\tau(\vec{\theta})$ fields significantly restricts statistical information of global properties as the power spectrum. (ii) Moreover, concentrating on deflection angle statistics by studying lensing properties of the CMB, one has to accept the suppression of existing non–Gaussian effects on small scales compared to statistics of the convergence or the shear. Thus, even with spherical light cone simulations of density evolution it will be very difficult to detect lensing effects with the deflection angle approach.

7.4 Further Perspective

Taking the encouraging results of figure 7.3 as basis, there still exists a possibility of detecting weak lensing signatures in the power spectrum $P_T(\ell)$. Due to the limited time frame of this diploma thesis, further investigations could not be carried out within this thesis. However, it is definitely worthwhile to proceed in this direction. A careful analysis is yet needed for these lensing studies of the CMB fluctuations because typical scales of lensing are comparable to the grid size of the temperature anisotropies. The task consists of detecting the pure lensing features while not picking up numerical effects of the interpolation routine. Another promising potentiality of detecting lensing in the CMB would be measurements of the skewness in apertures in lensed and unlensed maps. Pure skewness measurements as representatives of 1–point statistics show no effect of lensing because of conservation of surface brightness through lensing (shown in figure 7.5).

A Conventions and Nomenclature

The sign conventions for the formulae of General Relativity are chosen in agreement with the textbook of Landau & Lifshitz (1997). This implies the particular choice of signature $(+---)$, where the zeroth component refers to the time. General Relativity describes space–time as a four–dimensional manifold whose metric tensor $g_{\alpha\beta}$ is a dynamical field. Two events in space–time with coordinates differing by $\mathrm{d}x^\alpha$ are separated by $\mathrm{d}s$, with $\mathrm{d}s^2 = g_{\alpha\beta}\,\mathrm{d}x^\alpha \mathrm{d}x^\beta$, assuming Einstein's summation convention. The *eigentime* (proper time) of an observer traveling by $\mathrm{d}s$ changes by $c^{-1}\mathrm{d}s$. Greek indices $\alpha, \beta, \mu, \nu, \ldots$ are space–time indices running over $0 \ldots 3$. The corresponding Latin indices $a, b, m, n, \ldots$ label the spatial components $1, 2, 3$. The sign convention for the Riemann tensor is $R^\alpha{}_{\mu\beta\nu} \equiv \Gamma^\alpha_{\mu\nu,\beta} - \Gamma^\alpha_{\mu\beta,\nu} + \Gamma^\rho_{\mu\nu}\Gamma^\alpha_{\rho\beta} - \Gamma^\rho_{\mu\beta}\Gamma^\alpha_{\rho\nu}$ and the Ricci tensor is obtained by contracting the first and third index, $R_{\mu\nu} = R^\alpha{}_{\mu\alpha\nu}$. Space–time covariant derivatives are written with semicolons, e.g. $g_{\mu\nu;\alpha} = 0$, whereas partial derivatives are denoted by a single comma. In the following, the main abbreviations and notations used for various cosmological variables, statistics, and gravitational lensing are listed. They are by no means complete, but should be nevertheless useful as a quick reference.

Table 1: **Abbreviations**

BBN	big–bang nucleosynthesis
CMB	comic microwave background
CDM	cold dark matter (model)
WDM	warm dark matter (model)
HDM	hot dark matter (model)
ΛCDM	flat CDM model with a cosmological constant
PDF	probability distribution function
SNeIa	supernovae type Ia
AP^3M	adaptive particle–particle/particle–mesh technique in numerical simulations
COBE	Cosmic Background Explorer (satellite mission)
DMR	Differential Microwave Radiometers onboard COBE
MAXIMA	Millimeter Anisotropy Experiment Imaging Array (balloon–borne telescope)
BOOMERANG	Balloon Observations of Millimetric Extragalactic Radiation and Geophysics
MAP	Microwave Anisotropy Probe (satellite mission)
PLANCK	CMB anisotropy satellite (in honor of Max Planck)
ROSAT	X-ray satellite (in honor of Wilhelm Konrad Röntgen)

Table 2: **Notation for Cosmological Variables**

w	radial distance in the Robertson–Walker metric, identically to the comoving distance $D_{\rm com}$
a	cosmic scale factor, normalized to unity at the present epoch
z	cosmic redshift parameter, $z = a^{-1} - 1$
K	spatial curvature parameter
$f_K(w)$	curvature function defined in equation (2.2)
Λ	cosmological constant
Ω_m	total matter density ρ_m in units of the critical density $\rho_{\rm cr}$ today
Ω_b	baryonic matter density in units of the critical density $\rho_{\rm cr}$ today
Ω_Λ	cosmological constant Λ in units of the critical density $\rho_{\rm cr}$ today
Ω_r	radiation density ρ_r in units of the critical density $\rho_{\rm cr}$ today
$\Omega_{\rm tot}$	total energy density in the Universe in units of the critical density today, $\Omega_{\rm tot} \equiv \Omega_r + \Omega_m + \Omega_\Lambda$
$H(a)$	Hubble function, determined by Friedmann's equation $H(a) = \dot{a}/a$
h	Hubble constant at the present time, in units of $100\,\mathrm{km\,s^{-1}\,Mpc^{-1}}$, $H_0 = 100\,h\,\mathrm{km\,s^{-1}\,Mpc^{-1}}$
ω_f	parameterization of the equation of state of a particular cosmological fluid component, $\omega_f = p/(\rho c^2)$
q_0	cosmic deceleration parameter at the present time, $q_0 \equiv -H_0^{-2}(\ddot{a}/a)_0$
$\tau(\vec{\theta})$	relative temperature fluctuations of the CMB, $\tau(\vec{\theta}) = [T(\vec{\theta}) - \langle T\rangle]/\langle T\rangle$
$\vec{x}$	three–dimensional comoving position vector on spatial hyper–surface
$\delta(\vec{x}, a)$	density contrast of cold dark matter perturbations, $\delta(\vec{x}, a) = [\rho(\vec{x}, a) - \bar{\rho}(a)]/\bar{\rho}(a)$
δ_0	density contrast linearly extrapolated to the present epoch
$g(a)$	cosmological growth function, normalized to unity at the present epoch, $\delta(a) = \delta_0 a g(a)$
$G_+(a)$	effective growth function, $G_+(a) = a g(a)$
$d_H(a)$	comoving horizon, $d_H(a) = c\,a^{-1}H^{-1}(a)$
$\vec{k}$	three–dimensional wave vector in Fourier space, Fourier conjugate to $\vec{x}$
$\hat{\delta}(\vec{k}, a)$	Fourier transform of the density contrast $\delta(\vec{x}, a)$, $\hat{\delta}(\vec{k}, a) = \int \mathrm{d}^3x\, \delta(\vec{x}, a) e^{\mathrm{i}\vec{x}\cdot\vec{k}}$
$T(\vec{k}, a)$	linear transfer function for adiabatic perturbations
$P_i(k)$	initial Harrison–Zel'dovich power spectrum
n_s	spectral tilt of primordial density perturbations, $P_i(k) \propto k^{n_s}$

Table 3: **Notation for Statistical Quantities**

$g(\vec{x})$	statistically homogeneous and isotropic random field $g(\vec{x})$ with vanishing expectation value, $g \equiv \{\delta, \tau\}$
$\xi_{gg}(\|\vec{y}\|)$	autocorrelation function, $\xi_{gg}(\|\vec{y}\|) = \langle g(\vec{x}) g^*(\vec{x}+\vec{y}) \rangle$
$P_\delta(k)$	three–dimensional density power spectrum, Fourier transform of the autocorrelation function
$\vec{\ell}$	two–dimensional wave vector in Fourier space, Fourier conjugate to $\vec{\theta}$ on the tangential plane to the sky
$P_T(\|\vec{\ell}\|)$	two–dimensional power spectrum of the CMB temperature anisotropies in the flat–sky approximation
ℓ	multipole order of spherical harmonics
$a_{\ell m}$	expansion coefficients of the CMB temperature fluctuations
C_ℓ	angular power spectrum of the CMB temperature anisotropies as a function of multipole ℓ

Table 4: **Notation for Lensing Quantities**

Φ	three–dimensional Newtonian potential
Ψ	two–dimensional lensing potential; suitably scaled and projected Newtonian potential
D_l	angular diameter distance between lens and observer
D_s	angular diameter distance between source and observer
D_{ls}	angular diameter distance between source and lens
$\vec{\beta}$	intrinsic angular source position
$\vec{\theta}$	observed image position on the sky
$\vec{\hat{\alpha}}$	lensing deflection angle
$\vec{\alpha}$	reduced lensing deflection angle, $\vec{\alpha}(\vec{\theta}) = \vec{\hat{\alpha}}(\vec{\theta}) D_{ls}/D_s$
$\vec{\xi}$	two–dimensional impact parameter in physical units
$\vec{x}$	comoving two–dimensional impact parameter $\vec{x} = \vec{\xi}/a$
$\Sigma(\vec{\xi})$	surface mass density on lens plane
$\Sigma_{\rm cr}$	critical surface mass density
$\mathcal{A}$	Jacobian matrix of the mapping from the source plane to the image plane
$\mathcal{M}$	magnification tensor, $\mathcal{M} = \mathcal{A}^{-1}$
κ	lensing convergence, $\kappa = \Sigma/\Sigma_{\rm cr}$
γ	lensing shear, $\gamma = \sqrt{\gamma_1^2 + \gamma_2^2}$
$\kappa_{\rm eff}$	effective convergence in cosmological weak lensing
$P_\kappa(\ell)$	effective convergence power spectrum
$P_\gamma(\ell)$	cosmic shear power spectrum, $P_\gamma(\ell) = P_\kappa(\ell)$
$P_{\vec{\alpha}}(\ell)$	power spectrum of the lensing deflection angle

B Consistency Checks

Because the ray tracing code represents an important part of the numerical work done for this thesis, its performance and the property of being inherently self–consistent were checked in numerous ways, the most important of which are outlined in the following.

B.1 Consistency Checks on the Ray Tracing Code

The structure of the ray tracing code was already comprehensively explained in section 6.1. The procedure involves both the computation of the position of a given photon at a particular lens plane j, $\vec{\theta}_j$, yielding its position on the source plane $\vec{\beta} \equiv \vec{\theta}_n$ and on the other hand the evolution of the Jacobian matrix, $\mathcal{A}_j$, at this position backward in time. This leads to an effective convergence κ_{eff} and shear γ_{eff} as components of the Jacobian matrix describing the mapping from the source plane to the image plane. The reduced deflection angle $\vec{\alpha}(\vec{\theta})$ can easily be obtained from the angular position of the light rays on the source plane $\vec{\beta} \equiv \vec{\theta}_n$, using the lens equation (4.15),

$$\vec{\alpha}(\vec{\theta}) = \vec{\theta} - \vec{\beta}(\vec{\theta})\,. \tag{B.1}$$

The effective convergence κ_{eff} and the deflection angle $\vec{\alpha}$ are connected by

$$\kappa_{\text{eff}}(\vec{\theta}) \equiv \frac{1}{2}\vec{\nabla}_\theta \vec{\alpha}(\vec{\theta})\,. \tag{B.2}$$

As self–consistency check, the theoretical equivalence of the effective convergence fields $\tilde{\kappa}_{\text{eff}}$ obtained by means of the divergence of the deflection angle and the effective convergence field κ_{eff} in the Jacobian matrix will now be tested. The following illustration demonstrates this connection:

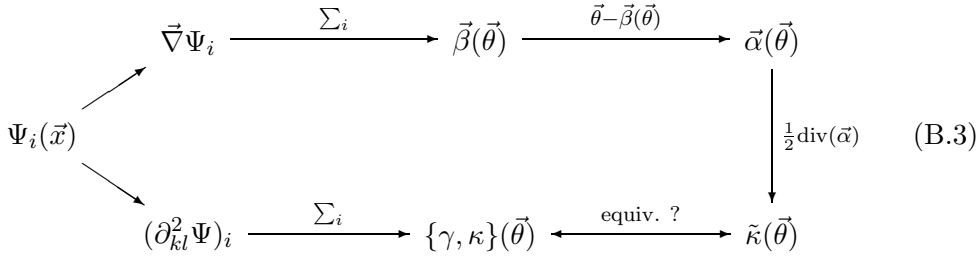

(B.3)

This section is subdivided into three parts, the first two of which compare the probability distribution function (PDF) of the difference between $\frac{1}{2}\vec{\nabla}_\theta\vec{\alpha}$ and κ for source

redshifts $z_s = 1$ and $z_s = 6.7$, respectively. The last part studies the power spectrum of this difference compared to the theoretical prediction of the convergence power spectrum.

B.1.1 Comparison of the Convergence Fields at $z_s = 1$

The following figures illustrate the comparison of the two convergence fields under consideration for source redshift $z_s = 1$: The left panel shows the effective convergence field κ_{eff}, computed by the recursion relation of the Jacobian matrix $\mathcal{A}$, whereas the right panel displays the convergence field $\tilde{\kappa}_{\text{eff}}$, obtained from the lensing deflection angle $\vec{\alpha}$ by the procedure described above. The images represent small parts of the previously shown figures 6.3 and 6.4, and the colors are rescaled such that the largest value of the present convergence in the images corresponds to the brightest color.

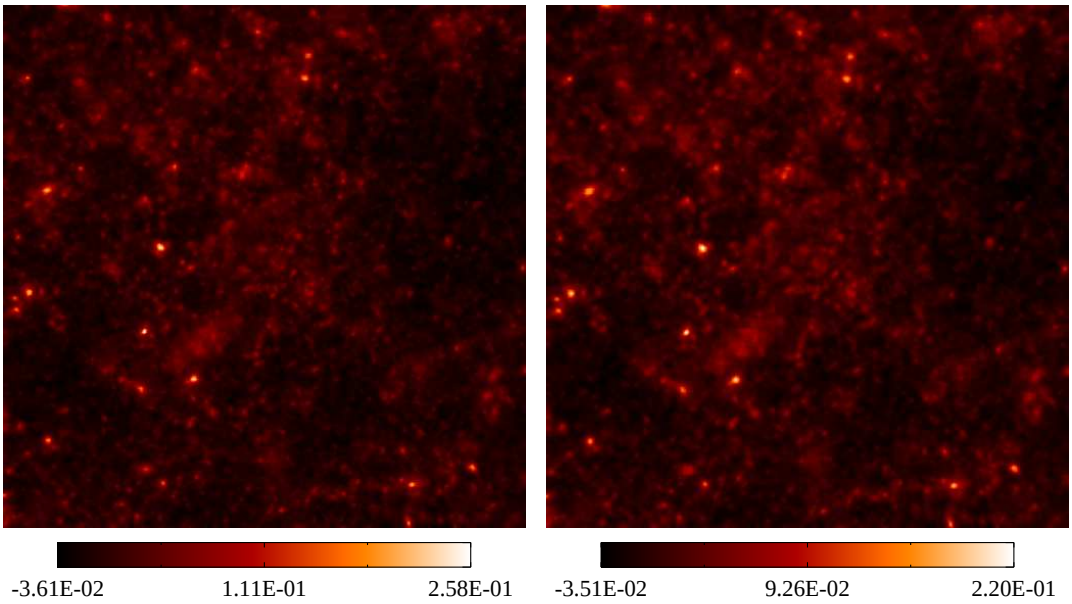

Figure B.1: Particular realization of an effective convergence field $\kappa_{\text{eff}}(\vec{\theta})$ of angular size $\theta \simeq 2.13°$ at $z_s = 1$. *Left panel*: The convergence κ_{eff} as computed from the evolution equation of the Jacobian $\mathcal{A}$. *Right panel*: The convergence $\tilde{\kappa}_{\text{eff}}$ as obtained from the lensing deflection angle $\vec{\alpha}$ as described in the text.

There can hardly be seen any difference between these two images irrespective of an overall color enhancement in the image on the right–hand side. This impression is supported by figure B.2, which shows the probability distribution function of the effective convergence field PDF_κ for source redshift $z_s = 1$, in comparison with the probability distribution of the difference of the two convergence fields, $\text{PDF}_{\Delta\kappa}$, displayed above. There is roughly one order of magnitude difference between their standard deviations, indicating a small influence of the effective resolution, already discussed in section

6.2.1. Another source of deviation of the $\mathrm{PDF}_{\Delta\kappa}$ from the theoretically expected delta distribution could be the usage of our finite difference methods.

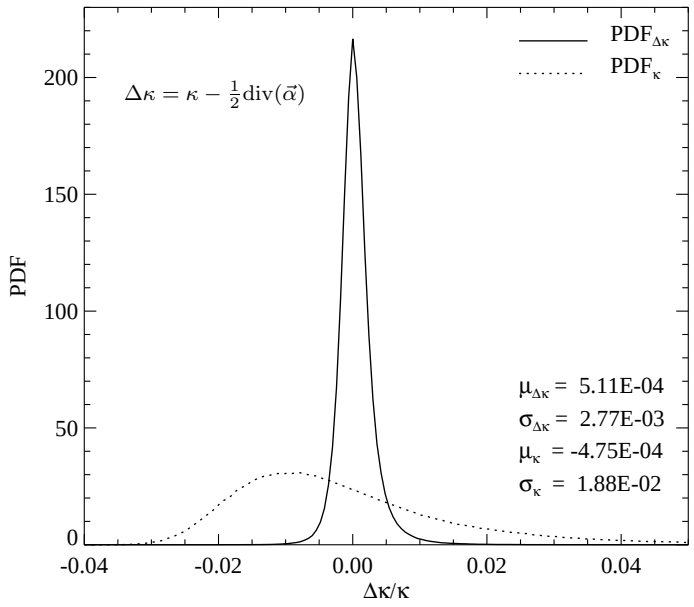

Figure B.2: Comparison of the probability distribution function of the effective convergence field, PDF_{κ}, with the probability distribution of the difference of the two convergence fields, $\mathrm{PDF}_{\Delta\kappa}$ for $z_s = 1$.

B.1.2 Comparison of the Convergence Fields at $z_s = 6.7$

This section resembles the previous one with the only difference that the simulations now assume a source redshift of $z_s = 6.7$ rather than unity. As before, the left panel of figure B.3 shows the effective convergence field κ_{eff}, computed by the recursion relation of the Jacobian matrix $\mathcal{A}$, whereas the right panel displays the convergence field $\tilde{\kappa}_{\mathrm{eff}}$, obtained from the lensing deflection angle $\vec{\alpha}$ by the procedure described above.

Figure B.4 shows the probability distribution function of the effective convergence field, PDF_{κ}, at source redshift $z_s = 6.7$, in comparison with the probability distribution of the difference of the two convergence fields, $\mathrm{PDF}_{\Delta\kappa}$. Compared to the previous case, the difference of the two convergence fields is larger at redshift $z_s = 6.7$, indicated by a broader $\mathrm{PDF}_{\Delta\kappa}$.

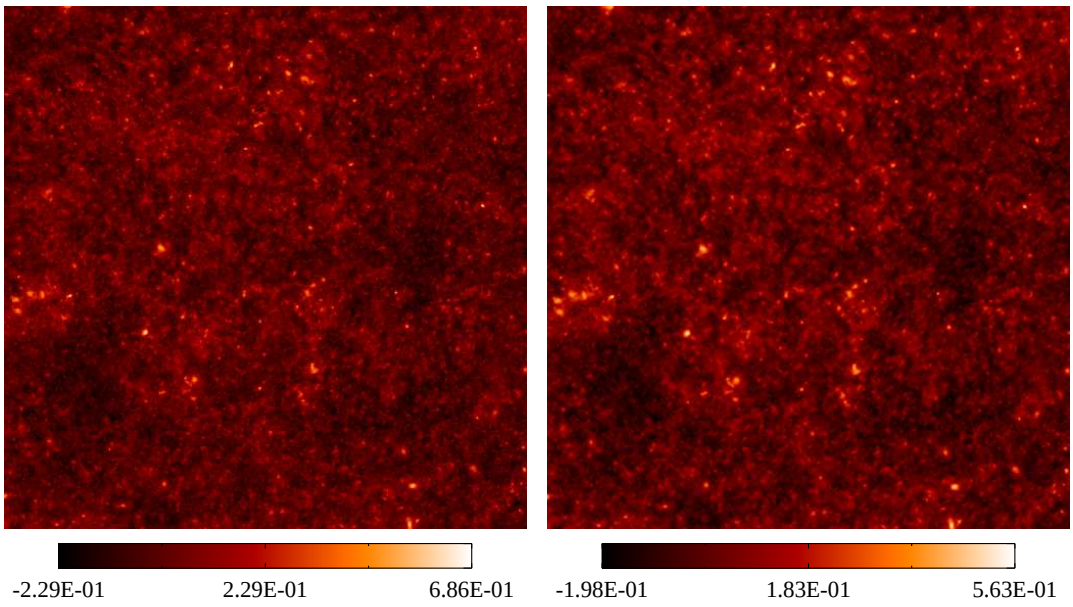

Figure B.3: Same realization as in figure B.1 of an effective convergence field $\kappa_{\rm eff}(\vec{\theta})$ of angular size $\theta \simeq 2.13°$ for $z_s = 6.7$. *Left panel*: The convergence $\kappa_{\rm eff}$ as computed from the evolution equation of the Jacobian $\mathcal{A}$. *Right panel*: The convergence $\tilde{\kappa}_{\rm eff}$ as obtained from the lensing deflection angle $\vec{\alpha}$.

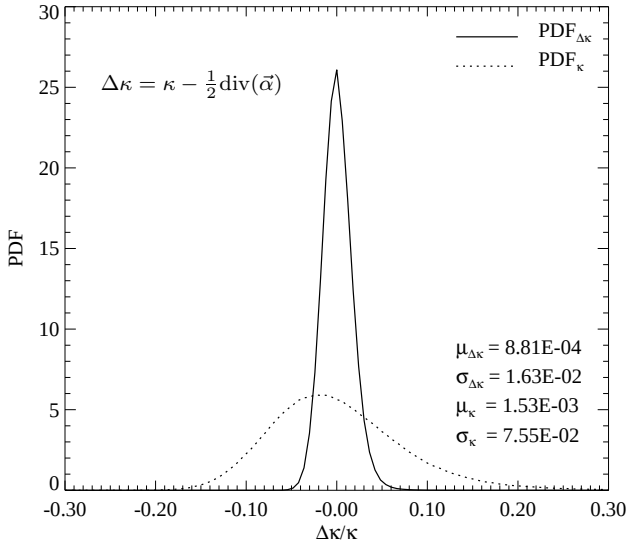

Figure B.4: Comparison of the probability distribution function of the effective convergence field, PDF_κ, with the probability distribution of the difference of the two convergence fields, $\mathrm{PDF}_{\Delta\kappa}$ for $z_s = 6.7$.

B.1.3 Comparison of the Power Spectra of the Convergence Fields

Figure B.5 shows power spectra for the difference of the two independently obtained convergence fields $P_{\Delta\kappa}(\ell)$ (crosses with error bars) compared to the theoretical prediction of the effective convergence power spectrum $P_\kappa(\ell)$ (solid line) at different source redshifts z_s, as indicated by their colors. The average and the standard deviation were taken over 50 realizations.

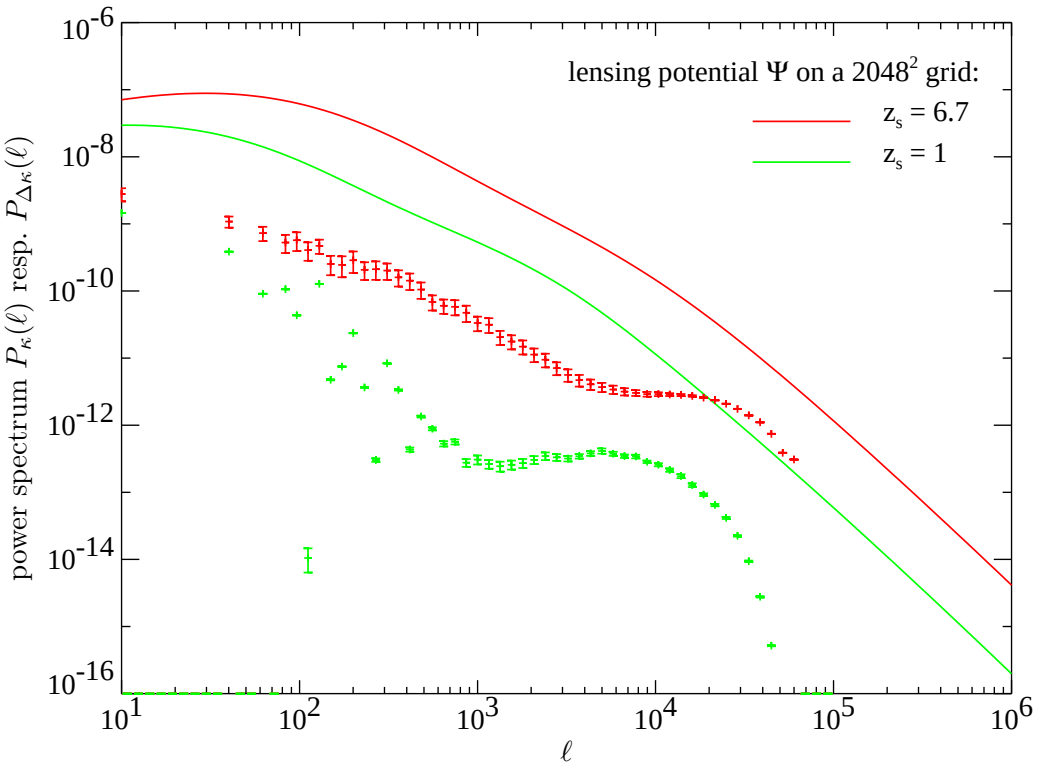

Figure B.5: Power spectra of the difference of the two convergence fields $P_{\Delta\kappa}(\ell)$ (crosses with error bars) are compared to the theoretical prediction of the power spectra of the effective convergence $P_\kappa(\ell)$ (solid line) for different source redshifts z_s according to their colors, respectively.

For $z_s = 1$, an enhancement of $P_{\Delta\kappa}(\ell)$ is visible, starting on scales $\ell \gtrsim 3 \cdot 10^3$, indicating correlations of the difference field $\Delta\kappa$ on these scales, i.e. non–vanishing difference of the two independently obtained convergence fields. This seems to be most probably a result of the effective resolution, already discussed in section 6.2.1.

This effect fades away in the case of $z_s = 6.7$ due to the modified lensing efficiency function and the larger number of integrated lens planes. Yet, another prominent feature develops on scales $\ell \gtrsim 3 \cdot 10^4$, which can be identified with the mean grid separation of the distorted mesh corresponding to the Nyquist frequency $\ell_N = 4.32 \cdot$

10^4. However, these scales are much smaller than the scales of interest for weak lensing of the CMB photons considering the resolution of the PLANCK experiment $\ell_{\mathrm{res}} \approx 2 \cdot 10^3$, to which we aim for.

B.2 Influence on the Power Spectrum due to Interpolation Schemes

In order to lens the temperature field of the CMB, one has to interpolate the temperatures on a given grid onto the light ray positions defined on another grid or vice versa. The influence of our linear interpolation routine on the power spectrum is studied in figure B.6.

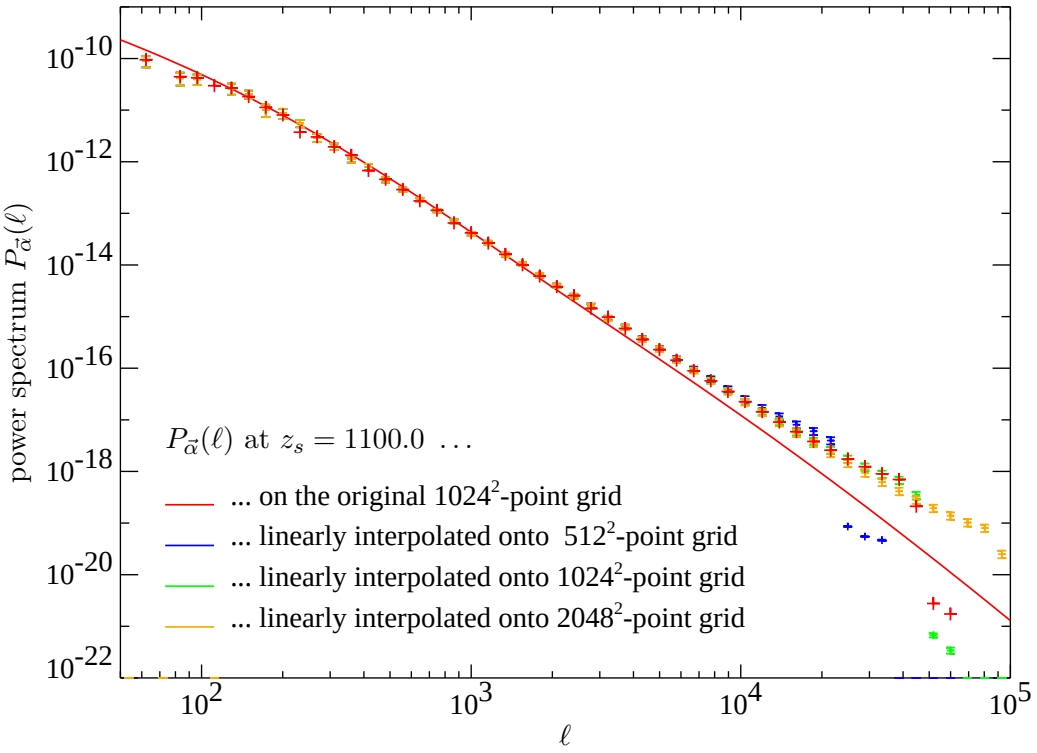

Figure B.6: Power spectra of the deflection angle $P_{\vec{\alpha}}(\ell)$ at different source redshifts z_s, respectively. Comparison of the theoretical prediction (solid lines) to the "measured" power spectra of ray tracing simulations (crosses).

The solid red line represents the theoretical prediction of the power spectrum of the effective lensing deflection angle $P_{\vec{\alpha}}(\ell)$, whereas the red crosses show its average measurement of 50 ray tracing simulations on the original 1024^2–point grid (0.25 arcmin

grid spacing) as indicated in section 6.1. The error bars of this graph are suppressed in order to show the influence of the studied effect only. After linearly interpolating the α_{eff} field onto a regular $\{512^2$–point, 1024^2–point, 2048^2–point$\}$ grid with gid spacing of $\{0.48, 0.24, 0.12\}$ arcmin, one obtains the {blue, green, orange} graph. The average has also been taken over 50 realizations.

They all agree very nicely with the original 1024^2–point grid on scales up to $\ell \approx 10^4$. In the figure both the datapoints and the errorbars of the interpolated grid at large and intermediate scales appear on top of each other, so the different colors are indistiguishable. However, each interpolated grid picks up small power near its own Nyquist frequency (e.g. in the case of the 512^2–point grid at $\ell_N = 2.25 \cdot 10^4$), whereas they lack power above their Nyquist frequency, as expected. This interpolation routine was applied both in chapter 6 for the ray tracing code and in chapter 7 for studying weak lensing of the CMB photons.

Acknowledgments

Foremost, I would like to thank my advisor Professor Simon White from the Max–Planck–Institute for Astrophysics at Garching for entrusting me with the challenging and interesting topic of this diploma thesis and for lending me his valuable advice. His ideas were crucial in shaping the scientific course of this work.

I also wish to thank my advisor Professor Reinhard Meinel from the Friedrich–Schiller University of Jena for supporting my external thesis at the Max–Planck–Institute for Astrophysics.

Working with Matthias Bartelmann was a pleasure for which I am grateful, particularly for his never–ending patience in clarifying my initial misunderstandings of physical problems. He was always supportive, willing to answer my questions, and spent large amounts of time helping me interpret the sometimes bewildering results of my simulations. I especially enjoyed his encouraging manner during enlightening discussions and his constructive comments over the entire period of this work which led to a substantial improvement of this thesis not only in its presentation but especially in its content.

I am also indebted to Martin Reinecke for his expertise in solving several numerical problems. His suggestions were always very useful. Many thanks to Takashi Hamana for providing us with his original simulation code, which we used for ray tracing photons through cosmological N–body simulations, as well as for helpful discussions. I also owe thanks to Björn Malte Schäfer for fruitful discussions, inspiring remarks, and relaxing conversations. Lots of thanks also to numerous other people at the Max–Planck–Institute for making it such a nice and inspiring place, particularly to Florian Siebel and Fritz Röpke.

I would like to thank the *Evangelisches Studienwerk Villigst* for the confidence they have placed in me.

Special thanks goes to my girlfriend Claudia for her constant encouragement in the course of this year. She has been very patient with me during this time and had to forgo my company very often. Finally, I am very grateful to my parents for their unconditional support throughout my life. Without them, neither my study of physics nor this diploma thesis would have been possible.

Erklärung

Ich erkläre, daß ich die vorliegende Arbeit selbstständig verfaßt und keine anderen als die angegebenen Quellen und Hilfsmittel benutzt habe.

Garching, den 6. Juni 2002 .....

Bibliography

Abramowitz, M., Stegun, I. A.: 1984, *Pocketbook of Mathematical Functions*, Frankfurt am Main: Harry Deutsch

Albrecht, A., Steinhardt, P. J.: 1982, *Physical Review Letters* **48**, 1220

Alpher, R. A., Herman, R. C.: 1950, *Reviews in Modern Physics* **22**, 153

Banday, A. J., Gorski, K. M., Bennett, C. L., Hinshaw, G., Kogut, A., Lineweaver, C., Smoot, G. F., Tenorio, L.: 1997, *Astrophysical Journal* **475**, 393

Bartelmann, M., Schneider, P.: 2001, *Physics Reports* **340**, 291

Blanchard, A., Schneider, J.: 1987, *Astronomy & Astrophysics* **184**, 1

Blandford, R. D., Saust, A. B., Brainerd, T. G., Villumsen, J. V.: 1991, *Monthly Notices of the Royal Astronomical Society* **251**, 600

Bond, J. R., Efstathiou, G.: 1984, *Astrophysical Journal Letters* **285**, L45

Briel, U. G., Henry, J. P., Boehringer, H.: 1992, *Astronomy & Astrophysics* **259**, L31

Burles, S., Nollett, K. M., Turner, M. S.: 2001, *Astrophysical Journal Letters* **552**, L1

Carlberg, R. G., Yee, H. K. C., Ellingson, E.: 1997, *Astrophysical Journal* **478**, 462

Carroll, S. M., Press, W. H., Turner, E. L.: 1992, *Annual Reviews of Astronomy & Astrophysics* **30**, 499

Cole, S., Efstathiou, G.: 1989, *Monthly Notices of the Royal Astronomical Society* **239**, 195

Davis, M., Peebles, P. J. E.: 1983, *Astrophysical Journal* **267**, 465

de Bernardis, P., Ade, P. A. R., Bock, J. J., Bond, J. R., Borrill, J., Boscaleri, A., Coble, K., Contaldi, C. R., Crill, B. P., De Troia, G., Farese, P., Ganga, K., Giacometti, M., Hivon, E., Hristov, V. V., Iacoangeli, A., Jaffe, A. H., Jones, W. C., Lange, A. E., Martinis, L., Masi, S., Mason, P., Mauskopf, P. D., Melchiorri, A., Montroy, T., Netterfield, C. B., Pascale, E., Piacentini, F., Pogosyan, D., Polenta, G., Pongetti, F., Prunet, S., Romeo, G., Ruhl, J. E., Scaramuzzi, F.: 2002, *Astrophysical Journal* **564**, 559

d'Inverno, R.: 1992, *Introducing Einstein's Relativity*, Oxford: Clarendon

Dyson, F. W., Eddington, A. S., Davidson, C. R.: 1920, *Memoirs Royal Astronomical Society* **62**, 291

Einstein, A.: 1915, *Sitzungsberichte der Preußischen Akademie der Wissenschaften* **1**, 831

Fixsen, D. J., Cheng, E. S., Gales, J. M., Mather, J. C., Shafer, R. A., Wright, E. L.: 1996, *Astrophysical Journal* **473**, 576

Freedman, W. L., Madore, B. F., Gibson, B. K., Ferrarese, L., Kelson, D. D., Sakai, S., Mould, J. R., Kennicutt, R. C., Ford, H. C., Graham, J. A., Huchra, J. P., Hughes, S. M. G., Illingworth, G. D., Macri, L. M., Stetson, P. B.: 2001, *Astrophysical Journal* **553**, 47

Fukugita, M., Futamase, T., Kasai, M., Turner, E. L.: 1992, *Astrophysical Journal* **393**, 3

Gamow, G.: 1948, *Physical Review* **74**, 505

Gradshteyn, I. S., Ryzhik, I. M.: 1980, *Tables of Integrals, Series and Products*, London: Academic Press

Guth, A. H.: 1981, *Physical Review D* **23**, 347

Hamana, T., Mellier, Y.: 2001, *Monthly Notices of the Royal Astronomical Society* **327**, 169

Heath, D. J.: 1977, *Monthly Notices of the Royal Astronomical Society* **179**, 351

Hewitt, J. N., Turner, E. L., Lawrence, C. R., Schneider, D. P., Gunn, J. E., Bennett, C. L., Burke, B. F., Mahoney, J. H., Langston, G. I., Schmidt, M., Oke, J. B., Hoessel, J. G.: 1987, *Astrophysical Journal* **321**, 706

Hockney, R. W., Eastwood, J. W.: 1988, *Computer simulation using particles*, Bristol: Hilger, 1988

Hu, W.: 2000, *Physical Review D* **62**, 043007

Hu, W., White, M.: 2001, *Astrophysical Journal* **554**, 67

Jaffe, A. H., Ade, P. A. R., Balbi, A., Bock, J. J., Bond, J. R., Borrill, J., Boscaleri, A., Coble, K., Crill, B. P., de Bernardis, P., P. Farese, P., Ferreira, P. G., Ganga, K., Giacometti, M., Hanany, S., Hivon, E., Hristov, V. V., Iacoangeli, A., Lange, A. E., Lee, A. T., Martinis, L., Masi, S., Mauskopf, P. D., Melchiorri, A., Montroy, T., Netterfield, C. B., Oh, S., Pascale, E., Piacentini, F., Pogosyan, D., Prunet, S., Rabii, B., Rao, S., Richards, P. L., Romeo, G., Ruhl, J. E., Scaramuzzi, F., Sforna, D., Smoot, G. F., Stompor, R., Winant, C. D., Wu, J. H. P.: 2001, *Physical Review Letters* **86**, 3475

Jain, B., Mo, H. J., White, S. D. M.: 1995, *Monthly Notices of the Royal Astronomical Society* **276**, L25

Jain, B., Seljak, U. ., White, S.: 2000, *Astrophysical Journal* **530**, 547

Jenkins, A., Frenk, C. S., Pearce, F. R., Thomas, P. A., Colberg, J. M., White, S. D. M., Couchman, H. M. P., Peacock, J. A., Efstathiou, G., Nelson, A. H.: 1998, *Astrophysical Journal* **499**, 20

Jenkins, A., Frenk, C. S., White, S. D. M., Colberg, J. M., Cole, S., Evrard, A. E., Couchman, H. M. P., Yoshida, N.: 2001, *Monthly Notices of the Royal Astronomical Society* **321**, 372

Jungman, G., Kamionkowski, M., Greist, K.: 1995, *Physics Reports* **267**, 196

Kaiser, N.: 1992, *Astrophysical Journal* **388**, 272

Landau, L. D., Lifshitz, E. M.: 1997, *Klassische Feldtheorie*, Frankfurt am Main: Verlag Harri Deutsch

Lee, A. T., Ade, P., Balbi, A., Bock, J., Borrill, J., Boscaleri, A., de Bernardis, P., Ferreira, P. G., Hanany, S., Hristov, V. V., Jaffe, A. H., Mauskopf, P. D., Netterfield, C. B., Pascale, E., Rabii, B., Richards, P. L., Smoot, G. F., Stompor, R., Winant, C. D., Wu, J. H. P.: 2001, *Astrophysical Journal Letters* **561**, L1

Linder, E. V.: 1988, *Astronomy & Astrophysics* **206**, 199

Lynds, R., Petrosian, V.: 1986, *Bulletin of the American Astronomical Society* **18**, 1014

Mather, J. C., Fixsen, D. J., Shafer, R. A., Mosier, C., Wilkinson, D. T.: 1999, *Astrophysical Journal* **512**, 511

Miralda-Escude, J.: 1991, *Astrophysical Journal* **380**, 1

Misner, C., Thorne, K., Wheeler, J.: 1973, *Gravitation*, San Francisco: Freeman

Mohr, J. J., Mathiesen, B., Evrard, A. E.: 1999, *Astrophysical Journal* **517**, 627

Narayan, R., Bartelmann, M.: 1995, in "Jerusalem Winter School",

Padmanabhan, T.: 1993, *Structure Formation in the Universe*, Cambridge: University Press

Peacock, J. A.: 1999, *Cosmological Physics*, Cambridge: University Press

Peacock, J. A., Dodds, S. J.: 1996, *Monthly Notices of the Royal Astronomical Society* **280**, L19

Peebles, P. J. E.: 1987, *Nature* **327**, 210

Peebles, P. J. E.: 1993, *Principles of Physical Cosmology*, Princeton: University Press

Penzias, A. A., Wilson, R. W.: 1965, *Astrophysical Journal* **142**, 419

Perlmutter, S., Aldering, G., della Valle, M., Deustua, S., Ellis, R. S., Fabbro, S., Fruchter, A., Goldhaber, G., Groom, D. E., Hook, I. M., Kim, A. G., Kim, M. Y., Knop, R. A., Lidman, C., McMahon, R. G., Nugent, P., Pain, R., Panagia, N., Pennypacker, C. R., Ruiz-Lapuente, P., Schaefer, B., Walton, N.: 1998, *Nature* **391**, 51

Premadi, P., Martel, H., Matzner, R.: 1998, *Astrophysical Journal* **493**, 10

Press, W. H., Teukolsky, S. A., T., V. W., Flannery, B. P.: 1992, *Numerical Recipes in FORTRAN: The Art of Scientific Computing*, Cambridge: University Press

Riess, A. G., Filippenko, A. V., Challis, P., Clocchiatti, A., Diercks, A., Garnavich, P. M., Gilliland, R. L., Hogan, C. J., Jha, S., Kirshner, R. P., Leibundgut, B., Phillips, M. M., Reiss, D., Schmidt, B. P., Schommer, R. A., Smith, R. C., Spyromilio, J., Stubbs, C., Suntzeff, N. B., Tonry, J.: 1998, *Astronomical Journal* **116**, 1009

Sachs, R. K., Wolfe, A. M.: 1967, *Astrophysical Journal* **147**, 73

Schneider, P., Ehlers, J., Falco, E. E.: 1992, *Gravitational Lenses*, New York: Springer Verlag

Seljak, U.: 1996, *Astrophysical Journal* **463**, 1

Seljak, U., Zaldarriaga, M.: 1996, *Astrophysical Journal* **469**, 437

Silk, J.: 1977, *Astrophysical Journal* **211**, 638

Smoot, G. F., Gorenstein, M. V., Muller, R. A.: 1977, *Physical Review Letters* **39**, 898

Soldner, J.: 1804, *Berliner Astronomische Jahrbücher* **1804**, 161

Soucail, G., Fort, B., Mellier, Y., Picat, J. P.: 1987, *Astronomy & Astrophysics* **172**, L14

Turner, M. S.: 1990, *Physics Reports* **197**, 67

Turner, M. S.: 1999, in "ASP Conference Series 165: The Third Stromlo Symposium: The Galactic Halo", 431

Walsh, D., Carswell, R. F., Weymann, R. J.: 1979, *Nature* **279**, 381

Wambsganss, J., Cen, R., Ostriker, J. P.: 1998, *Astrophysical Journal* **494**, 29

Watanabe, K., Tomita, K.: 1991, *Astrophysical Journal* **370**, 481

White, S. D. M., Efstathiou, G., Frenk, C. S.: 1993a, *Monthly Notices of the Royal Astronomical Society* **262**, 1023

White, S. D. M., Frenk, C. S., Davis, M.: 1983, *Astrophysical Journal Letters* **274**, L1

White, S. D. M., Navarro, J. F., Evrard, A. E., Frenk, C. S.: 1993b, *Nature* **366**, 429

Yoshida, N., Sheth, R. K., Diaferio, A.: 2001, *Monthly Notices of the Royal Astronomical Society* **328**, 669

Zaldarriaga, M., Seljak, U. .: 1998, *Physical Review D* **58**, 023003